12-2015

Designing Optical Properties in Infrared Glass

Benn Gleason
Clemson University, benn.gleason@gmail.com

DESIGNING OPTICAL PROPERTIES IN INFRARED GLASS

A Dissertation

Presented to

the Graduate School of

Clemson University

In Partial Fulfillment

of the Requirements for the Degree

Doctor of Philosophy

Materials Science and Engineering

by

Benn Gleason

December 2015

Accepted by:

Dr. Igor Luzinov, Committee Chair

Dr. Kathleen Richardson, Adviser, Co-Chair

Dr. John Ballato

Dr. Eric Johnson

Dr. Konstantin Kornev

ABSTRACT

Chalcogenide glasses (ChGs) are well-known for their attractive optical properties, such as high refractive index and transparency in across infrared wavelengths. ChGs also possess the ability to compositionally tune properties such as the refractive index, the thermo-optic coefficient, and other non-optical properties. Chalcogenide glasses with compositionally tailored physical and optical properties will provide optical designers with new materials necessary to create novel infrared imaging systems requiring new or expanded functionality.

This dissertation has evaluated the relationship between glass composition, the resulting atomic structure, and resulting optical and thermo-optical properties, with specific focus on the infrared refractive index and the thermo-optic coefficient (dn/dT). To create these linkages, a series of GeAsSe glasses with increasing Ge content were fabricated across three tielines, and evaluated for their chemical and physical attributes. A novel infrared refractometer was constructed to provide supplemental refractive index and dn/dT data.

Findings in this dissertation showed a correlation between the Ge content of the glass composition and several non-optical properties. Namely, as the Ge content increases, the glass transition temperature and Vickers Hardness increase, while the coefficient of thermal expansion decreases. These physical changes are due to the cross-linking of the glassy network by the 4-coordinated Ge additions.

In contrast, optical property data showed a strong dependence on the appearance and/or disappearance of specific atomic structures within the glassy network as the glass composition changes.

Overall, this study aimed to answer key questions that have not been systematically studied within multi-component chalcogenide glasses. These questions include:

- How will compositional variations for the sake of optical tunability affect the physical properties which dictate a materials' response to manufacturing processes?
- Are there links between optical properties, such as the index and dn/dT, and non-optical properties that can allow for easier prediction of the difficult to measure optical properties?
- Are there compositions within the GeAsSe ternary that can produce a zero dn/dT that will offer better thermo-mechanical stability to the current commercial options?

Finally, this work presented a new phenomenon of a thermally-induced, sub-T_g index hysteresis and subsequent room temperature structural relaxation in chalcogenide glasses. This process resulted in a maximal change in the room temperature refractive index of 0.0030. Over the course of 2 months the structural relaxations returned the refractive index to the initial state, with a characteristic relaxation time ranging from τ = 70,000s to τ = 300,000s.

DEDICATION

During my time as a graduate student I have lived and worked in three different states and two different countries. I would like to dedicate this dissertation the numerous people during that time who have helped me feel at home without actually being anywhere near home.

ACKNOWLEDGMENTS

I would first like to thank my parents who have provided the financial support necessary for me to continue my education all the way to a PhD, and the little extra beer money to not go crazy in the process.

Next I would like to thank Dr. Kathleen Richardson and Clemson University for giving me the opportunity to leave Arizona, explore the country in the name of science and collaboration, and, for whatever reason, to go back to Arizona.

I would like to thank my many collaborators across the country including Amy Qiao and Norm Anheier at PNNL for being wonderful coworkers and mentors while I spent my summers with them in Richland, Washington. Dr. McCloy at Washington State University for his assistance with the analysis of my optical data, which led to the final breakthroughs needed to complete this dissertation. Dr. Pao Tai Lin at Massachusetts Institute of Technology for assistance in laser integration at the UCF. Lockheed Martin for financial and experimental support of my research during my time at the UCF.

Finally I would like to thank all of my fellow students and coworkers at Clemson University and University of Central Florida: Guillaume Guery, Andy Buff, Erick Koontz, Spencer Novak, Jackie Novak, Laura Sisken, Antoine Lepicard, James Marco, Dr. Dave Musgraves, Pete Wachtel, Dr. Charmayne Smith, Dr. Jason Lonergan, and Karima Chamma.

TABLE OF CONTENTS

Page

Table of Contents (Continued)

Page

Table of Contents (Continued)

Page

LIST OF TABLES

Table Page

List of Tables (Continued)

Table Page

LIST OF FIGURES

Figure Page

List of Figures (Continued)

Figure Page

List of Figures (Continued)

Figure Page

List of Figures (Continued)

Figure Page

List of Figures (Continued)

Figure Page

List of Figures (Continued)

Figure Page

List of Figures (Continued)

Figure Page

List of Figures (Continued)

Figure Page

List of Figures (Continued)

Figure Page

List of Figures (Continued)

Figure Page

List of Figures (Continued)

Figure Page

Chapter 1

Materials for Infrared Optics

The rapid growth of infrared (IR) imaging, sensing and detection systems deployed in diverse civilian and military applications within the past decade has come about largely due to advances in detector technologies that have dramatically reduced system size, weight and thereby the costs to produce such systems. Lagging behind these advances, has been the adoption of new materials to replace the legacy bulk (crystalline) optical materials largely developed for military systems in the 1960-1980 timeframe. Adoption of new materials in optical designs needed for these next-generation systems will be enhanced not only by the commercial availability of glassy alternatives to the legacy crystalline materials, but also with a recognition that infrared optical glass solutions can exploit specific physical property optimization through compositional tuning. While just a few commercial glass compositions are currently available, new glass solutions can be realized if a broader understanding of the inter-relationship between chemistry, structure and properties is known.

This work aims to define such relationships using a ternary, multicomponent glass system as a model. As discussed herein, this representative glass system has been chosen to illustrate the power of engineering a glass system to attain desirable optical and thermo-optical properties. While optical properties define the optical performance of the element in a system, an understanding of the inter-relationship of the material's structure on other behavior important to its processing, optical fabrication and metrology and eventual

integration and performance in its environment of use, is also critical. This dissertation will connect these thoughts and illustrate how the design and test of such materials can provide key understanding critical for use of bulk infrared glasses in mid-wave transmitting systems.

This chapter discusses the basic information needed to understand and approach the challenges associated with current infrared (IR) optics technology. Firstly, the necessary definitions relevant to the fields of IR optics, glassy materials, and specifically focus on IR optical materials will be presented. As the similarities between state of the art visible optical materials and IR optical materials are discussed, the chapter will highlight the shortcomings of IR materials in terms of both manufacturing and optical performance.

The properties of commercially available IR materials, both crystalline and glassy, will be discussed further highlighting the need for a focused study to develop new materials. The chapter will also discuss reasoning behind selecting a specific chalcogenide glass forming ternary system for analysis, and discuss the current understandings of relevant physical and structural properties of these glasses. Finally, this chapter will establish the overreaching goals of this dissertation and the tasks that need to be completed and fundamental questions that need to be answered in order to achieve those goals.

1.1 What is Infrared Optics?

Infrared (IR) optics is a branch of optical science and engineering that focuses on wavelengths longer than visible light, typically as the wavelengths ranging from 750nm to ~1,000 μm. Because of the wide range of wavelengths often included in this definition, IR

wavelengths are often further divided into sub-infrared regimes. These zones include the near-IR (NIR), ranging from ~750nm to ~1500nm; shortwave IR (SWIR), ranging from ~1500nm to ~3000nm; the mid-wave IR (MWIR), ranging from ~3000nm to ~8000nm; the long-wave or thermal IR (LWIR / TIR), from ~6000nm to ~50µm; and finally the far infrared for wavelengths larger than 50µm. These transitions are not clearly defined across all users, and can change significantly depending on the author or application. For this work, the sub-infrared regimes are defined as mentioned above, and are highlighted in Figure 1.1.

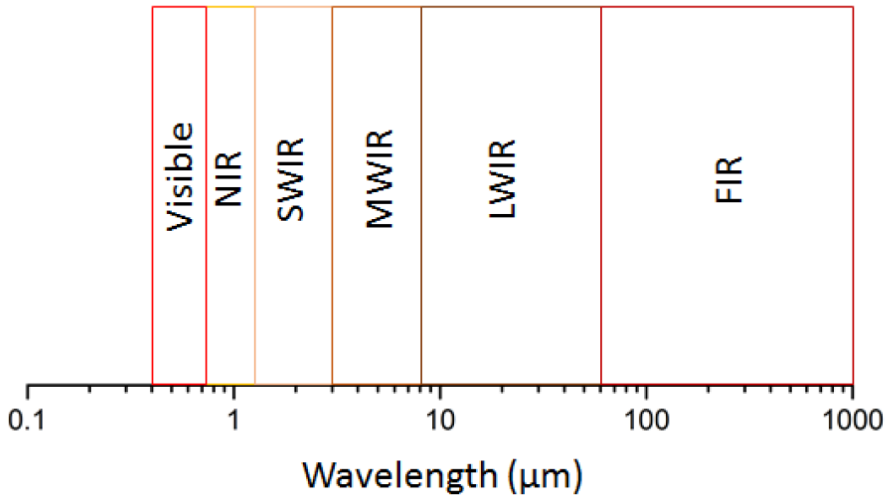

Figure 1.1 – Representation of the relevant sub-infrared regimes as a function of wavelength [1].

Infrared (IR) wavelengths present different and unique challenges compared visible wavelengths, which have the advantage of long history of scientific and engineering advancements. The primary challenge of the IR lies in finding suitable materials to transmit, reflect, and refract incoming light. Optical systems in the visible wavelengths often rely on optical (oxide) glasses made of combinations of silicon and oxygen

("silicates" in the form SiO_2), phosphorus and oxygen ("phosphates" in the form P_2O_5), aluminum and oxygen ("aluminates" in the form Al_2O_3), and can include other elements such as boron and select alkali and alkaline earth to transmit the visible light. The optical properties of these glasses are characterized typically by their index (n) and dispersion /Abbe number (ν), in a figure known as an Abbe diagram as shown in Figure 1.2, which includes all available oxide glasses from glass manufacturer, Schott Glass, Inc. [2]. A glasses Abbe number is calculated through the following equation:

$$\nu = \frac{n_d - 1}{n_f - n_c}$$

Equation 1

Where n_d, n_f, and n_c are the refractive index measured at 589.3 nm, 486.1 nm, and 656.3 nm respectively. The Abbe number equation can also be used to characterize the dispersion in other spectral regimes, by changing the measurement wavelengths of the three refractive index points in the equation. Additionally, the Abbe number of non-traditional wavelength regimes can be calculated by changing the wavelengths of n_d, n_f, and n_c. The requirement for appropriately changing the Abbe number wavelength regime is that the new n_f stays the shorter wavelength, the new n_d is the middle, and the new n_c stays the longer wavelength. For example, the MWIR Abbe number could be calculated through changing n_d to $n_{4\mu m}$, n_f to $n_{3\mu m}$, and n_c to $n_{5\mu m}$.

Available oxide glasses typically have a refractive index between 1.5 and 1.9, and have an Abbe number between 25 and 70. Schott's N-KB7, a borosilicate glass, is perhaps the most

widely used oxide glass for optical applications, and its properties are frequently used as a representative values for oxide glasses.

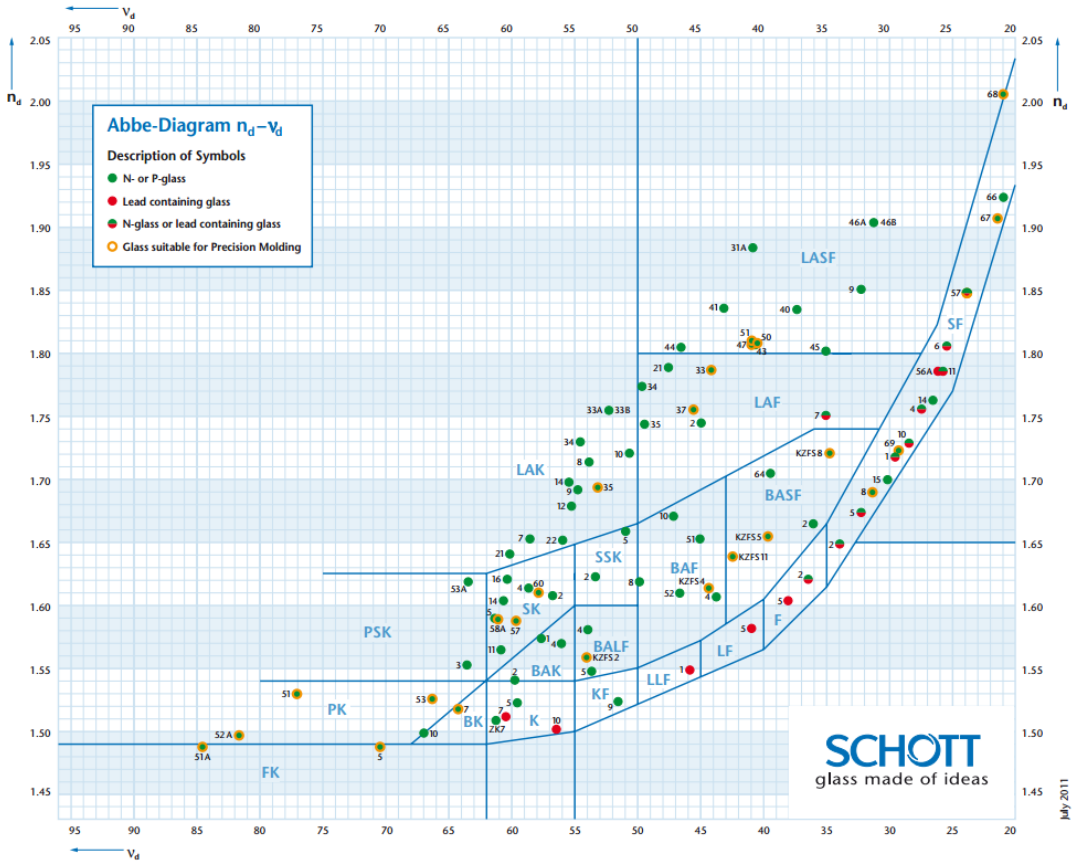

Figure 1.2 – Abbe diagram of oxide (visibly transparent) glasses available from Schott Glass, Inc. [2]

The transmission of N-BK7, and a majority of other oxide glasses, ranges from approximately 350nm to 2500nm, and would not be suitable for any application for that extends beyond the NIR [2]. The long wavelength transmission cutoff is due to intrinsic modifier–Oxygen (M-O) vibrational mode absorptions of the glass constituents, known as

the multi-phonon edge. New materials are needed to shift the transmission window from visible and NIR wavelengths to cover a broader range of IR wavelengths. Ideally, as these materials transition further into the IR, optical designers would like an IR version of the Abbe diagram to aide in their design needs. A stylized version of an IR Abbe diagram is shown in Figure 1.3. Additionally a measure of the MWIR Abbe number and the MWIR partial dispersion was obtained from Schott Glass Inc. and is shown in Figure 1.4 [3]. In the partial dispersion equations shown used for calculating dispersion, the subscripts on the indices represent the wavelength (in μms).

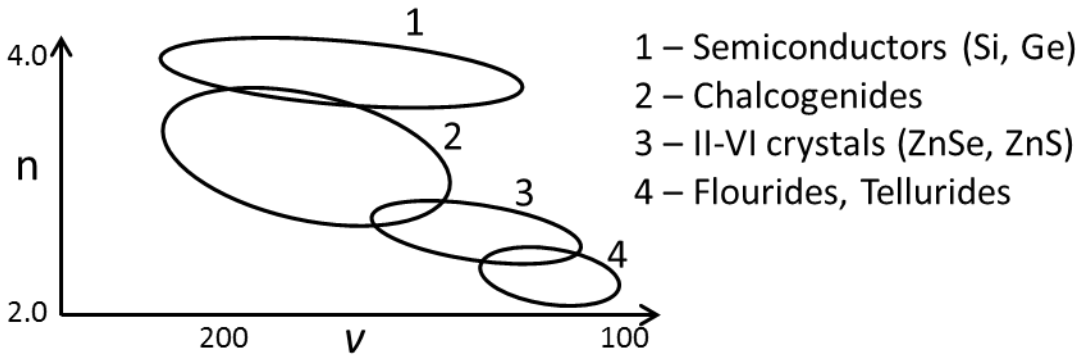

Figure 1.3 – Approximate index and dispersion values for IR transmitting materials.

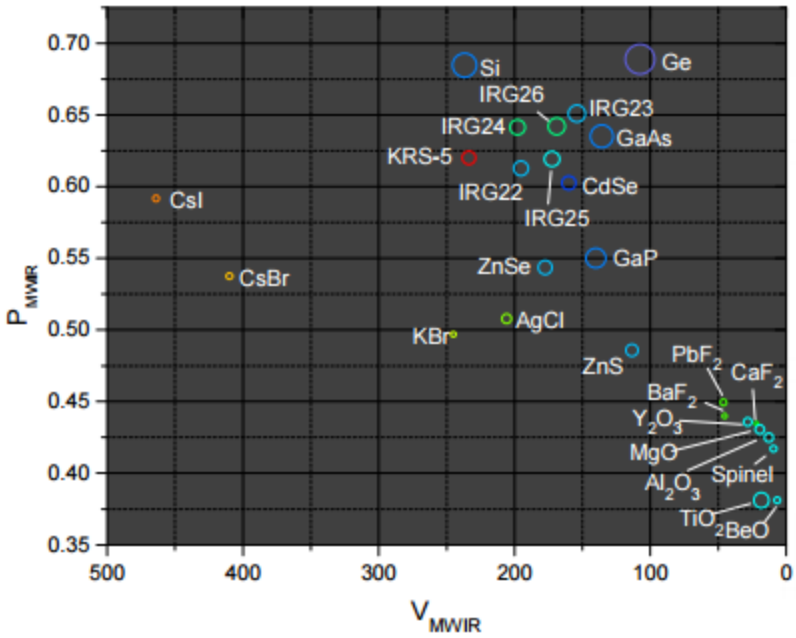

$$V_{MWIR} = \frac{n_4 - 1}{n_3 - n_5}$$

$$P_{MWIR} = \frac{n_3 - n_4}{n_3 - n_5}$$

Figure 1.4 – Chart of available IR materials, comparing the MWIR Abbe number (v_{MWIR}) and the MWIR partial dispersion (P_{MWIR}) [3].

In order to achieve IR transmission, the typical Si and O atoms of oxide glasses need to be replaced with heavier, larger atoms. The frequency of vibrational transitions between two elements, ν, can be modeled to a first order as a simple harmonic oscillator, as shown in Equation 2:

$$v = \frac{1}{2\pi}\sqrt{\frac{K}{M}}$$

Equation 2

where M is the effective mass of the atomic nuclei, K is the bond strength (spring constant). From this it is clear that as the mass of the atom increases (and coincidentally the effective bond strength decreases) the frequencies of vibrational transitions should shift to lower

frequencies. As a result, some of the preferred elements for IR transmission include: Si, S, Ga, Ge, As, Se, Pb, and Te.

1.2 Commercially Available Infrared Materials

Infrared-transparent materials are commercially available in two basic forms: crystalline or glassy. Crystalline materials have periodic, ordered structure that extends to medium (10s of nm) and long (μm to mm) length scales. Crystalline materials can contain a few as one crystal orientation (single crystal) or several crystallites in varying size and orientation (poly-crystalline). For IR applications there are a limited amount of viable crystalline materials with suitable optical and mechanical properties. Both Si and Ge are the two most widely used IR crystalline materials can be grown in single- and poly-crystalline forms. The properties and performance of both Si and Ge have been studied for several years and both are sold from numerous vendors. Both of these materials have a diamond cubic lattice with high hardness and modulus values, have a high refractive index and thermo-optic coefficient, and have a broad transmission window [4-11]. Extensive work has been performed to quantify the optical, mechanical, and thermal properties of these materials for both optical and semiconductor industries.

For example, Figure 1.5 shows the refractive index of Ge as a function of both index and wavelength in a 3D contour plot, obtained from [8]. Figures such as this are extremely useful in determining the refractive index for systems wide tolerances on temperature or wavelength.

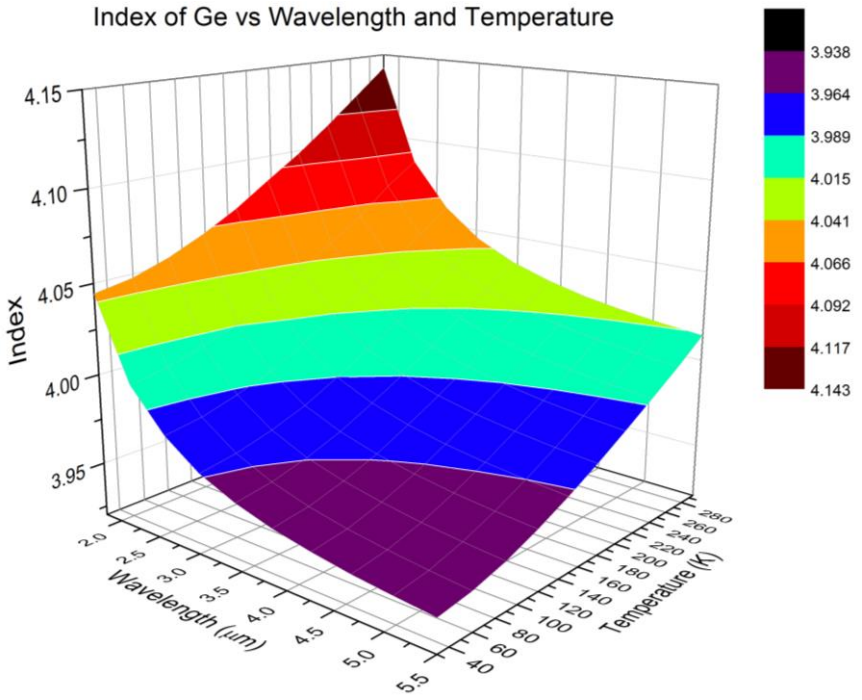

Figure 1.5 – Refractive index as a function of wavelength and temperature for single crystal Ge [8].

ZnSe and ZnS are two additional widely used IR transparent crystalline materials. Both ZnSe and ZnS share a unique crystal lattice called zincblende [12]. Zincblende can be envisioned either as interpenetrating face-centered-cubic lattices (one lattice for each element), or as a diamond cubic lattice where the atoms alternate between Zn and S/Se. Both ZnS and ZnSe are typically polycrystalline materials, and are formed through a chemical vapor deposition process. Like Si and Ge, ZnS/Se has been studied extensively [13-22] and is available from numerous vendors. When ZnS is subjected to hot isostatic pressing (HIP), the optical and mechanical properties of the material are augmented, and the resulting material is trademarked under the Cleartran name [23,24].

Similar to Ge and Si, ZnS/Se have broad transmission, and have favorable mechanical properties for fabrication. Unlike Si and Ge, ZnS/Se have comparatively low refractive

indices, low thermoptic coefficients, and a transmission window that extends to shorter wavelengths. A summary of relevant properties for Ge, Si, ZnS and ZnSe can be found in Table 1.1. These results are summarized in Table 1 and were obtained under specific experimental parameters. These conditions are defined, where known, in the footnotes below the table.

Table 1.1 – Mechanical, thermal, and optical property values of Ge, Si, ZnS, and ZnSe collected from literature. Experimental parameters and references are discussed below the table.

	Mechanical		Thermal	Optical	
	Hardness (GPa)	Young's Modulus (GPa)	CTE (10^{-6} °C^{-1})	Refractive index (n)	dn/dT (10^{-6} °C^{-1})
Ge	10 [a]	1.4 [b]	5.9 [c]	4.02051 [d]	420 [d]
Si	13 [a]	1.7 [b]	2.57 [c]	3.42404 [d]	170 [d]
ZnS	2.5 [e]	74 [f]	7.98 [g]	2.2002 [h]	3.87 [i]
ZnSe	1 [e]	70 [f]	8.57 [g]	2.4065 [h]	6.42 [j]

a Knoop Hardness measured at room temperature [25]
b Measured at room temperature along the <1,0,0> plane [26]
c Average of several compiled references at 300K [27]
d Measured at 295K and 4.5µm [8]
e Knoop hardness measured at room temperature [28]
f Measured at room temperature [28]
g Measured from 20°C – 600°C [28]
h measured at 10 µm [28]
i Measured from 298K - 358K at 3.39 µm [23]
j Measured at 295K and 4.5µm [29]

1.2.1 Commercially Available Glassy Materials

The main advantage of glassy materials over crystalline materials is that glasses are not locked in to a specific stoichiometry, and thus the composition can vary continuously to alter properties of the glass. The main type of glasses used for IR transmission are known as chalcogenide glasses (ChGs). Chalcogenide glasses consist of at least one chalcogen element (Group VI), with the exception of oxygen as it has strong vibrational absorptions in the IR. A stable glass can be formed when the chalcogen is combined with neighboring

elements from Group IV or V, such as Ge, As, Sb, Pb, or Bi. Most commercially available chalcogenide glasses include some combination of Ge and/or As with either S or Se. Despite the fact that the composition can be varied continuously to make a large number of glasses with unique properties, there are surprisingly few commercially available chalcogenide glasses. Shown in Table 1.2 are the primary commercially available ChGs, their compositions, and trade names.

Table 1.2 – Compositions of commercially available chalcogenide glasses, and their respective trade names

at% Ge	at% As	at% Sb	at% S	at% Se	at% Te	Schott Glass Inc. (VITRON GmbH) Trade name	Amorphous Materials Inc. Trade name	Umicore Trade name	Ref
33	12	-	-	55	-	IRG 22 (IG 2)	AMTIR 1	-	[30,31]
30	13	-	-	32	25	IRG 23 (IG 3)	-	-	[32]
10	40	-	-	50	-	IRG 24 (IG 4)	-	-	[33]
28	-	12	-	60	-	IRG 25 (IG 5)	AMTIR 3	-	[31,34]
-	40	-	-	60	-	IRG 26 (IG 6)	AMTIR 2	-	[31,35]
-	28	-	-	72	-	-	AMTIR 4 [a]	-	[31]
-	34	-	-	66	-	-	AMTIR 5 [b]	-	[31,36]
-	40	-	60	-	-	-	AMTIR 6*	-	[31]
22	20	-	-	58	-	-	-	GASIR 1	[37]
20	-	15	-	65	-	-	-	GASIR 2	[37]

[a] *Specific composition not explicitly stated in manufacturer's data sheet but assumed based on data sheet values for thermal expansion and glass transition temperature, and AsSe binary ($As_{25}Se_{75}$ and $As_{30}Se_{70}$) results from Musgraves et al. [38]*

[b] *Specific composition not explicitly stated in manufacturer's data sheet, but calculated from related patent data [36]*

1.2.2 Non-Commercial Chalcogenide Glasses

The binary combination of As and either S or Se is one of the most basic glass forming structures that can be made. In academic settings, researchers can explore the limits of compositional regions and glasses along the AsSe binary have been reported with compositions ranging from pure amorphous Selenium to compositions with more than 50 at% As [38-50]. This gives a very large compositional window for researchers to work with and allows for compositional dependency studies on a wide range of studies. Some of the

reported properties analyzed along the AsSe binary lines include, T_g [38,42,43,45-49], coefficient of thermal expansion [38,43,45,48], density [38,47,48,50], viscosity and fragility parameter [38,48], various hardness and moduli parameters [47,50-52], index of refraction [53-55] nonlinear refractive index [56], various energy gaps [40,47], and photo-modification effects [57]. Additionally the structure itself is also studied as a function of the composition along the tie-line, through techniques such as Raman spectroscopy [48,58,59], nuclear magnetic resonance (NMR) [60], x-ray photoelectron spectroscopy (XPS) [61-65].

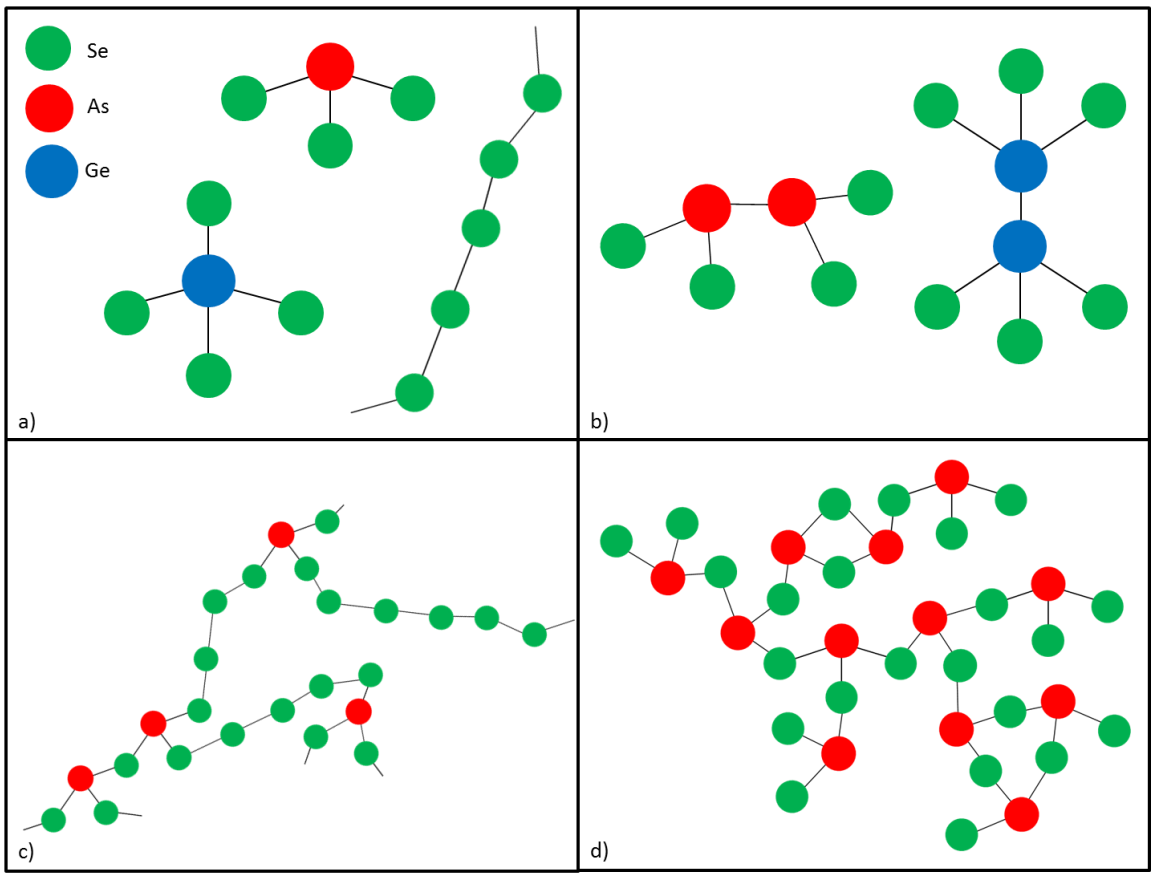

Figure 1.6 – a) Typical structures involving Ge, As, and Se: Se chains, $AsSe_{3/2}$ pyramids, and $GeSe_{4/2}$ tetrahedra, b) defect structures: $As_2Se_{4/2}$ and $Ge_2Se_{6/2}$ ethane-like modes, c) loosely bound AsSe structure with Se chains and AsSe pyramids, d) fully coordinated AsSe puckered layer structure observed at stoichiometry.

Sulfur and Selenium atoms are considered iso-structural atoms. That is, they serve the same role in a glass structure, and should behave similarly. The similar role of these two atoms allows for a general discussion of the structure for AsS and AsSe glasses. The chalcogen atoms (S/Se) belong to group VI and as such are able to form two bonds with neighboring atoms. Glass compositions that are heavily chalcogen excessive form long chains of S/Se of the form -S-S-S- or -Se-Se-Se- visualized as a "noodle-like" structure [48], and are visualized in Figure 1.6a and 5c. Additions of small amounts of As, a member of group V which can for 3 bonds with neighboring atoms, to S/Se creates pyramidal structures of the form $AsS_{3/2}$ or $AsSe_{3/2}$ [48,66], as shown in Figure 1.6a. These pyramidal structures connect the long S/Se chains in a process known as cross-linking or polymerizing [40,67,68]. Further additions of As to this network create more of the AsS/Se pyramidal units until the composition reaches the stoichiometric composition of As40S60 or As40Se60, also known as As_2S_3 and As_2Se_3 [47,48,59,69], as shown in Figure 1.6d.

The stoichiometric compositions of As_2S_3 and As_2Se_3 should theoretically have only As-S and As-Se hetero-polar bonds, respectively. The glass network would therefore consist primarily of the AsS or AsSe pyramidal structures. In reality, there is usually a small percentage of 'wrong'-bonding: homopolar bonds that form regardless of chemical order [63,70]. The AsS/Se structures connect to one another to form a single plane and the global structure is called a "puckered layer" structure shown in Figure 1.6d. These planes fold over themselves and are held together with weak van der Waals forces to create the 3D bulk glass structure [40,67,68]. Increasing the amount of As beyond 40 at% results in the expected formation of As-As homopolar bonds, due to the glass being chalcogen-deficient,

as depicted in Figure 1.6b. The structure becomes increasingly complex when As content increases beyond 40 at%, where molecular "cages" of As and Se that do not contribute to the overall network have been observed [71-74].

Incrementally changing the glass composition along the binary As-S and As-Se tielines allows for the systematic study of property variations as a function of chemistry, network connectivity, and topology/structure [38,40,48,59,66,75-78]. As can be seen, binary systems have been well studied and are well understood in terms of the influence of composition on properties. Of the previously mentioned properties studied along the AsSe binary (such as T_g, CTE, hardness), most vary linearly or approximately linearly as a function of As content. A strong deviation from linearity has been observed at the stoichiometric composition ($As_{40}Se_{60}$) for several properties, and has been attributed to a percolation threshold of rigidity [67,68,79,80]. This threshold was first predicted and described mathematically by Philips by comparing the number of constraints and the degrees of freedom of bonding within a particular composition. In this analysis each element is assigned a coordination number according to its position in the periodic table through the 8-N rule, where N is the number of valence electrons in the element's valence shell. Therefore As would have a coordination number (CN) of 3 (8 – 5 valence electrons), and S and Se would both have a CN of 2. The coordination of a glass composition is calculated by averaging the coordination numbers of all the constituents in their respective atomic percentages. For example a composition of $As_{20}Se_{80}$ would have a coordination number CN = 0.20*3 + 0.80*2 = 2.2 Increasing the As content to $As_{40}Se_{60}$ likewise results in a CN = 0.40*3+0.60*2 = 2.4. The work by Philips and Thorpe found that this threshold

should exist (seemingly regardless of actual chemistry) at a CN = 2.4 [67,68,80]. The prediction of this threshold holds true for binary glasses, but falls apart in ternary glass forming systems, as will be discussed in the following section.

1.2.3 Ternary GeAsSe

Moving from a binary glass system to a ternary or multicomponent glass system adds an extra degree of flexibility which usually leads to broader glass formation due to the mixing that occurs with more, dis-similar atoms. This compositional and property complexity also influences the compositionally-driven property changes described along the AsSe and AsS binaries, while generally adding enhanced stability to crystallization [81]. The additional constituents in the glass and the corresponding new bonding configurations make possible the ability to tailor specific properties required for specific applications. This lends the ternary glass system broader overall *tunability* of glass properties. For the specific application of infrared imaging, AsSe binary glasses *can* possess beneficial optical properties: high refractive index, broad transmission and low intrinsic absorptions, and low but varying thermoptic coefficients [31,35]. These same binary glasses however possess undesirable thermal/ mechanical characteristics such as low glass transition temperatures [38,82,83], high coefficients of thermal expansion (CTE) [38,66], poor photostability and photosensitivity [57,84-88], and poor hardness and chemical durability, particularly when compared to oxide glasses used for visible imaging systems [33,89]. In order to maintain the beneficial optical properties but overcome the undesirable thermal properties, compositional design with an additional constituent such as Germanium can be performed such that the properties can be tuned to meet specific design needs.

Germanium is a group IV element and is known to be glass network former in both oxide and chalcogenide glass systems. In chalcogenide glass (ChG) matrices it serves two functions; firstly, it enters the glass network in four-fold coordination and this additional bonding serves to increase connectivity of the structure. Addition of 4-fold Germanium to the lower coordinated As (3-fold) and Se (2-fold) atoms results in an increase in the glass' mean coordination number (MCN) which can dramatically enhance both thermal stability and mechanical robustness [66]. Additionally, it reduces the average number of lone-pair (LP) electrons per unit volume of the glass thus affecting local polarizability and hence, optical properties. As arsenic (1 LP per atom) and selenium (2 LP per atom) are replaced with germanium (0 LP per atom), not only is network connectivity increased but polarizability is markedly modified.

When Ge is added to binary AsSe glasses, the Ge additions preferentially form bonds with Se, as the electronegativity difference between Ge and Se is larger than As and Se [48]. The Ge will bond with 4 Se to create $GeSe_{4/2}$ tetrahedral units, and will further cross-link the puckered layers of AsSe [47,58,59,69,90-92] as shown in Figure 1.6a and Figure 1.7a, respectively. The Se atoms will next seek to form As-Se bonds. If more than enough Se is available to satisfy all of the Ge-Se and As-Se bonds, the composition is considered "Se-excessive". If there is exactly enough Se to satisfy all the required Ge-Se and As-Se bonds, the glass is considered "stoichiometric". Likewise, if there is not enough Se for the required bonds, the glass is "Se-deficient". X-ray photoelectron spectroscopy (XPS) and nuclear magnetic resonance spectroscopy (NMR) results have shown that regardless of whether the glass is Se-excessive or Se-deficient, a small number of Se-Se homopolar bonds will still

be present [63,70]. Results from XPS AND NMR investigations also show that the coordination numbers of Ge, As, and Se do not, in general, change with composition and the structures that are formed maintain their normal coordination [48,61,63].

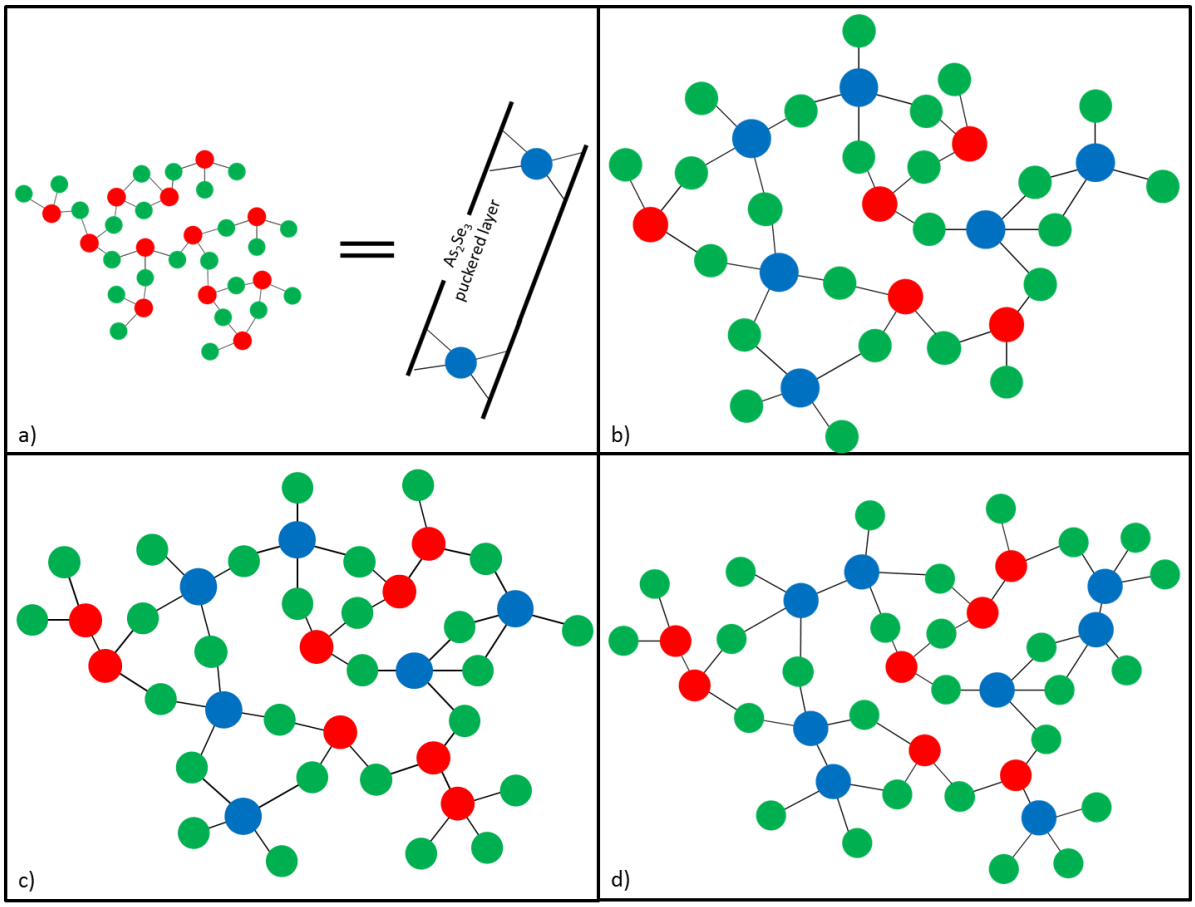

Figure 1.7 – a) Representation of how Ge additions cross-link the AsSe puckered layers, b) Stoichiometric structure with GeSe and AsSe structures, c) Se-poor network where $As_2Se_{4/2}$ defect structures are present, d) Se-poor network where $Ge_2Se_{6/2}$ ethane-like modes appear

When the compositions become increasingly Se-deficient, several studies have reported the formation of additional defect modes, such as $Ge_2Se_{6/2}$ ethane-like modes [58], Ge-Ge and As-As homo-nuclear (also called homopolar) bonds [70,93], shown in Figure 1.6b and

Figure 1.7d. It should also be noted that the presence of these defect states in Se excessive glasses have also been reported, but in significantly lower quantities [94].

Prior studies on the GeAsSe ternary system have examined the effects of composition, or MCN, on several materials properties, including glass transition temperature (T_g) [64,82,83,95-97], viscosity and fragility [95,98], optical bandgap [40], thermal diffusivity [99], elastic properties [96,97], and refractive index of limited compositions in thin film form [100]. Despite these numerous investigations on GeAsSe glasses, a study that systematically explores the impact of Ge additions on thermal, mechanical, and optical properties of glasses specifically designed for optical imaging applications where the compositional role of constituents on both optical properties and those attributes that most dictate optical manufacturing response, has not been carried out. This systematic study forms the core focus of the present effort.

1.2.4 Se-rich/-deficient compositions

At this time it is beneficial to introduce a concept of Se-rich and Se-poor percentages (equivalently called Se-excess/Se-deficiency), where these attributes are referenced relative to the chalcogen content at stoichiometry. Specific to the GeAsSe ternary system, the stoichiometric tieline connects the binary As_2Se_3 to $GeSe_2$ compositions. This concept is useful in ternary chalcogenide glasses as it is a method of determining the structures that *should* be present at a given chemistry (composition). As highlighted in this section, GeAsSe glasses can have multiple, unique structural units at the same time, and it is not feasible to investigate trends based on the amount of one structure, nor is it feasible to

include all of the structures in one coherent analysis. The Se rich/poor percentage can be calculated through:

$$\%Se - rich/-poor = 100 - 3x - 2.5y$$

Equation 3

where x and y represent the absolute amount of Ge and As in $Ge_xAs_ySe_{(100-x-y)}$. This formulation can be used to *assume* what structures should be present, based on Se's ability to fully form Se-Se chains, $AsSe_{3/2}$ pyramidal, or $GeSe_{4/2}$ tetrahedral structures [95]. Using the Se-rich/-poor percentage requires a prior knowledge of how constituents will bond together, which has been presented in this section, and is applied specifically for this case of the GeAsSe ternary.

For GeAsSe chalcogenide glasses with excess Se (*Se-rich*) content, structures of $GeSe_{4/2}$ and $AsSe_{3/2}$ are separated by chains of Se-Se bonds in what is referred to as the "chain-crossing" model [48]. Decreasing the amount of Se relative to Ge and As will increase the amount of GeSe and AsSe structures in the network until no Se-Se chains or rings will be able to form in between these structures, and there will be only enough Se to form $AsSe_{3/2}$ and $GeSe_{4/2}$. At this point the network is in stoichiometry and is considered neither *Se-rich nor Se-poor (i.e. 0%)*.

Further decreasing the amount of Se relative to Ge and As will result in Se preferentially forming bonds with Ge, as discussed in Section 1.2.3 [48], and results in a *Se-poor* network. The Se shortage will cause As to replace one of its Se bonds with a homopolar bonds between a neighboring As, in the form $Se_{2/2}$ – As – As – $Se_{2/2}$ [62,70]. The specific

condition of 0% in the Se-rich/-poor calculation results in a major shift in the structures and bonding arrangements of the GeAsSe ternary compositions.

Another major shift in structure and bonding has also been observed as further reductions in the Se content lead to the formation of additional defect states, such as the formation of GeSe ethane-like structures, in the form $Se_{3/2} – Ge – Ge – Se_{3/2}$ [62,70]. Recent XPS / NMR studies by the Luther-Davies group and has shown that the appearance of the GeSe ethane-like structures only occur when the network is sufficiently low in Se content. Using Equation 3 shows the compositions with GeSe ethane-like modes typically arise at regions between 20 and 30% Se-poor [93].

This background discussion on the inter-relationship of glass chemistry to structure will served to define the key optical properties that dictate material selection when considering materials for use in optical designs for specific components and systems. How these properties influence the selection of that optical material and its fabrication into an optical component, is discussed in the next section.

1.3 Manufacturing of Infrared Optical Elements

In order for an optical material to be used in optical imaging systems it must first be shaped into the appropriate form of use. For lenses, this means the material must be shaped with a certain curvature to refract the wavelength of light desired. In addition to determining how the materials' optical properties will affect its optical performance, the materials' thermal and mechanical properties must also be considered to determine the viability for production.

Chalcogenide glasses offer new manufacturing challenges compared to traditional oxide glasses due to their poor thermal and mechanical properties, but these effects can be partially mitigated through compositional design [101]. Additionally the elements in chalcogenide glasses are often carcinogenic and require special handling and disposal procedures to avoid contamination. The main production methods of chalcogenide glasses remain the same as for oxide glasses (with some specific attention to slurry chemistry and pH), including traditional methods such as laborious and wasteful grinding and polishing, whereas newer manufacturing methods include single point diamond turning (SPDT) and precision glass molding (PGM).

The traditional grinding and polishing techniques can fabricate spherical lens elements with tight tolerances, and in high volumes. However the performance of these spherical lens elements do not match that of aspherical lens elements. To meet the demands for lighter, cheaper, or more compact systems, design has shifted toward the use of aspheric or freeform optical elements [102-104]. While beneficial in terms of optical function in fewer components, manufacturing times and costs are usually larger. These elements present new fabrication challenges as one or both of their surfaces deviate from a spherical shape, and require non-traditional fabrication methods for production as well as more cumbersome metrology techniques to confirm accuracy to design target.

Both SPDT and PGM can produce elements that meet or exceed the tolerances of traditional grinding and polishing, but have the added flexibility to tackle these newer geometries. Tool wear issues with diamond turning of brittle materials such as glass, can also be a limiting factor in the viability of SPDT for aspherical lens elements [105].

Precision glass molding (PGM) machines work through a fairly simple process. Glass samples are placed in between two molds and heated to a temperature above their glass transition temperature, typically corresponding to a viscosity of 10^{10} Pa ·s. A constant force is then applied to the molds to force the glass to take the mold's negative shape. Glass samples are then cooled down to room temperature and removed from the molds. The resulting molded sample is typically a lens that requires no additional fabrication steps (aside from cleaning and/or optional coating) before sale or use. The process can be visualized in Figure 1.8, obtained from [106].

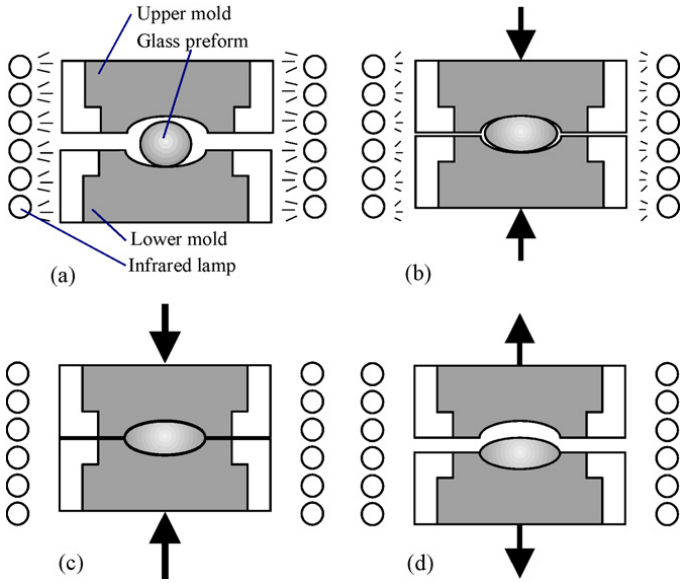

Figure 1.8 – Schematic of the precision glass molding (PGM) process: (a) heating, (b) pressing (or molding), (c.) annealing, and (d) cooling [106].

Precision glass molding (PGM) machines have been documented as a viable alternative for fabricating spherical and aspherical lenses as well as microlens arrays [107,108]. These PGM machines have shown the ability to mold large precision aspherical lenses with surface variations and irregularities comparable to or better than lenses produced using

convention methods [102]. Results on the importance of individual process parameters have been established by several other authors: including force-displacement relationships [109], cooling rate relationships to refractive index [110], and sticking between the glass and mold as a function of cooling times, pressing times, and pressing forces [111].

In order to produce a high quality chalcogenide glass for infrared optical imaging systems, both the materials bulk properties as well as how that material responds to current fabrication techniques must be taken into account. A material that cannot be cost-effectively fabricated into a practical shape is not useable no matter how superior the envisioned optical performance.

1.4 Choice of GeAsSe Ternary

The GeAsSe ternary glass forming system was chosen for target composition analysis for several practical reasons. Before detailing which specific compositions were chosen for this analysis, an overview of those justifications will be presented.

The primary reason for selecting the GeAsSe ternary system is that it possesses a large, stable glass forming region. Along the AsSe binary, stable glasses have been reported from pure Se, up to compositions with more than 50 at% As [38-50]. Compositions with higher As content than this have been shown to crystallize or separate into multiple phases. Additionally along the GeSe binary, compositions have been reported beyond a maximum Ge content (atomic %) of $Ge_{40}Se_{60}$ [75,112,113]. For truly ternary compositions, those which contain Ge, As, and Se, the reported glass forming region has been compiled from several sources and can be approximated in Figure 1.9. When compositions are not along

the edges of the glass forming region, the resulting glass is expected to be a good glass former that is resistant to crystallization and only contain one homogeneous phase of glassy material.

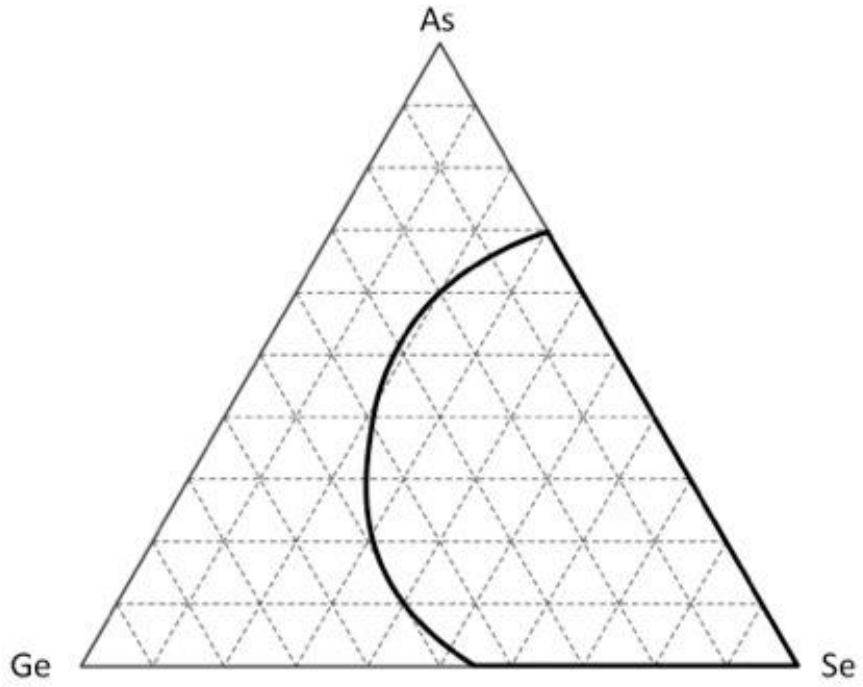

Figure 1.9 – Approximate glass forming region for GeAsSe ternary

Another reason for the selection of this subset of glasses is their current availability as commercial glasses. As detailed in Section 1.2.1, there are a small number of AsSe or GeAsSe compositions commercially available from several manufacturers. While the nominally nine (9) commercially available compositions can be used to satisfy basic design criteria, the lack of available glasses with significant optical and non-optical property variation hinders development of novel optical systems and allows for development of novel compositions to fill the voids.

Both commercial data sheets and peer reviewed journal articles have reported the optical performance of AsSe binary and GeAsSe ternary glasses. In general, these glasses possess a broad transmission window extending from near- or short-wave infrared (NIR/SWIR) through mid-wave (MWIR) and long-wave infrared (LWIR) wavelengths, high linear and non-linear refractive indices, and a variation in index with temperature, dn/dT, that can vary over large values depending on the composition [30-35]. In fact in a small compositional region along the AsSe binary alone, glasses have been shown that exhibit a dn/dT that rapidly and linearly change from positive to negative [31,33]. Aside from commercial data sheets, there is definite lacking of refractive index data on these glasses, let alone the spectral and thermal derivatives of the index, as shown in Figure 1.5 for Ge (Section 1.2). This leaves open the possibility for research to inform the community on the optics of GeAsSe glasses.

While these glasses exhibit extremely interesting optical properties (namely the zero or near zero dn/dT), their thermal and mechanical properties are markedly poor. Their low transition temperatures, high thermal expansions, and soft surfaces present many issues during the manufacturing and coating processes, and can also limit their potential use in optical systems. Thus it is important to understand how compositional variations in these GeAsSe glasses can influence the properties related to manufacturing as well as optical performance in the effort to design compositions with novel functionality.

1.4.1 Selection of GeAsSe compositions

The foundation for this study was to analyze how additions of Ge would simultaneously affect the optical properties of binary AsSe glasses, while also enhancing the thermo-

mechanical stability of the glasses. As mentioned in Section 1.2.3, Ge has been shown to improve the thermal and mechanical properties of AsSe glasses [66]. While the thermal and mechanical properties of the glass have been analyzed in part, the effect of Ge on the optical properties had not been adequately studied.

In an effort to improve upon the three commercially available binary glasses, three binary AsSe compositions were selected to serve as "analog" starting compositions. The three compositions are: $As_{40}Se_{60}$ (analog to Schott's IRG 26 [35]), $As_{35}Se_{65}$ (analog to Amorphous Material's AMTIR5 [31]), and $As_{30}Se_{70}$ (analog to Amorphous Material's AMTIR4 [31]). The network-strengthening Ge was added to each of these three binary glasses without changing the As:Se ratio to create tielines of the form $(As_{0.40}Se_{0.60})_{100-x}Ge_x$, $(As_{0.35}Se_{0.65})_{100-x}Ge_x$, and $(As_{0.30}Se_{0.70})_{100-x}Ge_x$ tielines where x={0, 5, 10, 15, 20} for the first tieline and x={0, 5, 10, 15, 20, 25} for the other two tielines. The compositions analyzed in this study are listed in Table 1.3, and shown on the GeAsSe ternary in Figure 1.10. Because of the high number of unique compositions and the similarities between them, the compositions have been given short-hand Sample IDs, and the three tielines will also be color coded for easier analysis: black will correspond to the $(As_{.40}Se_{.60})_{100-x}Ge_x$ tieline, red for the $(As_{.35}Se_{.65})_{100-x}Ge_x$ tieline, and blue for the $(As_{.30}Se_{.70})_{100-x}Ge_x$ tieline.

Table 1.3 – Compositions analyzed and their designated Sample IDs

Ge (at %) as batched	As (at %) as batched	Se (at %) as batched	Sample ID	MCN
$(As_{0.40}Se_{0.60})_{100-x}Ge_x$ tieline				
0	40	60	40_60_0	2.40
5	38	57	40_60_5	2.48
10	36	54	40_60_10	2.56
15	34	51	40_60_15	2.64

20	32	48	40_60_20	2.72
$(As_{0.35}\ Se_{0.65})_{100-x}Ge_x$ tieline				
0	35	65	35_65_0	2.35
5	33.25	61.75	35_65_5	2.43
10	31.5	58.5	35_65_10	2.52
15	29.75	55.25	35_65_15	2.60
20	28	52	35_65_20	2.68
25	26.25	48.75	35_65_25	2.76
$(As_{0.30}\ Se_{0.70})_{100-x}Ge_x$ tieline				
0	30	70	30_70_0	2.30
5	28.5	66.5	30_70_5	2.39
10	27	63	30_70_10	2.47
15	25.5	59.5	30_70_15	2.56
20	24	56	30_70_20	2.64
25	22.5	52.5	30_70_25	2.73

The final endpoints of these three tielines were chosen so that the mean coordination number (MCN or <r>) of that glass was greater than 2.67. A glass' average coordination is calculated through Equation 4:

$$< r > = \frac{4x + 3y + 2z}{100}$$

Equation 4

where x, y and z are the atomic percentages of Ge, As, and Se, respectively. The multiplicative weighting factors are representative of each constituent's average number of bonds, relying on the assumption each Ge atom would have four (4) bonds, each As atom three (3), and each Se atom two (2) bonds. The basis for this stems from the 8-N rule, where N is the number of valence electrons in the atom.

Several authors have documented a "percolation threshold" when the MCN = 2.4 that corresponds to a local maximum or minimum in certain properties in binary systems [67,68]. Additional authors have observed a second transition at a MCN = 2.67 [40], which

can also correspond to a local extrema or inflection point. The decision was made to increase the Ge content to a point where the MCN is past the potential transition at 2.67, a priori.

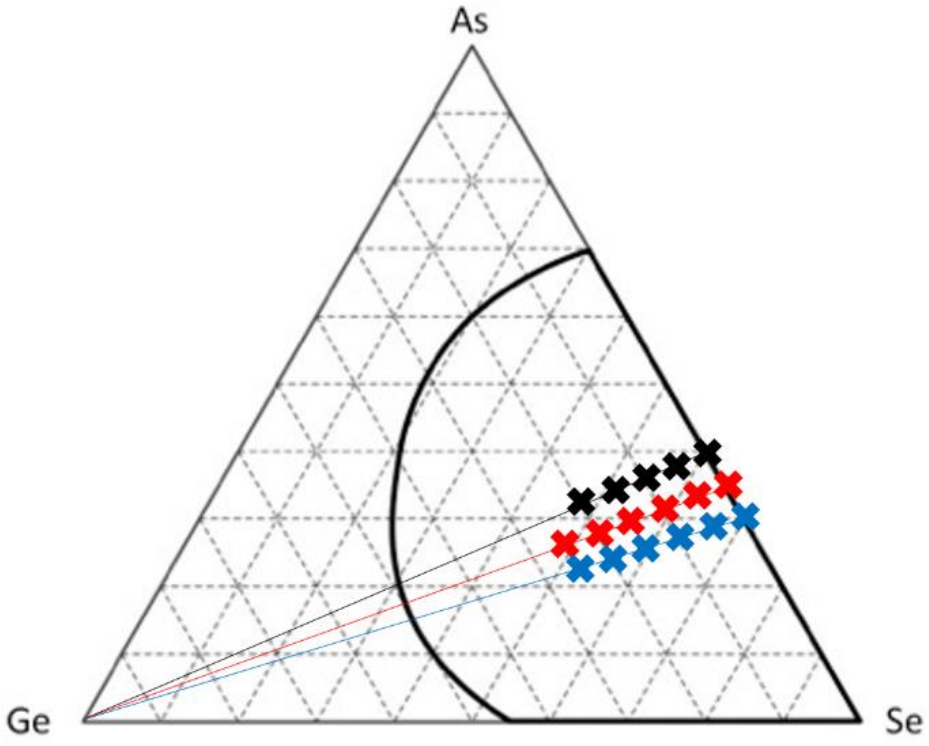

Figure 1.10 – Selected GeAsSe compositions approximate glass forming region bolded.

1.5 Goals for this Dissertation

This chapter has introduced the current state of infrared (IR) materials, highlighted the lack of diversity in commercially available material types and properties, and highlighted some of the methods used to manufacture IR optical components. Compositional design of optical properties has been proposed as a suitable method to overcome the lack of diversity,

and a specific glass forming system (GeAsSe ternary) has been chosen to begin this investigation of compositional design.

The overall goal for this dissertation is to develop a method of compositional design for the optical properties of chalcogenide glasses and to identify and evaluate novel compositions that may exhibit unique properties and are suitable for commercial production. It is hoped that this work will help to fill in some of the present gaps of commercially available IR materials and aide in the production of novel IR systems. While this work will specifically focus on the GeAsSe glass-forming system, the principles can be theoretically be adapted to additional glass-forming systems.

There are two main tasks that must be accomplished along the way to achieving the overall goal of this dissertation. First, novel equipment must be designed, constructed, and characterized in order to provide the necessary optical property information for analysis. Then, glasses must be fabricated and characterized via optical and non-optical methods, and the data must be presented in a way that allows for coherent data analysis.

After the completion of these two tasks, there are several questions which need to be answered during the analysis of the data:

- Is there a link between optical properties, such as the index and dn/dT, and non-optical properties that can allow for easier prediction of the difficult to measure optical properties?
- How will compositional variations for the sake of optical tunability affect the physical properties which dictate a materials' response to manufacturing processes?

- Are there compositions within the GeAsSe ternary that can produce a zero dn/dT that will offer better thermo-mechanical stability to the current commercial options?

This dissertation will seek to accomplish these tasks and answer these questions in order to satisfy the overall goal of this dissertation: to develop a method of compositional design for the optical properties of chalcogenide glasses to aide in the creation of novel IR materials for IR optical systems. Specifically, Chapter 2 will present the necessary procedures and methodology for the fabrication and characterization of these materials, and Chapter 3 will present results obtained from the characterization methods. Chapter 4 will present work done to construct and characterize novel metrology equipment and present results from said equipment. Finally Chapter 5 will present a unique, time-dependent optical phenomenon observed in chalcogenide glasses.

Chapter 2

Experimental Procedures and Methodology

This chapter discusses the preparation, fabrication, and testing of the GeAsSe glasses defined and discussed in Chapter 1. Experimental methods for optical property measurements (specifically refractive index and thermo-optic coefficient) will be the focus of Chapter 4, and not discussed here. The non-optical methods discussed here are crucial to determining appropriate manufacturing practices and confirming glasses fabricated here fall within acceptable ranges established in literature.

2.1 Preparation of the Bulk GeAsSe glass

All materials investigated in this study were approached as if they were novel experimental materials. As such, each composition was subject to analysis to determine the relevant material, mechanical, and optical properties necessary for the overall characterization of a novel material. The specific criterion for a new material depends heavily on the application for which it is intended. When a new material is being designed to fill a specific need, one overarching question must be asked during analysis: does this material meet the numerous criteria necessary for the intended applications?

2.1.1 Batching, melting, quenching, and annealing

All previously mentioned glasses along the three tielines were fabricated using a standard chalcogenide melt-quench protocol [38]. Specific to this study, elemental Ge, As, and Se (Alfa Aesar, minimum 99.999% purity) were individually weighed out in their appropriate

ratios in a glovebox with a N_2 atmosphere and placed in fused silica tubes (10 mm inner diameter) to create 25g batches. Few, select compositions were also melted in "large melts", where the batch size is increased to 250 g and the inner diameter of the fused silica tubes is increased to 30 mm. The elemental starting materials were weighed out to an accuracy of ±0.005 mg, which translates to an approximate "batch sheet" error of 0.1 atomic% for each element. After the raw materials have been placed in the silica ampule, a vacuum fixture was then placed on the end, and the "batch" was then heated to 90 °C and held under mild vacuum for ~30 min. The evacuated tube was sealed-off using an oxygen-methane torch to create a sealed ampule for melting. The ampule was placed in a rocking furnace (Barnstead Thermolyne 21100) at room temperature. The rocking furnace was increased to a melting temperature of 750 °C, at a rate of 2.5 °C /min, and held for ~16 hours. The following day, the rocking of the furnace was halted and the temperature of the furnace was decreased to 650 °C at a rate of 2.5 °C /min. The melt was then quenched to a temperature below T_g with forced air. The resulting glass was then placed in an annealing furnace (Barnstead, Termolyne 48000) for 24 hours at 40 °C below the corresponding glass transition temperature. Forced air was found to be necessary for several compositions to ensure the silica tube and chalcogenide glass inside would not crack during annealing.

After annealing, the chalcogenide glass was removed from the silica tube. Several slices measuring between 2-4mm in thickness were cut from each glass "boule", as well as one rod measuring 12-20mm in thickness, using a diamond tipped low-speed circular saw (Buehler Isomet Low Speed Saw). Additional pieces were set aside from each melt to be

ground into a fine powder using a mortar and pestle for differential scanning calorimetry (DSC) analysis.

The small disks and were then polished by hand using a single sided polisher (Buehler Ecomet 250). First a coarse grit pad was used to quickly grind the samples to an approximate final thickness of 2mm, and to remove any cutting marks during the slicing process. The samples were then fine ground with subsequent steps, each consisting of smaller grit sizes than the last. After grinding, the samples were then polished using a cloth pad and an alumina slurry with a particle size of 0.3 μm. The same process was repeated for the longer rods of glass, save for the initial grinding step to reduce the total length.

2.2 Material Characterization - Experimental Methods

A summary of the properties investigated in this experimental section have been outlined in Table 2.1 along with the specific equipment being used, and any specific sample preparations and /or geometries needed for the analysis. The sections below can be referred to, to gain an understanding of the fundamentals of the experiment in question and to understand any other pertinent parameters that could not be contained in Table 2.1.

Table 2.1 – Summary of the equipment used in this study, as well as pertinent information for sample fabrication and preparation.

Equipment Name	Spectral or Temperature Range or Wavelengths	Property Measured	Sample Form Needed	Amount of Sample Needed (per run)	Sample Width Needed (mm)	Sample Thickness Needed (mm)
Bruker Senterra MicroRaman	λ_{exc} = 785 nm	Vibrational Energy	Polished Slice	1 Piece	>2 Typically 10	>1 Typically 2
Metricon 2010/M	30°C – 90 °C PNNL: 3.4µm, 4.5 µm, 5.4 µm, 7.78 µm, 10.6 µm UCF: 4.515 µm	Refractive Index, dn/dT	Polished Slice	1 Piece	>7 Typically 10	1 to 4 Typically 2
ZYGO NewView 8300		Surface Roughness	Polished Slice	1 Piece	>1 Typically 10	>1 Typically 2
TA Instruments SDT Q600		Weight Loss, Tg	Powder	30-40 mg Typically - 125 mesh	N/A	N/A
Thermtest TPS2200		Thermal Conductivity	Polished Slice	2 Pieces	>9 Typically 10	> 2.75 Typically 3
TA Instruments 2940 TMA		Thermal Expansion, Softening Temp	Slice	1 Piece	2 to 10 Typically 3	>5 Typically 10
AE Adams PGW Balance		Density	Slice	1 Piece	>5 Typically 10	>2 Typically 2
Shimadzu DUH-211S		Vickers Hardness	Polished Slice	1 Piece	>5 Typically 10	>1 Typically 2

2.2.1 Differential Scanning Calorimetry (DSC) and Simultaneous DSC/TGA (SDT)

A differential scanning calorimeter (DSC) is an instrument that measures the heat flow into and out of a sample. Typically a DSC system design utilizes a cell with two sample pads: one for sample to be measured and another to serve as a reference. The system works by measuring the heat flow needed to keep the two samples at the same temperature during a ramp in temperature. The signals between the sample and reference are then compared to obtain material properties such as the glass transition temperature (T_g), crystallization growth (T_x) and melting (T_m) temperature(s), relative nucleation and crystallization rates (I, U) [114], as well as the material's heat capacity (C_p).

One variant of the DSC also incorporates thermogravimetric analysis (TGA), which measures a sample's weight during heating, to yield simultaneous results including the onset of volatilization or dehydration in bulk samples as well as solutions [84,115-117]. This system is often referred to as simultaneous DSC or DTA associated with the specific simultaneous differential thermal technique (SDT). This is particularly useful when considering use of a material in an extended temperature environment or in a manufacturing environment involving broad thermal excursions or cycling. Deviations beyond a thermal stability regime can lead to change in composition and thus, optical properties.

A representative SDT thermogram is shown in Figure 2.1. The figure contains two distinct curves: the heat flow (green) into the sample and the derivative of the heat flow (blue) into the sample. The glass transition temperature of a glassy sample is defined as the inflection point of the first endothermic feature in the heat flow signal. This can also be calculated as the minimum of the derivative of the heat flow signal, and is noted in Figure 2.1 for reference.

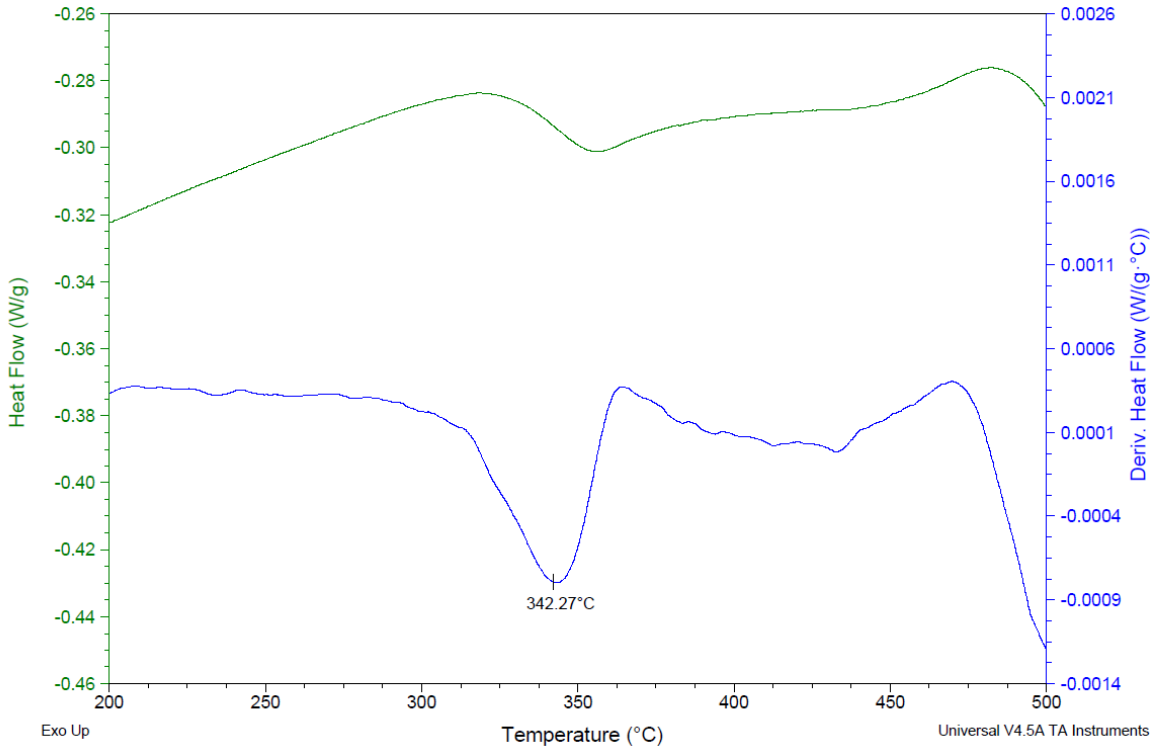

Figure 2.1 – Standard DSC thermogram of a GeAsSe glass (30_70_25), including the measured heat flow into and out of the sample (green) and the derivative of this signal (blue). The T_g of the glass is noted in the figure and is calculated from the minimum of the derivative of the heat flow.

Bulk samples for this study were crushed into powder and 15-25 mg of the sample power was weighed in an alumina pan. The sample was heated at a rate of 10°C·min^{-1} to T_g+25°C to maintain a similar thermal history for each sample. The sample was then cooled down to 50°C before heating again at a rate of 10°C·min^{-1} and continuing until 3% of the initial weight was lost through volatilization. Specific to this study, T_g was calculated as the temperature corresponding to the minimum in the first derivative of the heat flow for the first endothermic feature *upon reheating*.

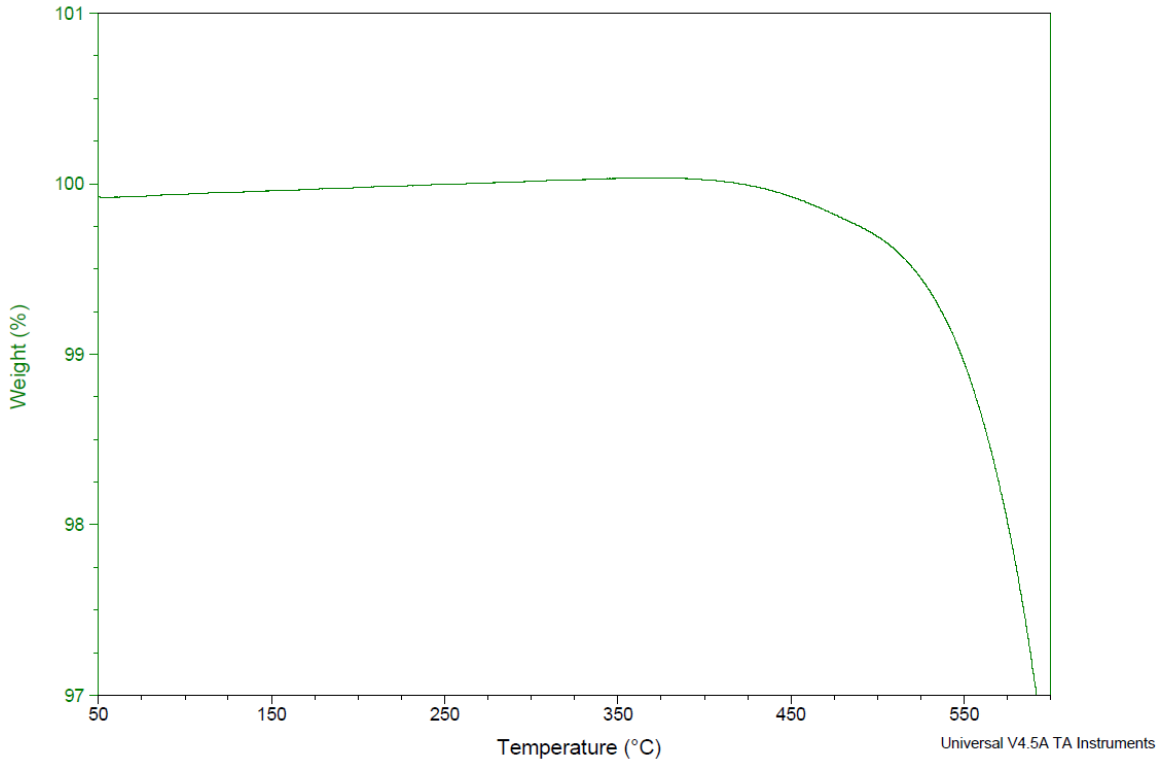

Figure 2.2 – Measured weight of a GeAsSe sample (30_70_25) as a function of temperature, as measured by an SDT. The "upper use temperature" of a composition is defined as the temperature corresponding to 1% total weight loss.

A representative plot of a samples weight during a temperature ramp up to its upper use temperature is shown in Figure 2.2, and is the same sample as previously shown in Figure 2.1. The maximum upper use temperature was calculated as the temperature corresponding to 1% weight loss. The reported error on the T_g and upper use temperature was obtained through the standard deviation of 5 unique runs from of a representative bulk sample, and was found to be ±2°C in both cases.

2.2.2 Thermo Mechanical Analyzer (TMA)

A thermomechanical analyzer (TMA) is an instrument that measures relative and absolute changes in a sample's length, typically as a function of temperature or time. The most

common information gathered from a TMA is a material's coefficient of linear thermal expansion (CTE). The CTE (α) is obtained by taking the slope of the linear dimension change vs. temperature curve $\left(\frac{dL}{dT}\right)$, and dividing by the initial length (L_i) as shown in Equation 5. In addition to the CTE, a TMA can also be used to measure the dilatometric T_g of a glass, as well as the dilatometric softening point (T_d). A TMA curve of a representative sample is shown in Figure 2.3.

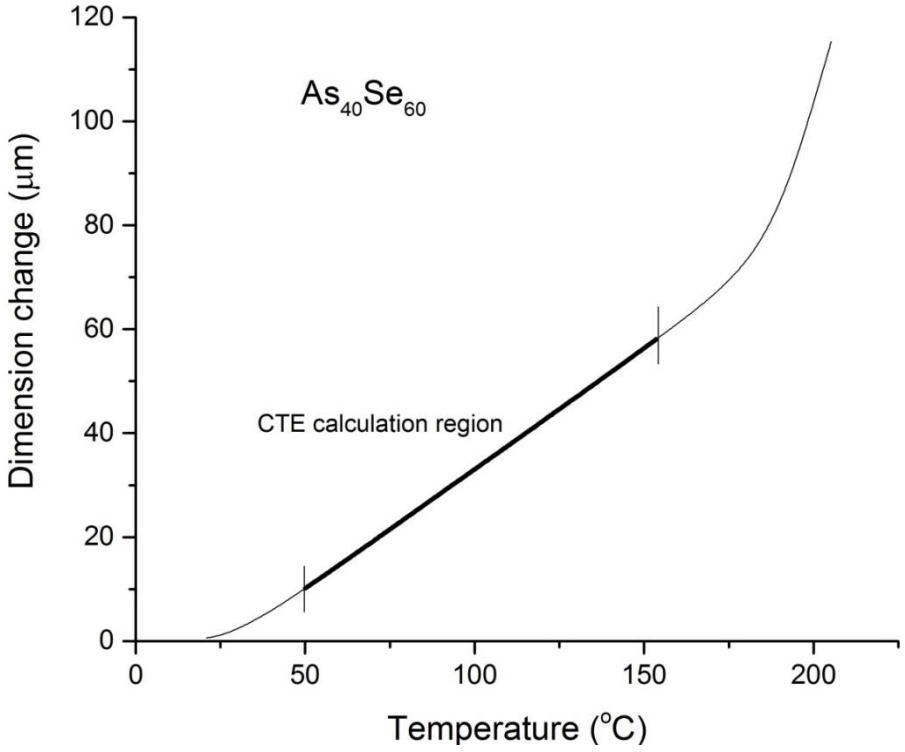

Figure 2.3 – Linear dimension change as a function of temperature for a sample of $As_{40}Se_{60}$ measured at 3°C·min^{-1}. The bold region signifies the region used in the calculation of the Coefficient of Thermal Expansion (CTE).

For this study, cylindrical samples measuring 10 mm in diameter and approximately 15 mm in height were used, and all heating rates for the experiments were held constant at 3 °C·min^{-1}.

$$\alpha = \frac{1}{L_i}\frac{dL}{dT}$$

Equation 5

The region used to calculate the CTE is shown in Figure 2.3 and is defined for this study as the range between 50 °C and 0.8*T_g, with the T_g being determined through DSC or SDT analysis. The maximum temperature for the TMA is typically set to T_g + 25 °C, so that the glass does not significantly deform, or slump, under its own weight. One run of room temperature up to T_g + 25 °C is used to reset the thermal history of the samples, and the reported CTE is taken as the average of the CTE from the next three consecutive runs up to the maximum temperature. The error was obtained by averaging the standard deviation of the linear fitting of these three runs from a representative sample and was found to be ±1.0 ppm ·°C^{-1}.

The TMA can also be used to characterize micron-scale relaxations in chalcogenide glasses that occur at temperatures slightly below the T_g over the course of hours to days. These structural relaxations are pivotal in understanding how a chalcogenide glass may change shape after a fabrication process such as precision glass molding [1,118]. These specific processes will not be discussed in this analysis, but remain an important topic for IR glass manufacturers.

2.2.3 Vickers Microhardness, H_V (GPa)

The Vickers Hardness of a material is a measure of that material's ability to resist plastic deformation upon indentation of a Vickers indenter. The Vickers Indenter is made from diamond and has a pyramidal shape with a square base. The indenter is pushed into the

material's surface, and held in contact with the surface for a set amount of time and with a constant force. The resulting indentation in the material surface is then measured under a microscope objective. A typical Vickers indentation is shown in Figure 2.4.

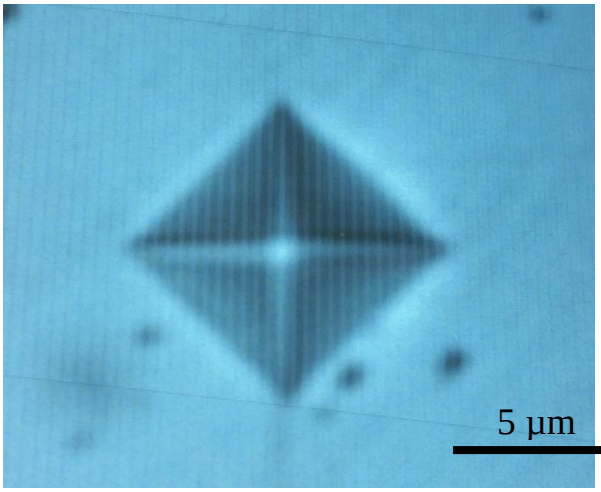

Figure 2.4 – Indentation of a Vickers Hardness indentor on a GeAsSe glass with an indentation force of 100mN.

When measuring glassy materials, indenting the surface with too large of a load can cause in crack formation and propagation, potentially leading to incorrect measured hardness values [50]. A polished sample of $As_{40}Se_{60}$ was indented with increasing loads, and the hardness was measured to determine the appropriate load for analysis and to determine the threshold load for crack formation and propagation. Figure 2.5 shows the measured hardness for an $As_{40}Se_{60}$ sample as a function of indentation load, and highlights the threshold load for crack formation / propagation.

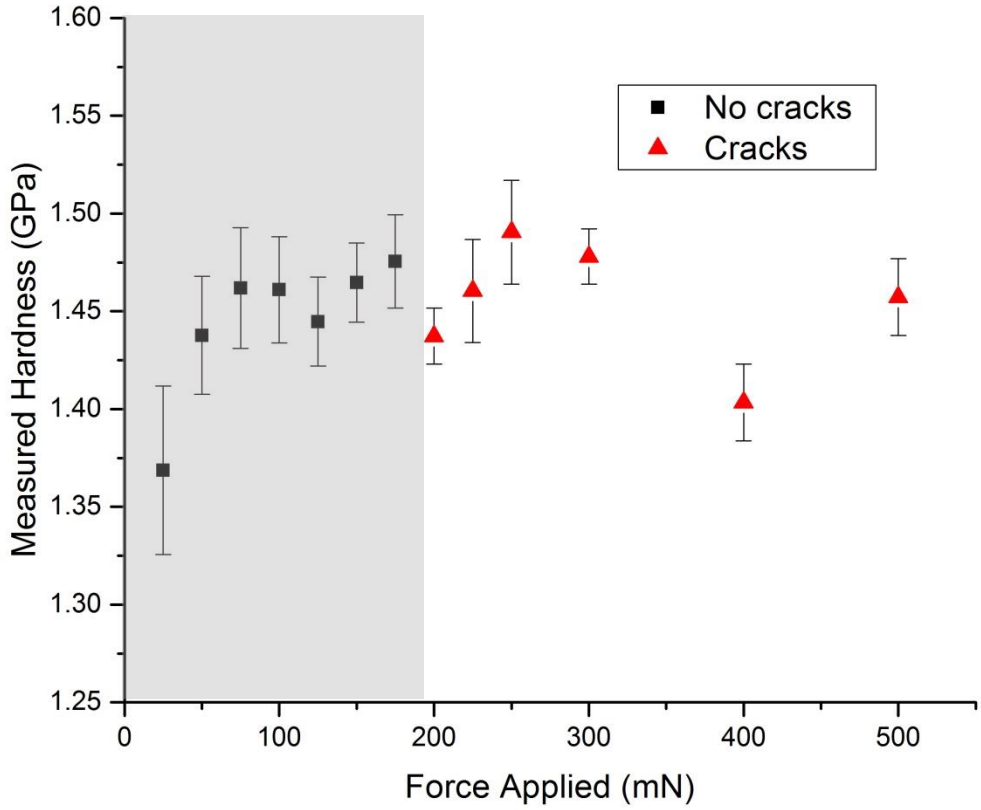

Figure 2.5 – Measured Vickers Hardness in GPa as a function of indentation force for a sample of $As_{40}Se_{60}$. Black data points indicate that no cracking occurred, while red data points indicate that cracking did occur.

Based on these results all samples for this analysis were indented with a 100 mN load for a hold time of 10 seconds using a Shimadzu DUH-211S Dynamic Ultra Microhardness Tester with a Vickers indenter. The reported hardness values are obtained through averaging calculated hardness on ten unique indentations. The error is reported as the standard deviation of the same ten indentations and is uniquely obtained for sample measured for each sample.

2.2.4 Density

Density is a measure of the mass occupying a unit volume of a material. The density of a material is mathematically defined as the mass of the material divided by the volume it occupies. The density of the glasses was determined using the Archimedes method on an Aaron Balance (AE Adams PGW Balance) utilizing deionized water as the immersion medium. A 1-inch single crystal silicon cube was used as reference to verify the accuracy and repeatability of the measurement technique. The samples previously described for thermal expansion measurements provided a large enough sample size to minimize the error. All density measurements were performed on samples prior to measuring the thermal expansion to avoid measuring the effect of thermal history changes in the process.

2.2.5 Raman Spectroscopy

Raman scattering is a type of inelastic scattering of monochromatic light that gives information to the types of vibrational modes within a material. During the scattering process, the vast majority of photons are elastically scattered, known as Rayleigh scattering, and only a small fraction of photons are inelastically scattered, meaning the scattered photon has a lower energy than the initial photon. Raman scattering was first experimentally observed by C.V. Raman, which later earned him the 1930 Nobel Prize in Physics.

During the inelastic scattering process, a portion of the incident photon's energy interacts with low frequency vibrational states between certain molecules within the sample. Different atoms / molecules have different characteristic vibrational states, and will "leech" different amounts of energy from the incident photon, referred to as the Raman shift.

Systematic experimental investigations coupled with computer simulations have produced a large database of characteristic Raman shifts for a wide variety of materials and vibrational states.

The spectra of polished samples were collected using a Bruker Optics Senterra Raman Spectrometer with an excitation wavelength of 785 nm. The reported Raman spectrum for each sample is an average of data acquired from three spots; each measured using 5 co-additions of 30 seconds.

The data was then normalized by the total integrated area between 165 cm^{-1} and 400 cm^{-1}as described by Musgraves et al. [92]. The Raman spectrometer used in this analysis exhibited increased noise below 165 cm^{-1}, and was filtered out for this reason. The normalized data was then deconvolved using PeakFit software and Raman assignments from relevant literature sources.

The Raman spectra of a representative GeAsSe glass is shown both prior-to and after normalization in Figure 2.6. Additionally an example of the deconvolution is shown in Figure 2.7. The individual bands, dashed lines in Figure 2.7, correspond to specific vibrational modes of As-Se or Ge-Se. Additional information of the specific bands used for deconvolving the signal can be found in Section 3.1. The information gathered from the deconvolved Raman specta will also be used in Section 3.4.3 to highlight the correlation between certain Raman-active bands and physical properties.

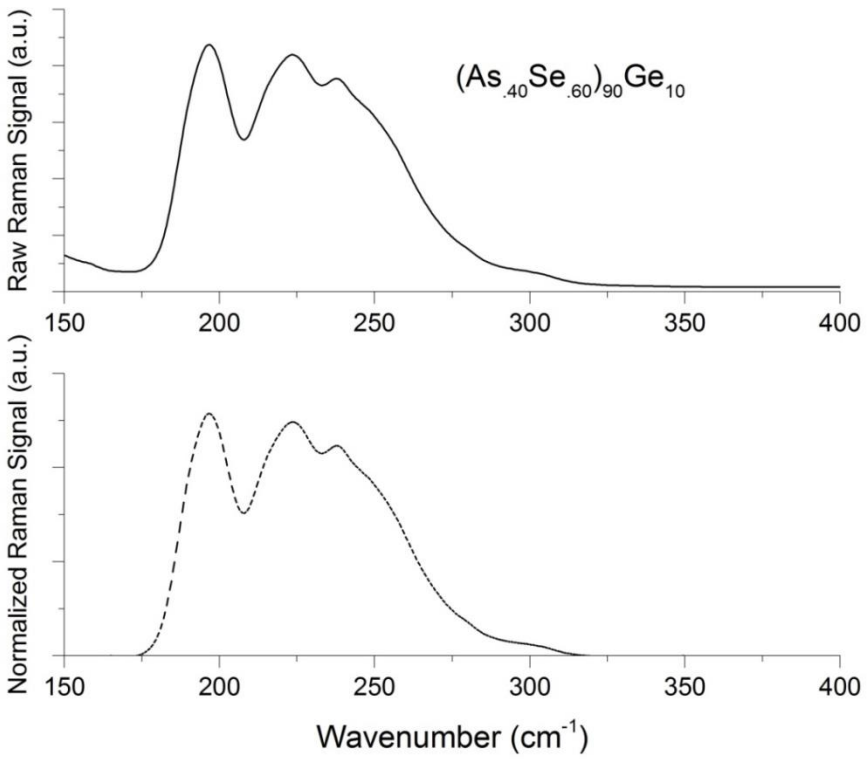

Figure 2.6 – Raman signal from a sample of $(As_{.40}Se_{.60})_{90}Ge_{10}$ prior to normalization (top) and after normalizing to the total integrated area (bottom).

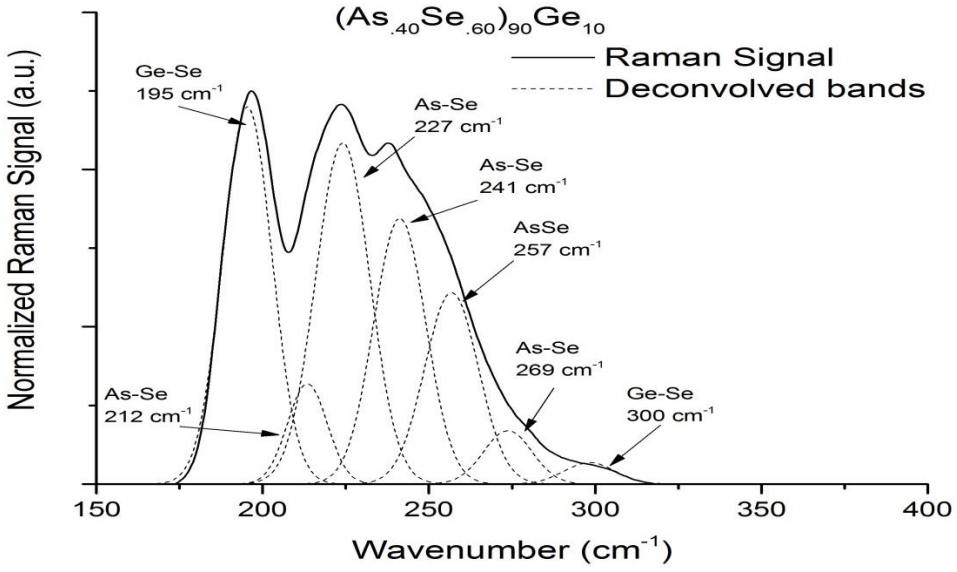

Figure 2.7 – Normalized Raman signal from a sample of $(As_{.40}Se_{.60})_{90}Ge_{10}$ (solid), shown with deconvolved bands (dashed).

2.2.6 Infrared Transmission (FTIR and UV-VIS)

The most basic application of these GeAsSe glasses is transmission of light in bulk, fiber, or thin film form. The glasses in this analysis are largely novel glasses, with unknown transmission behavior. To determine the transmission of the new glasses Fourier Transform Infrared Spectroscopy (FTIR) was used. FTIR utilizes a broad spectral signal to simultaneously collect transmission and absorption data over an equally large spectral range. The broadband light is passed through a Michelson Interferometer where one of the mirrors is attached to a motor for lateral movement. Moving this mirror increases the path length of one of the interferometer's arms and allows for constructive and destructive interference different wavelengths of light. The measured signal is collected in the spatial domain (as a function of lateral movement of the system mirror), then a Fourier transform is used to present the transmission data in the spatial frequency domain (cm^{-1}). The data can them be converted to the wavelength relevant information for optical designers who often prefer to work with units in nm or μm form. This method works in contrast to an Ultraviolet-Visible (UV-VIS) Spectrometer which measures the transmission and absorption over a narrow spectral linewidth and incrementally constructs the transmission and absorption spectra.

The transmission data from FTIR measurements can be used to check for absorptions from impurities and to determine the transmission window limits. Absorptions from impurities are typically present over narrow wavelength regions and decrease the transmission partially or fully. The short-wave FTIR spectrum of the polished samples in this investigation was collected using an FTIR in transmission mode (Perkin Elmer FT-NIR

Spectrometer Frontier). Each sample was measured 5 times, and the signal was averaged across all measurement runs. The short-wave transmission cut-off wavelength ($\lambda_{c/o}$) was defined for this analysis as the wavelength corresponding to a 30% drop in transmission from the maximum measured transmission, i.e. $0.7 \cdot T_{max}$. A typical transmission spectrum for a GeAsSe glass is shown in Figure 2.8, which has been corrected for Fresnel losses and normalized to the maximum transmission. Also highlighted in Figure 2.8 are the regions corresponding to typical absorption bands in GeAsSe glasses.

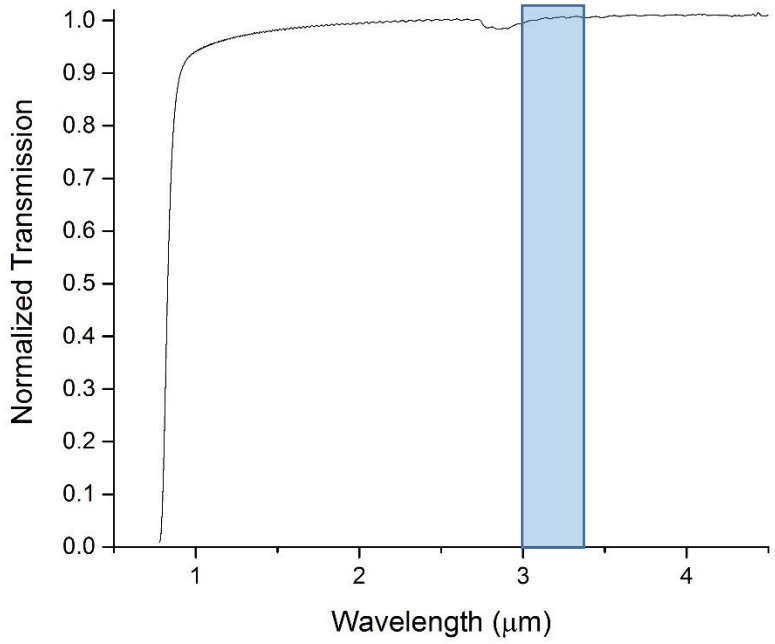

Figure 2.8 – Fresnel corrected and normalized transmission spectrum of an $As_{40}Se_{60}$ sample measuring ~2mm in thickness as measured by an FTIR spectrometer. The highlighted band at ~2.8 μm corresponds to absorptions from O-H impurities [119,120].

2.2.7 Surface Roughness

White light interferometry (WLI) is a non-contact optical method of measuring surface heights of a sample, and is primarily used for obtaining surface roughness and dimensions of features present on a materials' surface, intended or otherwise. As the name suggests, WLI interferometry uses a broadband visible source to create interference patterns on the surface being measured. In a method similar to FTIR spectroscopy, an interferometer with a movable mirror is used during the analysis. The similarities end there, as WLI utilizes a different type of interferometer and captures images of interference patterns projected on the surface of the material, rather than the spectral transmission or reflection of the material.

The surface roughness of the polished samples was measured using a Zygo White Light Interferometer (NewView 8300). The reported surface roughness for each sample is the average of root mean square (RMS) roughness obtained from five measurement locations 0.707 mm^2 in area spread across the sample. A sample image of the white-light interferogram is shown in Figure 2.9, this figure shows the relative height of each "pixel" across the sample, then calculates the peak-to-valley (PV) roughness and root-mean-square (RMS) roughness. There are several lines (slightly different color/scale than immediate surroundings) that traverse the image from top left to bottom right of the image, these lines are scratches in the surface from the polishing process.

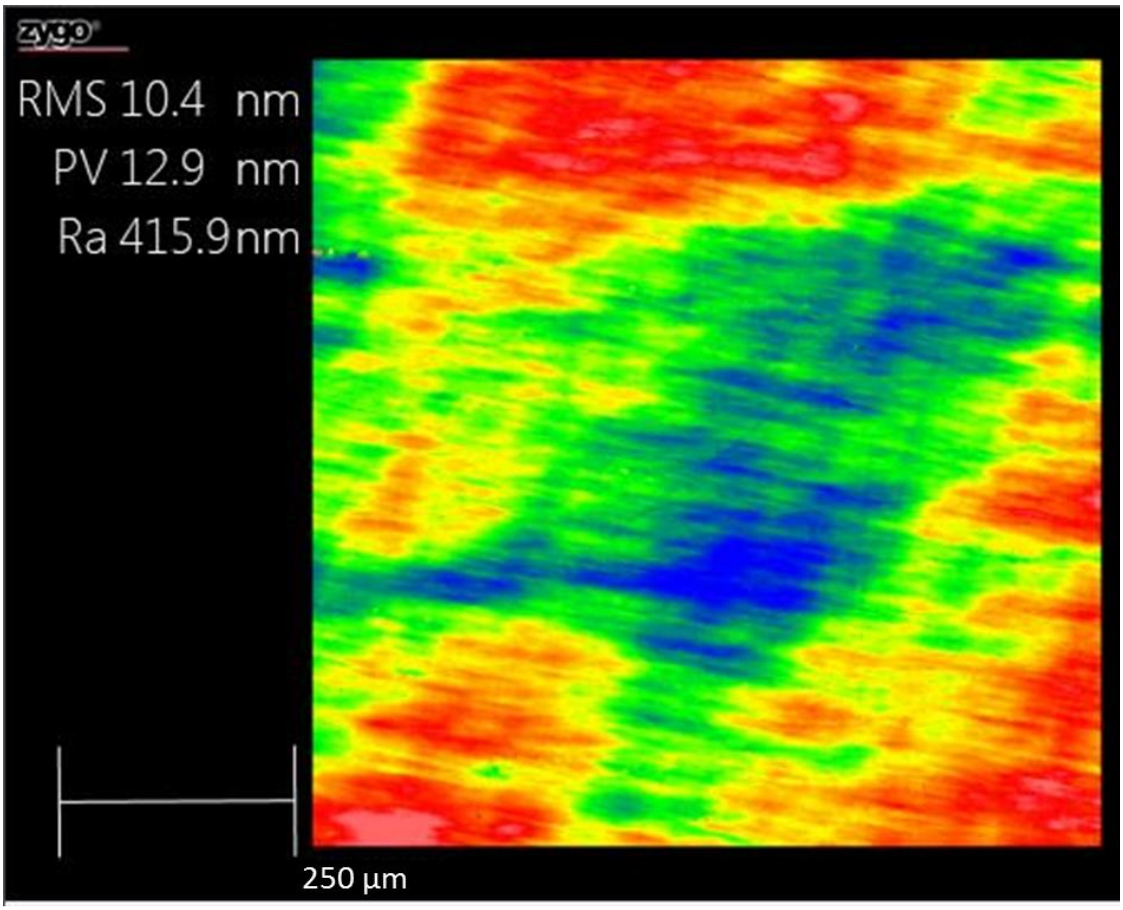

Figure 2.9 – Surface profile interferogram of a GeAsSe glass surface (over a 0.707 mm^2 area) as measured by white light interferometry (WLI). The root mean square, and peak-to-valley roughness is shown in the upper left corner.

2.3 Conclusions

This chapter has discussed the necessary procedures to melt chalcogenide glasses, fabricate samples, and characterize these samples using well understood characterization techniques. The following chapter will present the results of the characterization techniques on the chalcogenide glasses outlined in Section 1.4.1, and provide analysis for the observed trends.

Chapter 3

Material Characterization Results

This chapter will discuss the results of the non-optical experimental procedures outlined in Chapter 2. Firstly, the structure of these glasses will be presented to establish a foundation on which to discuss the evolution of the optical properties. Then, with the structural evolutions in mind, the remaining properties will be investigated. Specific focus will be paid to the influence of these properties on manufacturing properties, and will be referenced to established results for oxide-based glasses. Finally the collected data in this investigation will be compared to prior literature results to verify the results obtained in this study conform to expected standards.

3.1 Structural Analysis

This section will describe the evolution of structural, physical, and thermal properties across the three tielines. The data throughout this dissertation will be presented in three slightly different methods, with each one highlighting a different aspect of the trends. The first method is based simply on the added Ge (in atomic percentage) to the base AsSe binary glass. This method looks solely on the chemistry of the compositions, i.e. X% Ge, Y% As, and Z% Se, but fails to emphasize the underlying structures and/or global network connectivity. The second method is through calculating the mean coordination number (MCN), which was mathematically described previously in Section 1.4.1. To reiterate, the MCN is a global measure of the network connectivity and is a calculation of the average

number of bonds (coordination) per atom. A considerable amount of work has been performed on characterizing ternary glasses as a function of MCN, and thresholds at certain MCN values (namely 2.4 and 2.67) have been well documented [40,67,68]. Within MCN analysis, two glasses with considerably different chemistry can have identical MCN values.

The final method of characterizing trends along the tielines is through looking at the structures that *should* be present at a given chemistry (composition). Since GeAsSe glasses can have multiple structures at the same time, it is not feasible to investigate trends based on the amount of one structure, nor is it feasible to include all of the structures in one coherent analysis.

In brief summary, the three methods for analyzing the tielines are as follows:

1. Ge concentration – a measure of glass chemistry at a given composition
2. Mean coordination number (MCN) – a measure of network connectivity at a given composition
3. Se-rich/-poor percentage (or excess/deficiency) – a measure of the likely structures at a given composition

Properties will be presented in one of these three methods to demonstrate how either the glass chemistry, the network connectivity, or how structures (types and/or relative amounts) dictate property trends across the tielines. The non-optical properties will be presented primarily in terms of the MCN or the absolute Ge concentration of the corresponding composition. This will be done to show correlation with previously

published data and to discuss relevant trends. Optical data in Chapter 4 will primarily be discussed in terms of the Se-rich/poor % to highlight new findings in the results.

3.2 Structural Characterization - Results

The manner in which the glass constituents (atoms) are arranged in the isotropic glass network gives rise to the resulting glass structure. This structure, which can be analyzed by a variety of tools, specifically using Raman spectroscopy in the present study, varies as the types and relative quantities of the respective constituents change in the glass. The resulting network structure is key to understanding the resulting material's mechanical, thermal, and optical properties.

Chalcogen-rich glasses, such as amorphous Se or binary AsSe with Se content >80 at%, contain extremely long Se chains. This 1D structure is a result of the selenium atom's coordination number of 2, meaning that only two of its six outer shell electrons will participate in bonding, while the other four form two sets of lone pair electrons that do not contribute to the connectivity of the network [67,68]. If a three-coordinated As atom (three unbound valence electrons and one set of non-contributing lone pair electrons) were added to this chainlike structure, a pyramid type structure would form connecting three Se chains to one As, with the remaining lone pair electrons at the "apex" of the pyramid. The process of replacing Se with As (and thus Se chains with AsSe pyramids) gradually shifts the network from 1D to 2D, and once the composition reaches the stoichiometric $As_{40}Se_{60}$ a completely 2D structure of puckered layers held together by weak van der Waals forces is realized [40,67,68]. The three binary AsSe glasses selected for this study yield a structure

comprised primarily of these 2D puckered layers, as they are near stoichiometry, with $As_{40}Se_{60}$ being stoichiometric.

The normalized Raman spectra of the three AsSe binary glasses are shown in Figure 3.1. Vibrational modes observed between 210 and 270 cm^{-1}, relevant to these glasses, are listed in Table 3.1 along with their references. The Raman spectra of the three glasses are similar, showing broad signal response containing several AsSe vibrational modes, and is a direct result of the glasses' structures also being similar. With this background, and prior systematic property changes shown for binary AsSe materials that show quantitative comparison of property changes across compositional tielines [38,40,47,48,83,121] the structural evolution in this glass system with Ge additions are discussed.

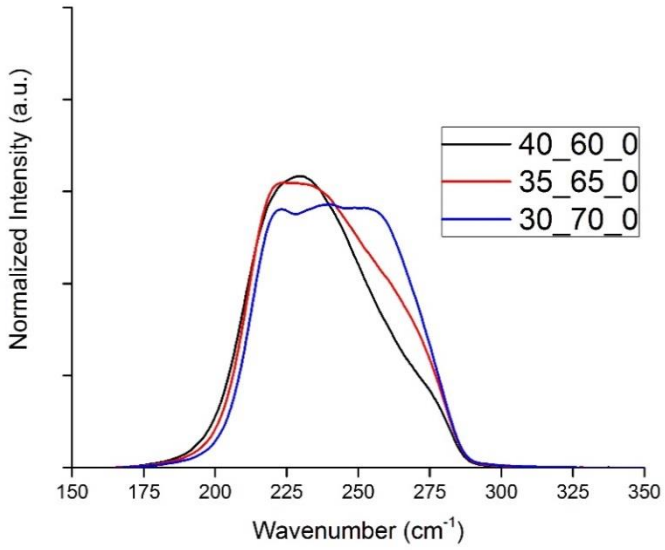

Figure 3.1 – Normalized Raman spectra of the three AsSe binary glasses, measured with an excitation wavelength of 785nm.

The normalized Raman spectra of the three tielines, $(As_{.40}Se_{.60})_{100-x}Ge_x$, $(As_{.35}Se_{.65})_{100-x}Ge_x$, and $(As_{.30}Se_{.70})_{100-x}Ge_x$ are shown in Figure 3.2, Figure 3.3, and Figure 3.4. Figure 2.8 (found in Section 2.2.5) shows the normalized Raman spectrum of a representative glass, $(As_{.40}Se_{.60})_{90}Ge_{10}$ (equivalently 40_60_10), with the individual deconvolved bands that create the overall spectrum. The deconvolved bands have been labeled for approximate center wavenumber, and have been labeled with the type of vibration that contributes. More information on the individual bands can be found in Table 3.1.

According to Kaseman et al., the larger difference in electronegativity between Ge and Se, as compared to between As and Se, leads the Ge to preferentially seek bonding with Se [48]. This assertion is supported in Figure 3.5, which shows the change in the total relative contribution from AsSe, GeSe, and SeSe bands in the Raman spectra. The values reported are a summation of the deconvolved peak area of each individual AsSe, GeSe, or SeSe bands, respectively. As more Ge is added to the glass network, there is a steady increase in the contribution from GeSe bands, namely GeSe edge- and corner-shared tetrahedral units [58,122]. These GeSe bands grow at the expense of the AsSe bands as the GeSe units become a significant part of the glass network. The contribution of SeSe bands is also annihilated as the compositions move beyond stoichiometry to become Se deficient.

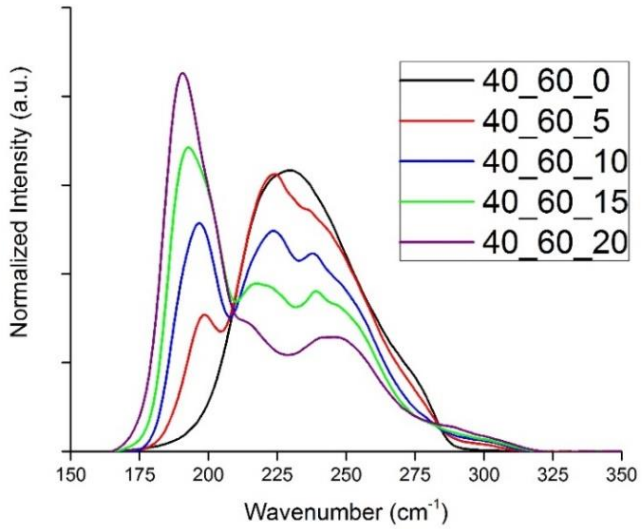

Figure 3.2 – Normalized Raman spectra of the $(As_{.40}\ Se_{.60})_{100-x}Ge_x$ tieline, where x={0, 5, 10, 15, 20}, measured with an excitation wavelength of 785nm.

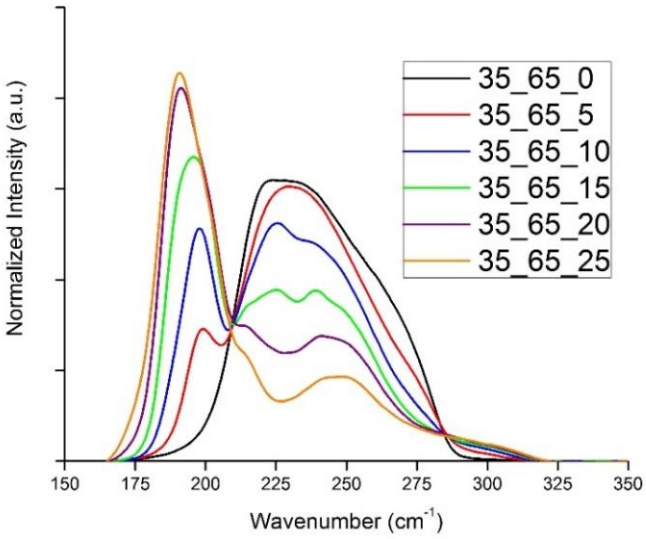

Figure 3.3 – Normalized Raman spectra of the $(As_{.35}\ Se_{.65})_{100-x}Ge_x$ tieline, where x={0, 5, 10, 15, 20, 25}, measured with an excitation wavelength of 785nm.

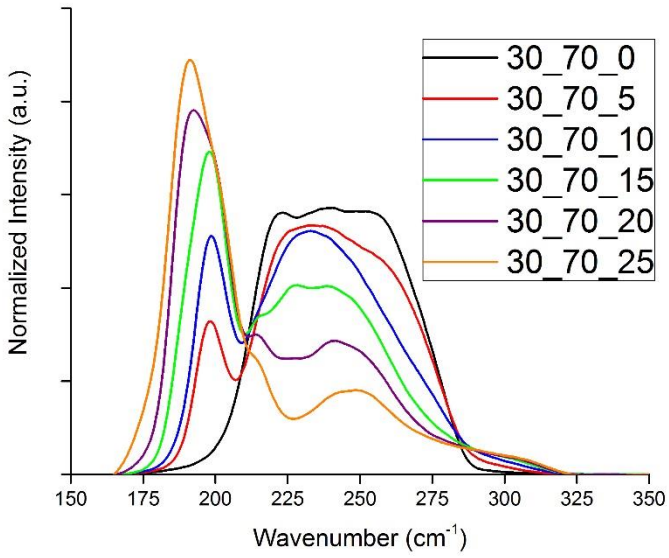

Figure 3.4 – Normalized Raman spectra of the $(As_{.30}\ Se_{.70})_{100-x}Ge_x$ tieline, where x={0, 5, 10, 15, 20, 25}, measured with an excitation wavelength of 785nm.

The newly formed $GeSe_{4/2}$ tetrahedra and their extra, interlayer connectivity, will replace the weak van der Waals forces holding the puckered AsSe layers together with stronger, covalent, interlayer bonds. The addition of Ge leads to more of these structural units which initiates the onset of a fully 3D glass network [40]. Germanium's role in the process is often referred to as "cross-linking" or "polymerizing" the glass network. The simultaneous growth in GeSe bands and decline in AsSe bands shows the mechanism by which the network evolves to yield a more highly coordinated structure, with the addition of 4-coordinated Ge.

Table 3.1 – Raman bands found in GeAsSe glasses, their center positions, and relevant reference information.

Center peak position (cm^{-1})	Peak assignment	Reference
175	$GeSe_{4/2}$ – ethanelike mode	[122]
195	$GeSe_{4/2}$ – corner shared	[58,122]
205	$GeSe_{4/2}$ – edge shared	[58,122]
212	Interaction of the $AsSe_3$ pyramids	[59]
227	As-Se vibration within $AsSe_3$ pyramidal units	[58,69]
241	As-Se vibration	[69]
250	SeSe	[122]
257	As-Se vibration	[59]
269	Interaction of the $AsSe_3$ pyramids	[59]
300	$GeSe_{4/2}$ – ethanelike mode	[122]

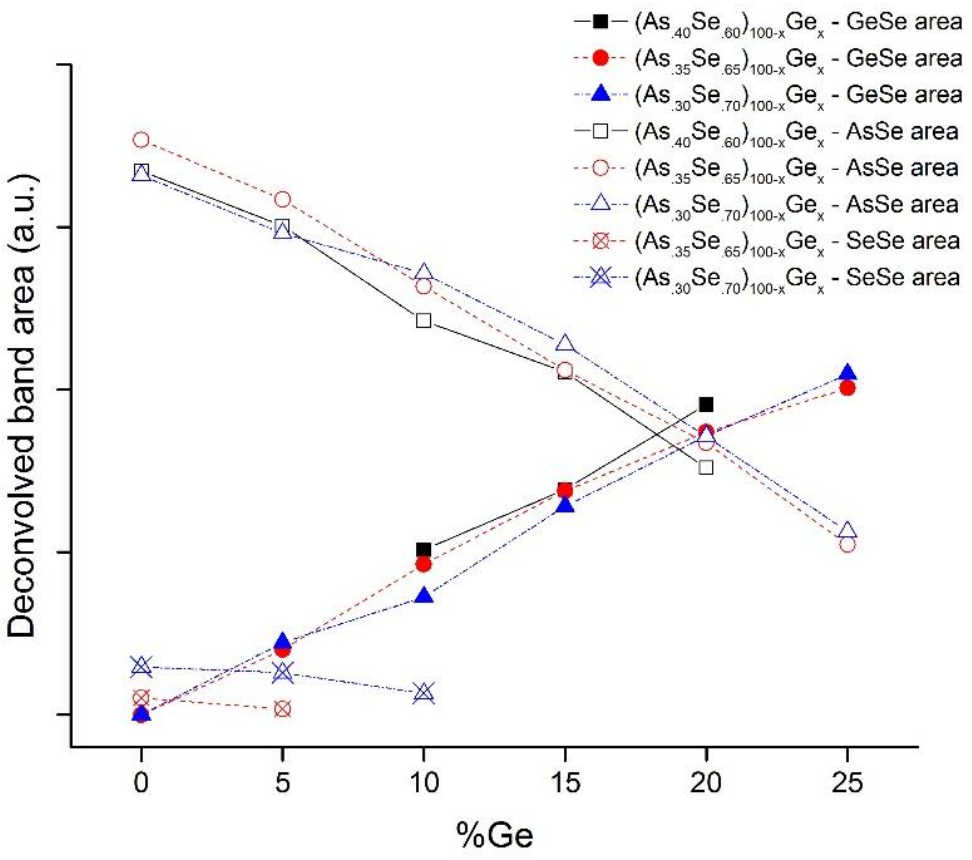

Figure 3.5 – Summation of the deconvolved GeSe bands (solid points), AsSe bands (hollow points), and SeSe bands (hollow points with cross) from Raman spectral analysis as a function of Ge.

3.3 Precursor to Manufacturability

Traditional chalcogenide glass optical manufacturing involves tedious grinding and polishing of a bulk work-piece to remove material until the desired shape is met. Unlike oxide glass loose abrasive processes, fabrication of chalcogenide materials requires specialized handling protocols of slurries and waste, as well as more gradual heating and cooling procedures (i.e., during blocking/de-blocking or generation) where the glass' high(er) coefficient of thermal expansion (CTE) can yield to thermal shock and fracture. While conventional optical fabrication techniques can produce high quality parts, final sample geometries are typically limited to planar or spherical elements. A relatively new method of production, single point diamond turning (SPDT), has been proven to be extremely useful for producing a high quantity of high quality optical elements in spherical, aspherical, and non-rotationally symmetric geometries [123,124]. Chalcogenides, due largely to their low glass transition temperatures lend themselves to hot forming techniques such as extrusion and precision glass molding (PGM) [125]. The latter method of molding, while studied extensively over the past decade are only now becoming commercially viable for making specialized parts (aspheres or diffractive optic elements) for optical systems [1,104,126-128].

As both SPDT and conventional polishing rely on mechanical (and in some cases chemo-mechanical) material removal, one important aspect to consider is the materials' hardness. The relevance of this property in glass has been examined and established in work by Lambropolous and Puttick. Their study showed a favorable correlation between the hardness of oxide glasses and their final optical element surface roughness, for both

grinding and polishing [129] as well as SPDT [130]. Specifically, glasses with a lower inverse root of the hardness values ($H^{-1/2}$), demonstrated lower final surface roughness [129,131,132]. While hardness has been explored, and specifically related to manufacturing processes, there are other important properties that have less of a defined relationship, which will be discussed in the present study.

The material removal in the manufacturing processes results in the need to consider not only the final shape of the piece but any additional thermal aspects that may occur during processing. These thermal effects must also be considered due to the fact that interactions between the work-piece and the slurry/ diamond tip can result in localized heating [130]. As noted above, rapid heat accumulation occurring over short times can lead to thermal shock of the work-piece, resulting in cracking or work-piece failure [133]. Additionally, heat accumulation that occurs over longer time scales can cause the work-piece to deform due to thermal expansion. If the temperature that the glass reaches during processing is close to its specific T_g, then network structure changes through bond relaxation and rearrangement can occur [118]. To avoid these physical or structural changes in the work-piece, the T_g of any candidate material should be above the maximum temperature reached during manufacturing, and the coefficient of thermal expansion should be kept as low as possible.

The intrinsic material property consideration becomes particularly important when working with ChGs as compared to traditional oxide glasses [129,131,132]. Given that the hardness values of oxide glasses, such as Schott's N-BK7 can reach up to 6 GPa, 2-4 times larger that typically reported for ChGs, it is expected that the resulting surface roughness

of chalcogenides will also be higher. This interrelationship has been experimentally verified on the shop floor as it much more difficult to achieve higher precision figure and finish on much softer ChGs. The glass transition temperatures, T_g, of chalcogenides can be as much as 200-350 °C lower than oxides. Similarly, the thermal expansion coefficient of ChGs is 2-5 times larger than the widely used N-BK7 from Schott Glass Inc. [89]. Although nearly all of the properties relevant to the optical manufacturing of ChGs are often deemed unfavorable compared to oxide counterparts, compositional tailoring of glass chemistry can be used to mitigate some of these property limitations. Efforts to minimize the unfavorable manufacturing aspects through compositional design should therefore focus on increasing the glass' hardness and glass transition temperature both which would yield a more thermo-mechanically robust material, and simultaneously decreasing the coefficient of thermal expansion. Achieving these results through glass composition and structure modification to the glass network will yield a material with improved manufacturability by producing a glass that is better suited for production with both SPDT and conventional grinding polishing methods.

For PGM applications the considerations of what makes a more *manufacturable* material are extremely different. In general a glass can be made into the negative shape of virtually any mold given the correct process parameters; viscosity, force, heating/cooling rates, etc. The factors for consideration of production through PGM of chalcogenide glasses are the temperature at which it must be molded, the glass' viscosity temperature relationship, and the maximum temperature at which the glass can be elevated to safely as to avoid volatilization. The temperature should be kept low to minimize production time, the

viscosity should change slowly with temperature, and the maximum upper use temperature should be kept sufficiently higher than the maximum temperature reached during the molding process.

During the PGM process, the glass material is a viscous material and thermal reflow will cause the surface roughness final molded optic to resemble the surface roughness of the mold, decreasing the importance for a glass to have a higher hardness. Additionally the thermal expansion of the material is not necessarily important as it can be predicted in computer simulations so that any shape changes due to expansion and/or contraction can be accounted for and "pre-designed" into the mold shapes [134,135].

3.4 Physical Property Characterization - Results

3.4.1 Density

The density of all the compositions along the three tielines was measured, and is presented in Figure 3.6 as a function of Se deficiency. There is an overall decrease in the density as the network becomes more Se deficient, and sharp transitions can be observed at the previously described locations where there is a shift in the types of available structures in the network. Namely, these transitions are present at either the location where the composition crosses stoichiometry, or at a higher level of Se deficiency where the GeSe ethane-like structures begin to appear. These transitions however, are not consistent across all tielines.

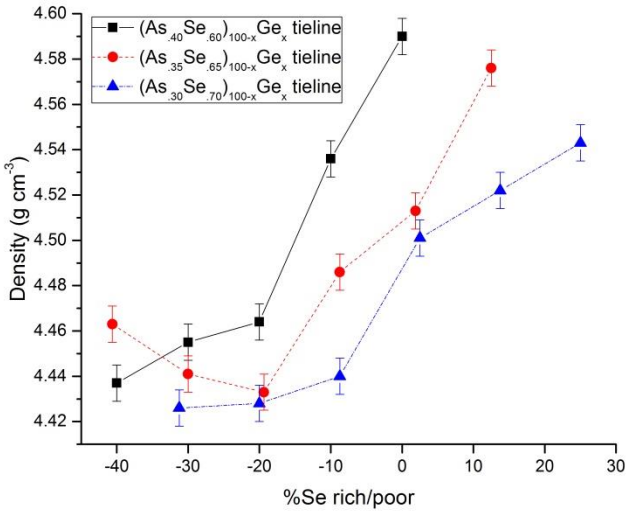

Figure 3.6 – Compositional variation of the density along the three tielines, as measured with the Archimedes Principle.

3.4.2 Hardness

The average hardness values for compositions along the three tielines are shown in Figure 3.7, and listed in Table 3.2. Across all three tielines, there is a clear trend of increasing hardness with MCN, highlighting that the increased network connectivity gained through Ge additions is resulting in a physically stronger network that is more resistant to plastic deformation [136].

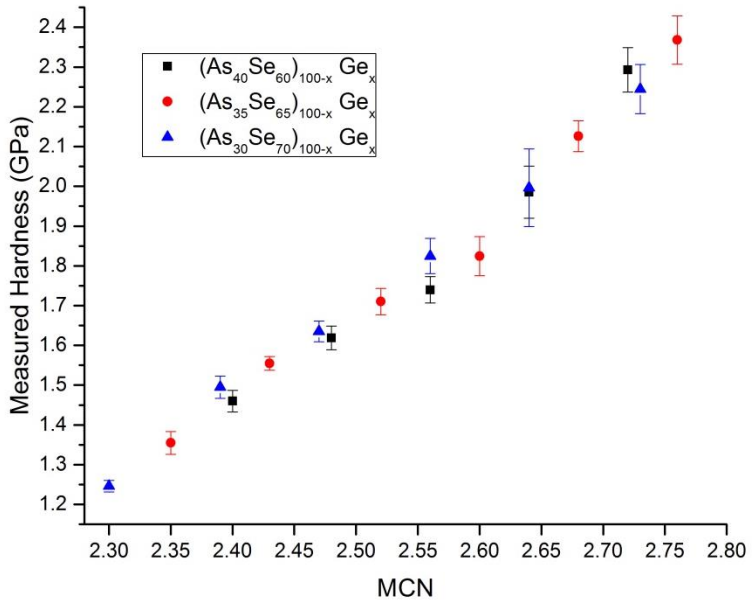

Figure 3.7 – Compositional variation of Vickers Hardness along the three tielines measured with and indentation load of 100mN

Mechanical properties such as the microhardness have a direct impact on crack initiation and fracture which accompany the mechanical processes in grinding. These processes are also impacted by chemical properties, which become more important during the polishing process. According to Fang et al. [137] and Lambropoulos et al. [129], there is a strong correlation between the post-production roughness for both bound and loose abrasive grinding, lapping, and polishing processes and the materials' mechanical properties as observed in their work on over 60 oxide glasses from both Schott Glass Inc. and Hoya Corp. In these studies, variations in mechanical properties directly affected removal rates, as well as how removal occurred and the residual sub-surface damage that remained as a result of fracture processes during grinding/polishing. As mentioned in Section 3.2, the final roughness of these polished oxide glass samples increases proportional to the inverse root of the hardness ($H^{-1/2}$) [129,131,132]. The relationship between the post-polish surface

roughness and the inverse root of the hardness of compositions along the $(As_{.35}Se_{.65})_{100-x}Ge_x$ tieline is shown in Figure 3.8. Similar to the oxide glasses investigated by Lambropoulos et al., there is a correlation between the polished roughness of the samples and the inverse root of the hardness.

Table 3.2 – Physical property values for all compositions investigated in this study.

Composition Sample ID	T_g (°C) (±2 °C) Heating Rate: 10 °C·min^{-1}	Upper Use Temperature (°C) (±2 °C) Heating Rate: 10 °C·min^{-1}	CTE (ppm/°C) (±1.0 ppm/°C) Heating Rate: 3 °C·min^{-1} Temp range: (50 °C – 0.8*T_g)	Hardness (GPa) (±0.09 GPa maximum) Indentation Force: 100 mN
40_60_0	191	437	22.1	1.46
40_60_5	215	447	21.1	1.62
40_60_10	239	517	21.6	1.74
40_60_15	274	533	19.1	1.99
40_60_20	318	541	16.0	2.29
35_65_0	159	432	25.6	1.36
35_65_5	199	470	20.4	1.56
35_65_10	235	514	20.8	1.71
35_65_15	267	532	19.0	1.82
35_65_20	306	559	16.2	2.13
35_65_25	350	543	14.1	2.37
30_70_0	134	435	28.8	1.25
30_70_5	168	466	25.0	1.50
30_70_10	225	500	20.5	1.64
30_70_15	263	548	19.0	1.83
30_70_20	299	557	17.4	1.99
30_70_25	344	548	14.8	2.25

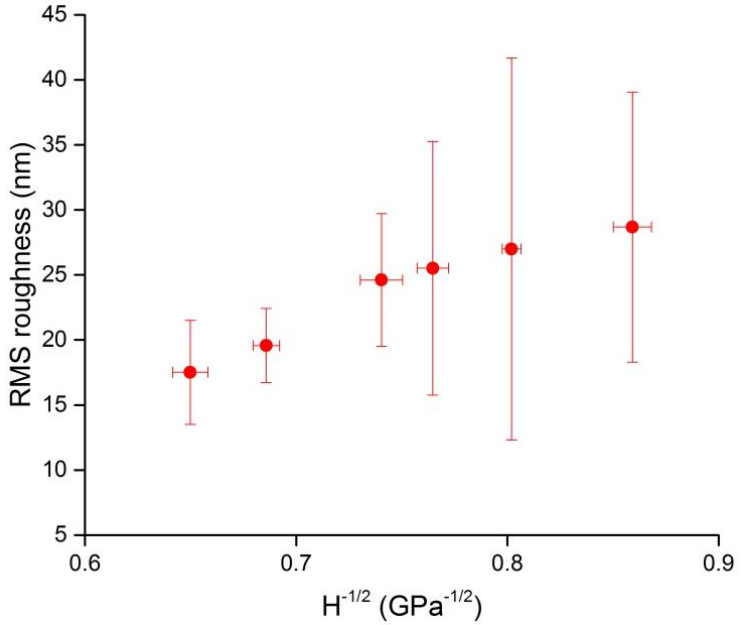

Figure 3.8 – Root-mean-square roughness in nm of $(As_{.35}\ Se_{.65})_{100-x}Ge_x$ tieline shown as a function of the inverse root of the Vickers hardness.

When looking at the effect of hardness on single point diamond turning (SPDT), there is a similar relation between final work-piece optical quality and the material hardness. According to Leung [138], there is a critical indentation depth for brittle materials that will lead to crack propagation. This critical indentation depth represents a transition from a ductile to a brittle material response, and is inversely related to the cube of the hardness of the material. This regime transition is measureable using a standard hardness tester, but can be related to the brittle-ductile modes in SPDT, where a lower surface roughness is created by operating in a ductile removal mode. Therefore, as the hardness of a material increases, the critical cutting depth necessary to stay within the ductile mode decreases, forcing lower removal rates and longer processing times. Leung also showed that lower cutting depths and lower feed rates result in a lower final surface roughness [138]. Therefore, as the hardness increases with added Ge, it should follow that lower cutting depths will be

required to maintain ductile material removal, but the decreased removal rates should lead to a lower final surface roughness.

3.4.3 Thermal Properties

Variations in the glass transition temperature for compositions along the three tielines are shown in Figure 3.9, and listed in Table 3.2. The entire data set was also fit with the modified Gibbs-DiMarzio equation, of the form:

$$T_g = \frac{T_0}{[1 - \beta(MCN - 2)]}$$

Equation 6

Where T_0 is the glass transition temperature of pure selenium (a fitting parameter here, not obtained from literature), β is a fitting parameter, and the MCN is calculated as previously described. The fitting of collected data resulted in a T_0 of 351.77 K, β of 0.575, and an r^2 value of 0.964. The Gibbs-DiMarzio equation is based on a model of increasing cross-linking of chains in a floppy network. While the assumption of increasing chain cross-linking is only valid for Se deficient compositions, the Gibbs-DiMarzio equation still provides a good prediction of the glass transition temperature regardless of Se content. Increasing the MCN through additions of Ge increases the glass transition temperature in the same manner as the hardness. The increased network connectivity raises the thermal energy required to rearrange bonds within the network in the same manner that it also makes the glass more resistant to plastic deformation.

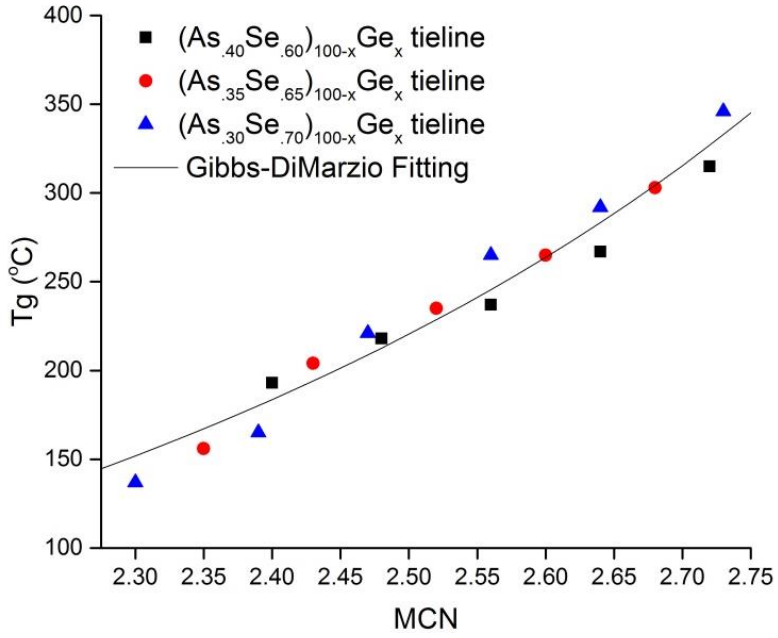

Figure 3.9 – Compositional variation of the glass transition temperature along the three tielines, measured at 10°C·min^{-1}. Errors are within the size of the data points.

The upper use temperatures for the investigated compositions were also measured and are shown in Figure 3.10, and listed in Table 3.2. Unlike the glass transition temperature and Vickers hardness, the upper use temperature did not increase monotonically with MCN. A maximum in upper use temperature was found in all three tielines at a Ge content of 20 at%. Under conventional fabrication, glasses should never reach temperatures near the glass transition temperature, let alone the absolute upper use temperature. However, during processes such as fiber drawing and compression molding, where the glass is heated above the T_g, caution must be used to avoid working where these glasses can volatilize and release carcinogenic by products. The maximum upper use temperature observed at 20 at% Ge suggests that there may a threshold in chemistry in this region of the ternary that lowers the thermal barrier for certain molecules to re-arrange. Theories as to which atoms or molecules are leaving the network can be confirmed with simultaneous thermal analysis –

mass spectrometry equipment, but remains an option for further studies in this ternary system.

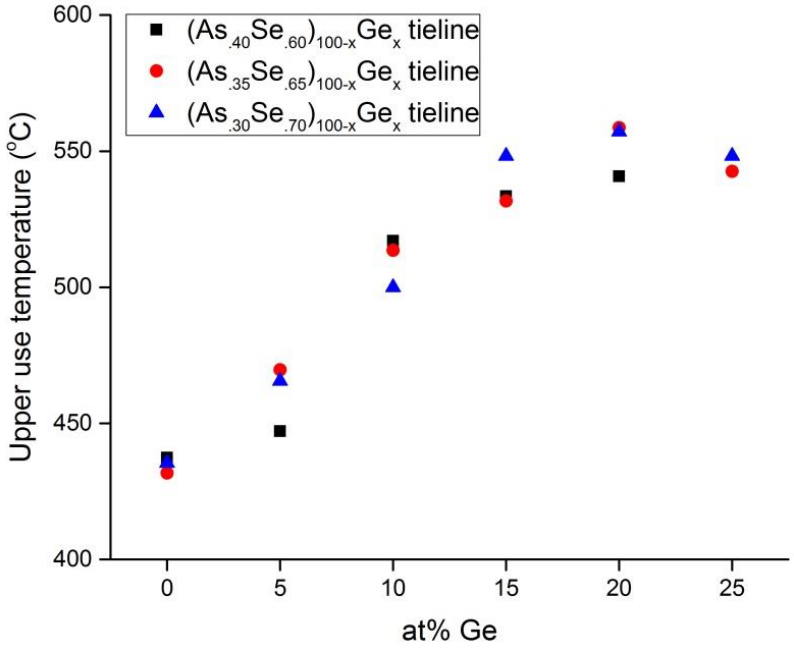

Figure 3.10 – Compositional variation of the upper use temperature along the three tielines, measured at 10°C•min^{-1}. Errors are within the size of the data points.

The coefficient of thermal expansion (CTE) was measured for each of the glasses along the three tielines, and is presented in Figure 3.11 and listed in Table 3.2. In contrast to the hardness and T_g, which both increased monotonically with MCN, the CTE was found to decrease monotonically with MCN. While the trend in CTE is quite the opposite as for the trends in T_g and Vickers hardness, the fundamental origin is the same. The increased network connectivity realized through Ge additions is holding the glass together more strongly and thus lowering the glass' response to thermal variations.

Shown in Figure 3.12 is a visualization of the effect of GeSe bonding on the properties along $(As_{0.35}Se_{0.65})_{100-x}Ge_x$ tieline. The figure simultaneously shows the relative contribution from GeSe bonds (as determined through Raman spectroscopy in Section 3.1) along with the hardness, CTE, and T_g.

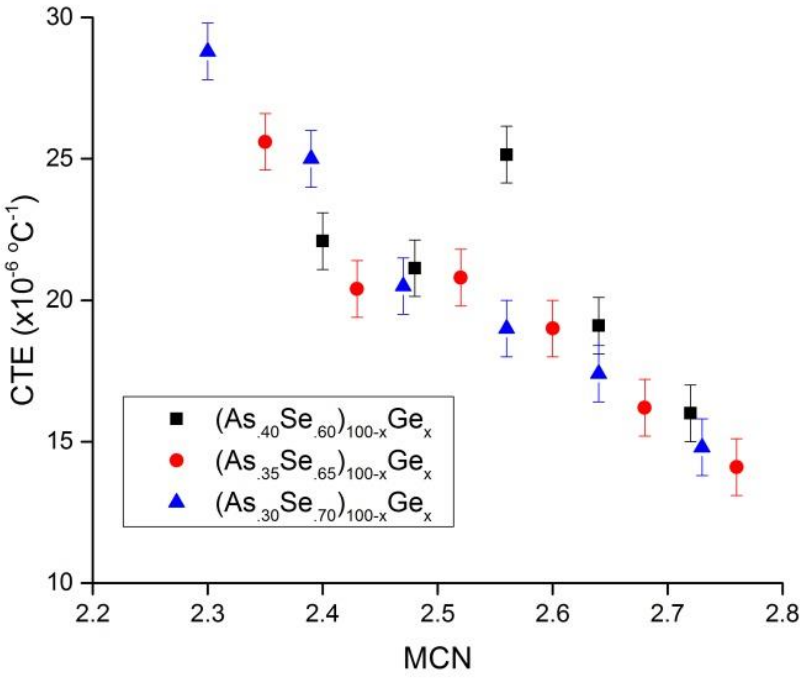

Figure 3.11 – Compositional variation of the coefficient of thermal expansion of along the three tielines, measured at a rate of 3°C·min^{-1} and between 50°C and 0.8 T_g.

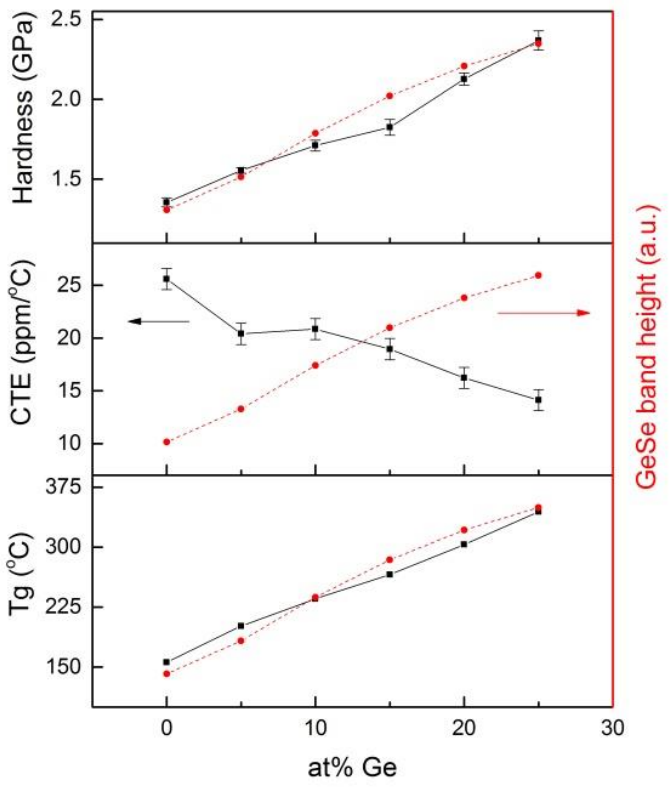

Figure 3.12 – The hardness, coefficient of thermal expansion, and glass transition temperature of the $(As_{0.35}Se_{0.65})_{100-x}Ge_x$ tieline, compared with the total relative GeSe band height.

3.5 Optical Property Characterization – Results

3.5.1 Transmission Cutoff wavelength ($\lambda_{c/o}$)

The IR transmission of all the compositions along the three tielines was measured and the calculated transmission cutoff wavelength ($\lambda_{c/o}$) is presented in Figure 3.6 as a function of Se deficiency. Please refer to Section 2.2.6 for specific information on the calculation of $\lambda_{c/o}$. From this figure, it should be immediately noticed that there are two significant transition points that occur as a function of the Se-rich/-poor %, and more importantly that

these two transitions occur at the same locations as previously described in Section 1.2.3 and as seen with the density in Section 3.4.1. In the case of the $\lambda_{c/o}$, there is no noticeable change in values for compositions with a Se-excessive network. As soon as the glassy network transitions from Se-excessive to Se-deficient, the $\lambda_{c/o}$ exhibits a strong blue-shift (shift toward shorter wavelengths). This trend continues until the compositions reach the level of Se-deficiency required to form the Ge-Se ethane-like modes. Here the $\lambda_{c/o}$ exhibits a minimum, and as the network becomes more Se-deficient the $\lambda_{c/o}$ experiences a redshift (shifts back toward longer wavelengths).

For applications focused on the MWIR, ~3 - 8μm, the changes in $\lambda_{c/o}$ will not alter the performance to any measureable degree. But as the spectral requirements for systems expand to include multiple bands such as NIR or SWIR, understanding the limitations of the optical material help in determining appropriate selection for the required application.

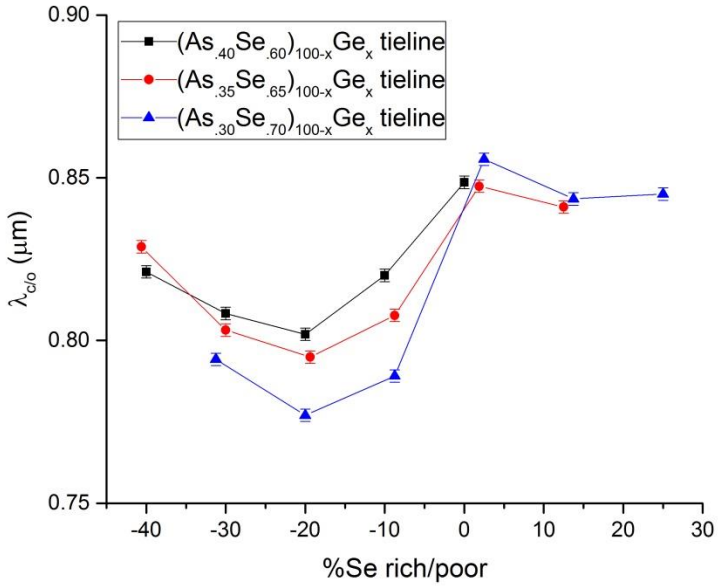

Figure 3.13 – Compositional variation in the transmission cutoff wavelength ($\lambda_{c/o}$), as a function of the Se-rich/-poor %.

3.6 Corroboration of Physical Properties with Prior Works

Numerous compositions within the GeAsSe ternary have been subject to investigation over the years, and as previously mentioned properties and trends such as T_g, CTE, hardness, and density have been thoroughly studied. An online database known as SciGlass has been established to compile the results on these, and countless other, glasses to assist researchers in their investigations. From the numerous references found on SciGlass, two specific papers with a compilation of properties within the GeAsSe ternary have been chosen to serve as references: "Some physical properties of GeAsSe infrared optical glasses" by Webber et al. [66], and "Glass Formation and Properties of Glasses in the As–Ge–Se System" from Aio et al. [139]. Additional references from Aio [140] and Voronova [45] have been used to fill the missing data regions as needed.

To that end, the SciGlass database was used to gather the Vickers Hardness, density, glass transition temperature, and coefficients of thermal expansion of all previously studied and reported AsSe binary and GeAsSe ternary compositions. Since the majority of the trends discussed in this chapter are best explained through variations on the MCN, the compilation of results obtained from SciGlass will be presented in a similar fashion. For consistency, glass values collected from SciGlass along the AsSe binary will be presented as hollow data points, values from the GeAsSe ternary as filled data points, and values measured as part of this investigation will be presented as red circles. Where possible error bars on the presently measured compositions is given, else it is within the size of the data point.

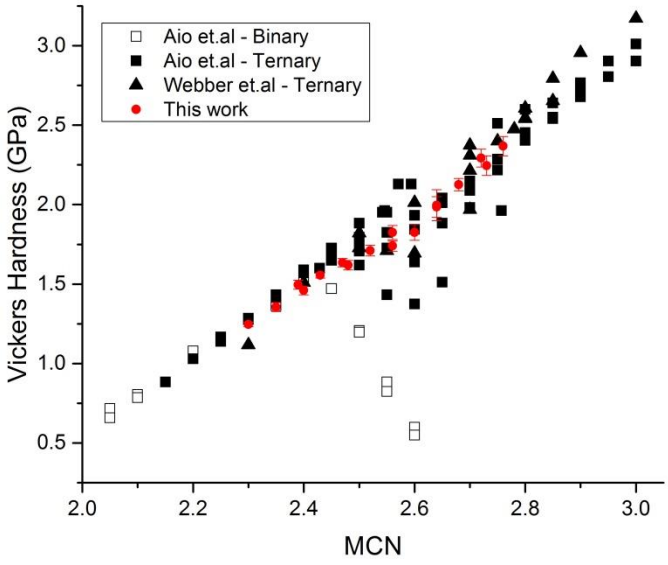

Figure 3.14 – Variations in Vickers hardness with mean coordination number, as collected from SciGlass and as measured here [66,139,140].

The Vickers hardness, density, glass transition temperature, and coefficient of thermal expansion SciGlass compilations are shown in Figure 3.14, Figure 3.15, Figure 3.16, and Figure 3.17 respectively, along with the values obtained in this investigation. All four of the properties exhibit either a minimum or a maximum along the binary at a MCN of 2.4, which is equal to the coordination number $As_{40}Se_{60}$ as predicted by Philips [67,68]. Along the ternary however, not one of these four properties exhibit a min/max in the ternary at a MCN of 2.4. The binary glasses fabricated in this experimental investigation had a maximum MCN of 2.4, and thus could not confirm or deny the existence of maxima or minima at that location. Additionally only the density shows the possibility of a broad minimum near a MCN of 2.67, but the significant variations in reported values is enough to raise suspicions of this conclusion. Measured values of all four properties show overall good agreement with the compiled SciGlass data, confirming that the glasses manufactured here fall within the norms of previously published non-optical data.

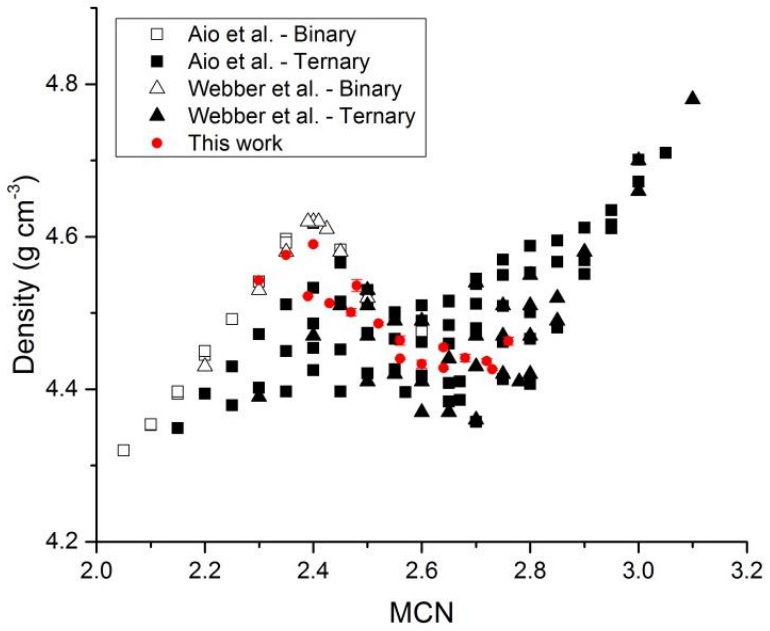

Figure 3.15 – Variations in density with mean coordination number, as collected from SciGlass and as measured here [66,139,140].

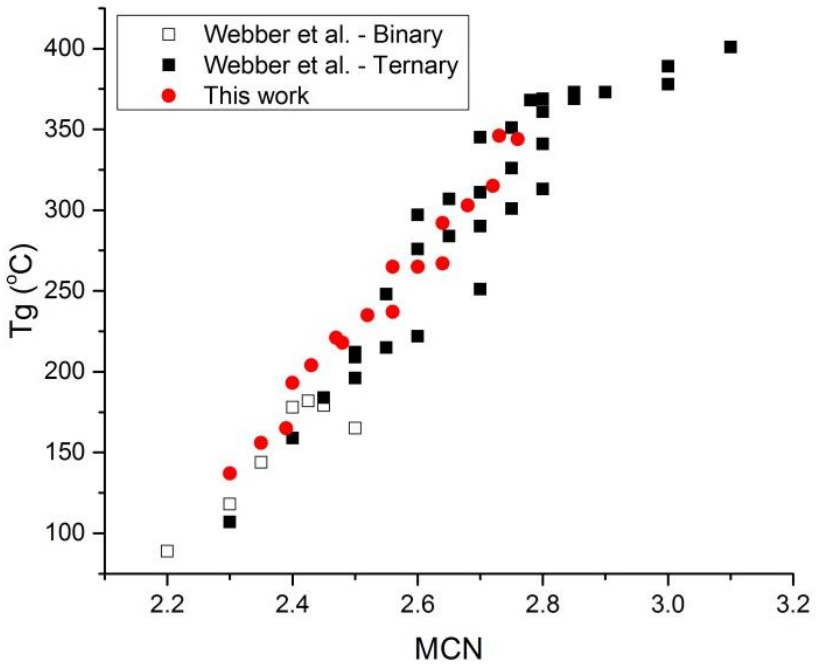

Figure 3.16 – Variations in glass transition temperature with mean coordination number, as collected from SciGlass and as measured here [66].

The entire CTE data set was fit with an exponential function of the form:

$$CTE = A + B * e^{(C*MCN)}$$

Equation 7

where A, B, and C are fitting parameters. The fitting of collected data yielded the following values for the fitting parameters: A of -9.91, B of 357.43, a C of -0.981 and an r^2 value of 0.902. This exponential fitting is also included in Figure 3.17.

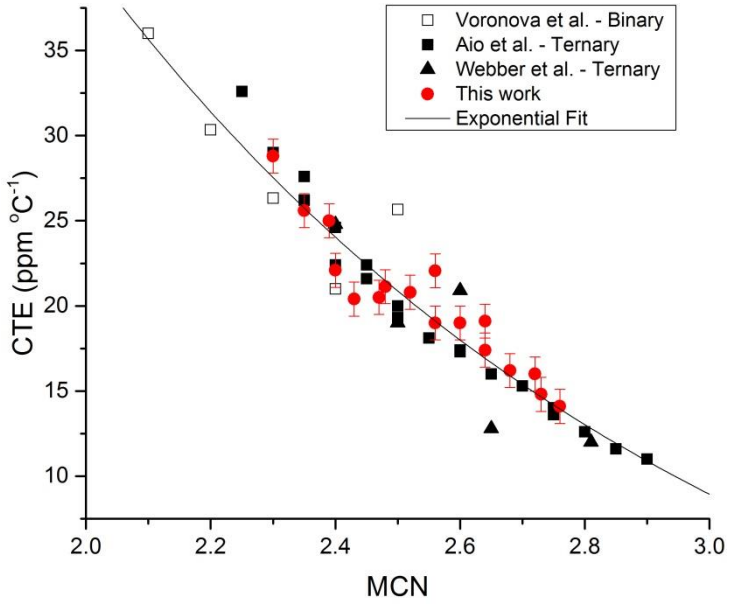

Figure 3.17 – Variations in coefficient of thermal expansion with mean coordination number, as collected from SciGlass and as measured here [45,66,139].

Similar efforts to compile the refractive index and thermo-optic coefficient of the GeAsSe glasses from SciGlass were also conducted. Of the previously investigated glasses, refractive index was found on a number of glasses, but nearly all were in the Se excessive region with much lower MCN values, and no thermo-optic coefficient data was found using SciGlass. Additionally, the experimental parameters of these investigations can vary in

both measurement wavelength and temperatures adding further ambiguity to external analysis. The lack of available data on this subset of leaves an opening for investigations on the index and its temperature derivative, as well as the fundamental origins of glass properties that dictate these property trends.

3.7 Conclusions

This chapter has presented the structural and material properties of the 17 GeAsSe glasses involved in this study. Structural analysis showed an increasing contribution of Ge-Se bonding, which serves to cross-link the puckered layers of AsSe and strengthen the network. The network strengthening effects of Ge additions were shown to be a driving force for increases in T_g and hardness, as well as decreases in CTE, all of which were shown to have a favorable impact on the manufacturing of chalcogenides on conventional fabrication techniques. The chapter has compared the results of the physical property measurements in this study to those seen in literature and shown good agreement between the two. Data presented in this chapter will be referenced to in the following chapters, as required for relevant analysis of optical properties.

Chapter 4

Refractive Index Metrology

This chapter discusses the decision to utilize the prism coupling method to characterize the refractive index and dn/dT, along with its fundamental theories and relative strengths and weaknesses. The necessary modifications to convert an "off the shelf" Metricon Prism Coupler to one that is fully capable of measuring refractive index and thermo-optic coefficient (dn/dT) in the infrared will also be presented. Modifications, construction, and calibration performed on two separate systems will be discussed. A detailed analysis of the error on the index and dn/dT will be presented, highlighting areas for improvement that will potentially decrease the error in one of both of these properties.

Measurements of the refractive index and dn/dT for the GeAsSe glasses outlined in Chapter 1 will be presented from Metricon systems located at both Pacific Northwest National Laboratory (PNNL) and University of Central Florida (UCF), along with an analysis of the "cross-calibration" between the two systems. Repeatability studies will also be presented to highlight the ability of the system to produce consistent data, and homogeneity data will be presented to highlight the ability of the material to do the same. The index and dn/dT of selected compositions will also be investigated in larger melt form, to assess their candidacy for potential commercial scale up.

Ultimately, the trends in the index and dn/dT within the GeAsSe ternary will be analyzed in terms of the network coordination and the level of Se excess or deficiency (relative to stoichiometry), and the merits of each will be discussed. The index and dn/dT will be

further analyzed using established models for predicting property values, based on other physically measureable properties, such as those outlined in Chapter 2.

4.1 Development and Construction of Infrared Prism Coupler

As part of a collaborative project with Clemson University (prior to relocation to University of Central Florida), Pacific Northwest National Laboratories (PNNL), and Edmund Optics, a prism coupler was purchased from Metricon Corporation (model 2010M) for the purpose of measuring infrared refractive index and thermo-optic coefficient (dn/dT). The normal operation of the Metricon system only measures index at 632.8nm with a visible HeNe laser, and can be extended into the near infrared (NIR) without changing sources, detectors or prism material. In order to gain the ability to measure materials in the infrared, several modifications were implemented. The following sections describe, in detail, the initial modifications made to the 2010M Metricon system at PNNL, as well as modifications that were made to a second 2010M Metricon system in the labs at University of Central Florida (UCF). The system at University of Central Florida was setup to be able to reproduce the infrared index measurement capabilities at PNNL, as well as reproduce the results obtained at PNNL.

One immediately necessary modification for IR measurements is a change of material for the measurement prism, and detector type, as well as a change of illumination source. The standard oxide prism material (rutile) transmits into the infrared, but the refractive index (~2.0) is far too low to measure chalcogenide glasses which with compositional variation can have indices as high as 3.4. Additionally, the standard Si detector has greatly

diminished responsivity beyond 1100 nm. Metricon Corporation offers several optional materials that transmit into the IR and allow for measurements of infrared materials. The available prism materials include Ge, Si, Rutile, and GaP. A Ge prism was chosen as the primary prism material for infrared measurements. The decision was based on the refractive index of the material, which determines the range of measurable sample index, as well as the material's transmission window. Several detectors are available for infrared applications, and a liquid nitrogen cooled Mercury-Cadmium-Tellurium (MCT) detector was ultimately chosen for the system upgrades. Laser sources for infrared applications include quantum cascade lasers (QCLs) which can be manufactured to give several unique output wavelengths, optical parametric oscillators (OPOs) which offer tunability windows, as well as gas lasers such as HeNe, operating at 3.4μm and CO_2, offering several excitation wavelengths between 9.2 and 10.9μm.

4.2 Modifications to the system at PNNL

The standard layout for the Metricon 2010M system is shown in cartoon form in Figure 4.1. The first step in the modifications was to determine a way to combine the external infrared (IR) and the on-board visible HeNe beam into one collinear beam path. It is necessary to combine these to beams for two reasons. First general system alignment after the beams are collinear is much easier with light sources that are visible to the naked eye. Second, the system needs a visible light source for a self-referencing calibration that is performed with every measurement. It was determined that a wafer or thin window of Ge would act as a window for IR sources, while acting as a mirror for the visible HeNe laser source. A Ge window was added to the beam path, and the on-board HeNe source was

moved to the opposite side of the system to allow for beam combination. Both Figure 4.2 and Figure 4.3 show the modified layout of the system with the Ge window and new placement of the HeNe laser. With these two modifications, and careful beam alignment, the HeNe beam and any external IR beam will hit the measurement prism at the same position and angle.

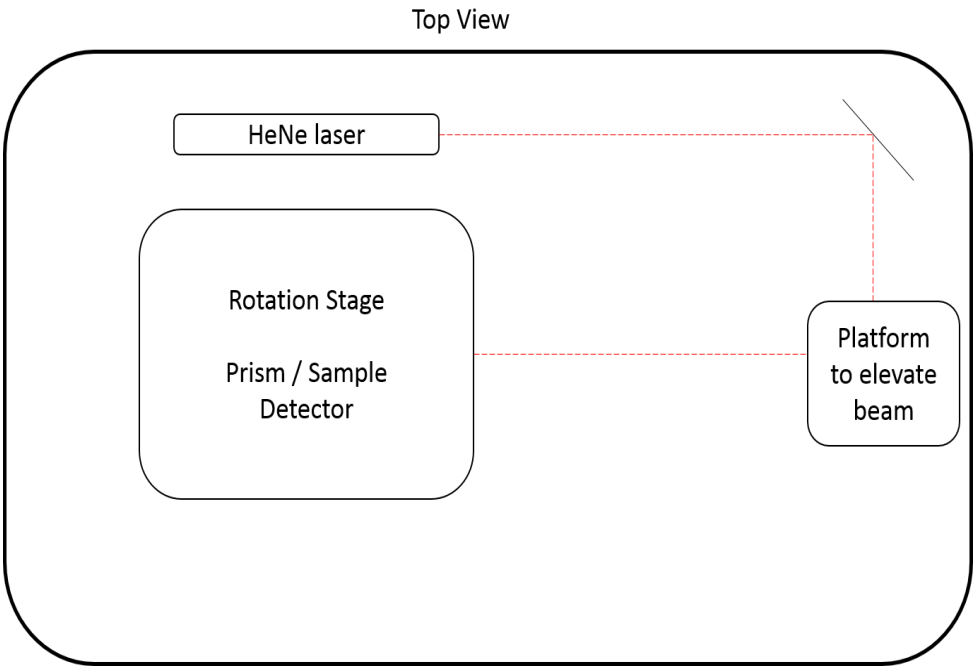

Figure 4.1 – Top view of Metricon 2010M system, as received.

The normal Si line detector for visible measurements is small and can be mounted directly on the rotation platform. When switching to an MCT detector for IR measurements, *two* modifications are necessary. First, since MCT detectors are not available as line detectors (or are extremely cost prohibitive), an infrared integrating sphere is needed to ensure that exiting light from the prism will reach the detector regardless of the exit angle. Second,

because of size of both the integrating sphere and MCT detector, an extra platform was needed to hold both the items. A close up of the layout of the prism, sample, and detector for both the visible and IR setups are shown in Figure 4.4. Additionally, a picture of the Metricon System (at UCF) is shown in Figure 4.5.

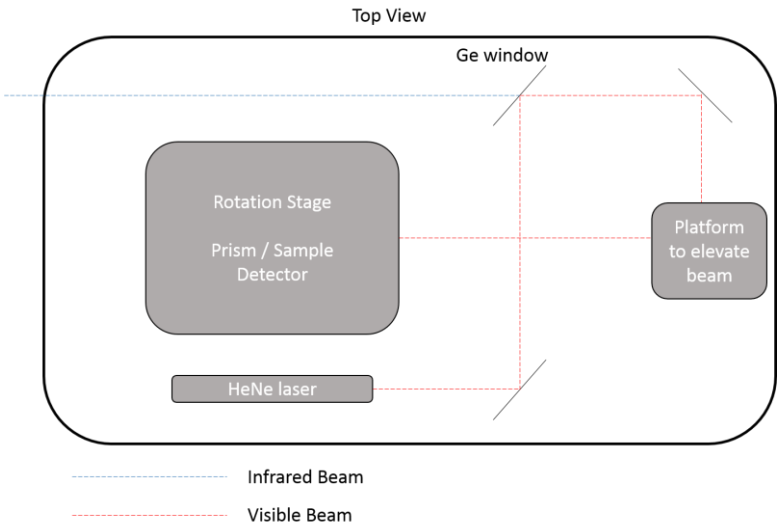

Figure 4.2 – Top view of Metricon 2010M system, after modifications.

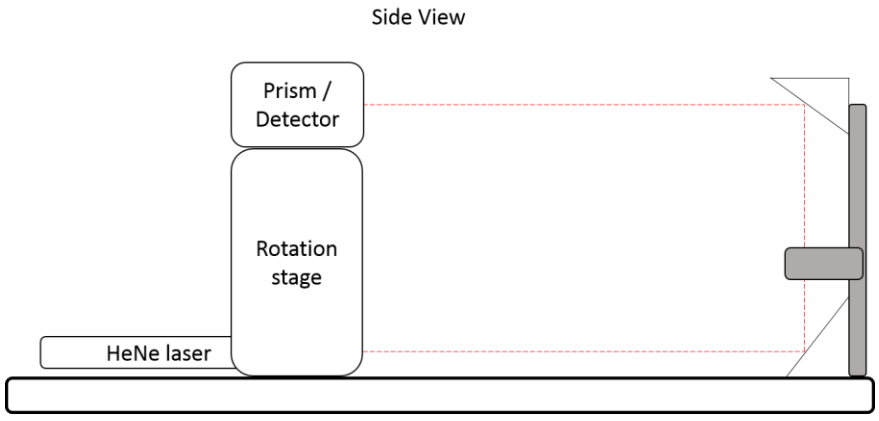

Figure 4.3 – Side view of Metricon 2010M after modification

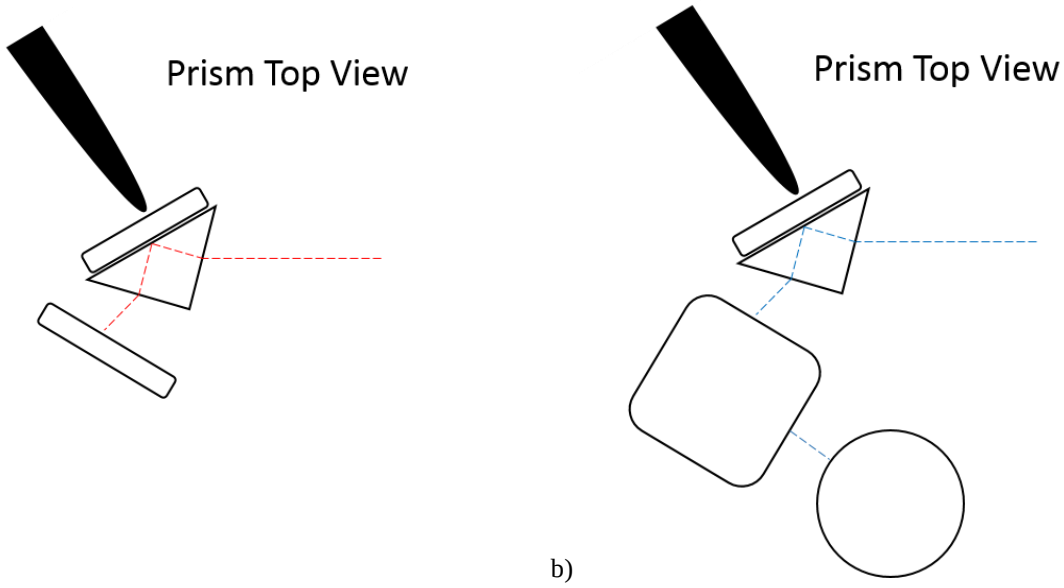

Figure 4.4 – Close up of the prism, sample, and detecting optics, for a) the "stock" Metricon 2010M and b) after the necessary modifications for operation in the infrared.

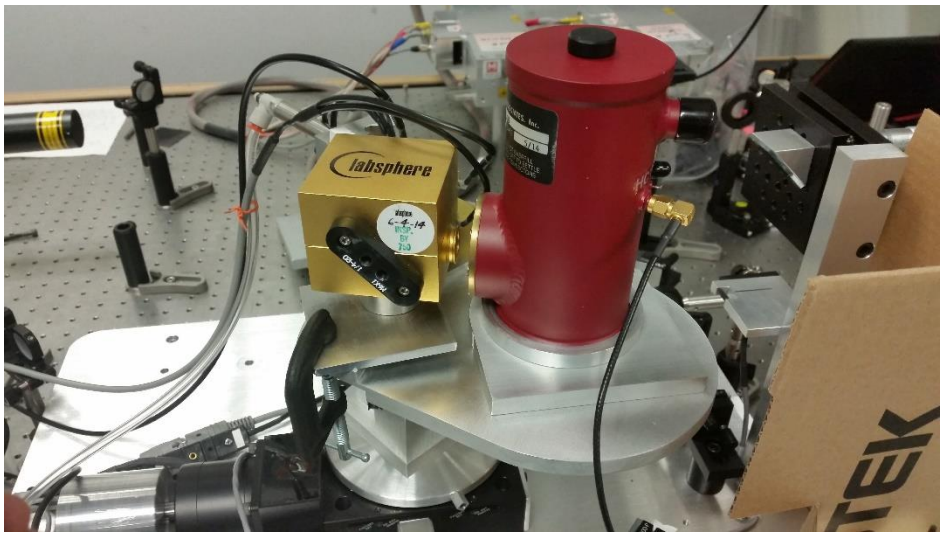

Figure 4.5 – Metricon System (UCF) after modifications to allow for IR measurements.

All external sources are laid out on an optical table to have semi-unique beam paths. That is, they have a unique beam path up until one common mirror, after which they share a similar beam path (but are not necessarily guaranteed to be collinear) with each other. When switching between IR sources, it is important to check alignment with the on-board HeNe source. Two adjustable mirrors are required for each source to grant both angular and positional freedom for alignment with the HeNe source. Figure 4.6 shows an approximate setup of the optical table used for the PNNL Metricon system, with a simplified schematic of the Metricon system [141]. Because of the noise associated with MCT detectors and IR measurements, a lock-in amplifier is necessary to improve the signal quality. An optical chopper operating at 1.5 kHz was added to the IR beam path before entering the Metricon and combining with the HeNe.

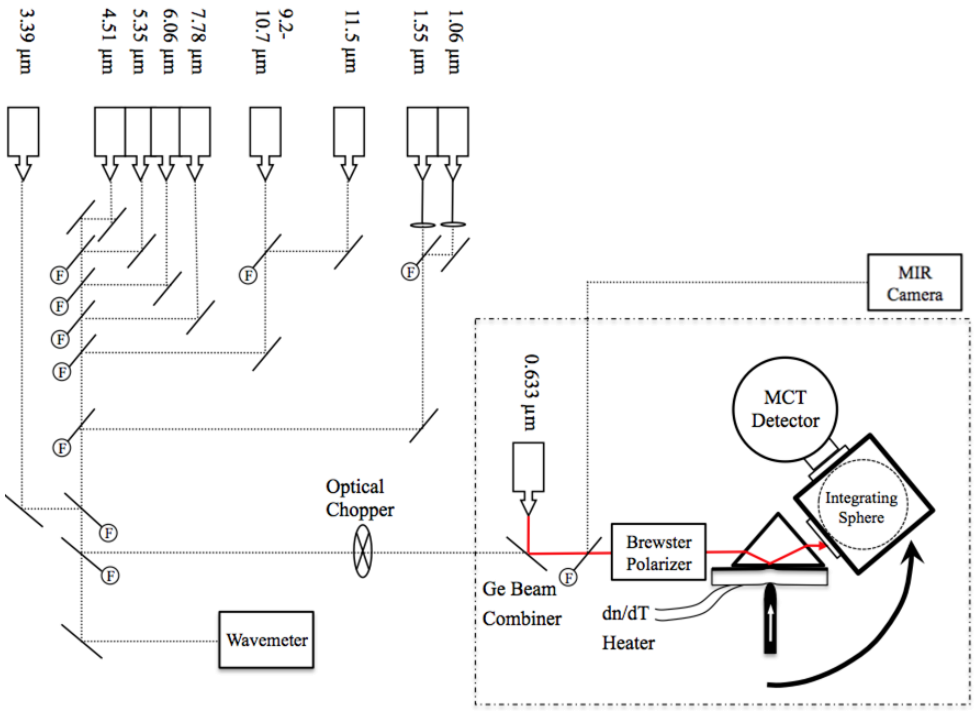

Figure 4.6 – Schematic of optical table layout at PNNL, obtained from [141].

4.2.1 Modifications to system at UCF

The Metricon 2010M system at University of Central Florida (UCF) also underwent modifications to allow for IR index and dn/dT measurements. The modifications were intended to duplicate the system at PNNL, but not to mirror the exact design and functionality. The steps necessary for the modification of the PNNL Metricon system are the same for the UCF system: prism and detectors need to be switched out, external IR beams need to be aligned with the on-board HeNe through a Ge window, IR signal needs to be process through a lock-in amplifier, and a mount needs to be designed and manufactured to support the additional IR optics "behind" the prism. The UCF Metricon system differs from the PNNL Metricon system in the layout of the optical table, design of the platform supporting the optics, as well as the actual IR sources/wavelengths used for measurements.

The UCF system uses three IR prisms: Ge for standard IR measurements, Si for high index measurements, and GaP for lower index measurements. The measureable index range for each of the three prisms is listed in Table 4.1. Two optical parametric oscillators (OPOs) were purchased from M^2 Lasers (Firefly-IR) to serve as the mid-IR sources for measurements. The OPOs offer tunable wavelength selection in the ranging from approximately 1500nm to 4800 nm. The specific wavelengths of tunability for each output of the OPOs are shown in Table 4.2. The Ge window used to combine the IR and visible beams was purchased from Edmund Optics and is held at a 45° angle with respect to the propagation direction of both the IR and visible beams (as shown in Figure 4.2). The

integrating sphere (Lab Sphere 3P-LPM-020-IG) and detector (IR Associates MCT-13-1.00) provide the same functionality as the versions in the PNNL system.

The OPOs from M^2 Lasers are pulsed lasers with a repetition rate of 150 kHz, which eliminates the need for optical chopping of the beam. The repetition rate of the laser was modified to 112 kHz with a signal generator (GwINSTEK SFG-1013) so that it could be amplified by a Princeton Applied Instruments lock-in amplifier (model 5209), which can only amplify signals up to a maximum repetition rate of 115 kHz. The signal generator was operating in square wave mode, and served as the external trigger for both the M^2 lasers as well as for the lock-in amplifier.

Table 4.1 – Approximate measureable index and wavelength ranges for the IR prisms

Prism material	GaP	Ge	Si
Approximate Index Range	2.0-2.6	2.3-2.9	2.8-3.4

Table 4.2 – Available sources for UCF Metricon system

	Wavelength range (μm)
Firefly 1 - Signal	1.48 – 1.88
Firefly 1 - Idler	2.4 – 3.8
Firefly 2 - Idler	3.2 – 4.6

4.3 Measurement Protocol

This section aims to provide a description of the measurement process employed when using the Metricon system, specifically while operating in the infrared.

Firstly appropriate sample specifications need to be established. For bulk materials, the sample needs to meet the following criteria: at least one polished, flat optical surface, with a lower hardness than the measurement prism, thickness between 2mm and 3mm, and a

refractive index within the measurement prism's measurable index range. If the sample is harder than the prism, the thickness is too large, or the sample is unpolished there will be weak or no optical contact between the sample and the prism. Having two polished sides does not necessarily increase the quality of the measurement, and in certain cases (thin samples relative to measurement wavelength) can actually exhibit interference fringes and degrade the measurement quality. The ideal sample size for chalcogenide glasses would be as follows: 10-25 mm diameter disks (or 10-25 mm long square) measuring 2-3 mm in thickness, parallelism within 100 arcmin, and a surface roughness less than 50 nm RMS on both sides.

The first step in measurement is to turn on the infrared (IR) source and give it time to warm-up and reach steady state operation. Depending on the laser in use this can take between 5 minutes and 1 hour. The on-board HeNe laser should also be turned on at this time. While the laser is approaching steady state, the alignment and beam profile of the IR source should be monitored. During this warm-up time the system can be prepared for measurement, and the Mercury-Cadmium-Tellurium (MCT) detector should be filled with liquid nitrogen.

Both the sample and prism faces should be cleaned with acetone or another organic solvent. While both the sample and measurement prism are at room temperature, the sample is held flat against the rear face of the measurement prism with a pair of wafer tweezers. A pneumatic actuator is switched on, and holds the sample against the prism while also creating a spot of optical contact between the two surfaces. Next, the temperature is set using two Omega temperature controllers (CL3515R) to the adjusted temperature set point (described later). After equilibrating for 15-30 minutes, the refractive index of this a strip

of IR thermal paper and an additional mirror are needed. Directly after the Ge window, place the IR thermal paper in the beam path. The visible HeNe spot should be immediately visible, and the IR beam should change to color of the thermal paper to indicate its location. Adjust one mirror so that the two beams overlap, this only ensures that the beams are aligned at on position in space. To ensure the two beams are aligned at all points after the Ge wafer, a second alignment position is needed. Place a mirror in the beam path of the IR/visible beams and direct to a far side of the room. Again place the thermal paper in the beam path (as far away as possible), and observe the location of the two beams. Adjust a second mirror so that the two beams again over lap at this second position. This process will need to be repeated several time, alternating near and far positions, to ensure the two beams are collinear at all points along the propagation axis. When the two beams are closely aligned using the thermal paper, a quadrant detector should be used to obtain numerical data on the alignment. A quadrant detector from Ophir Photonics (3A-Quad) was used for the alignment of the UCF system and the alignment between the visible and IR lasers was found to be better than 0.2 mrad. Analysis from Carlie et al. showed that a ±0.4 mrad angular error produces a ±0.0004 absolute error on the index [142].

Once the two beams are properly aligned, the thermal paper and extra mirrors should be removed from the beam path. Using the HeNe beam as a visual guide, the two beams should be directed to the upper corner of the measurement prism. The system is designed so that the optical contact between the sample and the prism should occur in this location, but additional work may be needed to find the precise location of the coupling spot. The integrating sphere and detector should be positioned to give a stable signal near where the

"knee" of the index measurement is expected to occur. Both the integrating sphere and detector will need to be adjusted to achieve a flat, stable signal, and to produce a sharp knee for index measurements. The visual output of the software is shown in Figure 4.7.

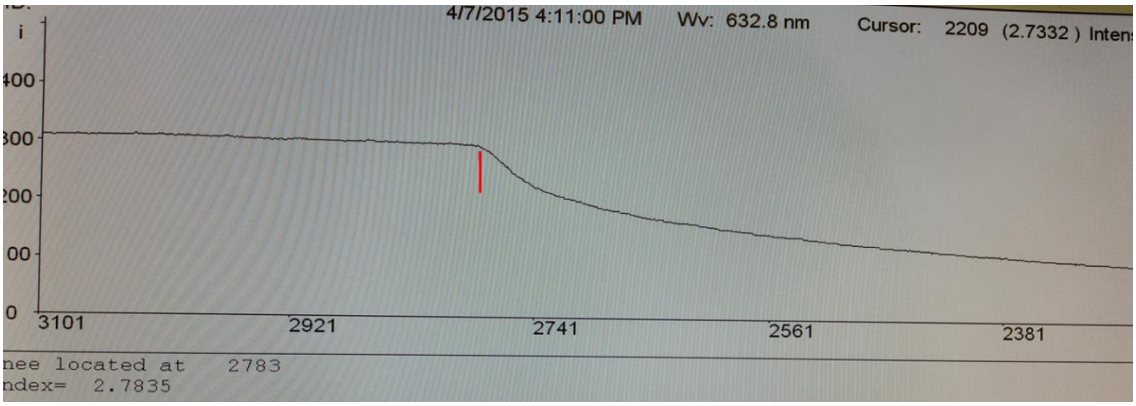

Figure 4.7 – Visual output of the Metricon software. The "knee" is indicated by the redline in the graph, and is used to calculate the refractive index.

The glass samples should be measured at the following temperature intervals to obtain sufficient data for dn/dT fitting: 30 °C, 50 °C, 70 °C, and 90 °C. Most glasses exhibit a linear change in refractive index with temperature, and can be measured in ascending temperature intervals (30 °C first). However, as will be described in much further detail in Chapter 5, certain glasses exhibit a level of "room temperature relaxation" of the refractive index, and should be measured at temperature set points in descending order (90 °C first).

This issue is extremely important in trying to quantify variations in properties with temperature (such as dn/dT measurements) or in attempting to quantify index changes following deviation from the as-annealed starting point (such as what is observed as an 'index-drop' during precision glass molding where samples see thermal excursions beyond T_g). In these instances, the room temperature, 'as-quenched/annealed free volume and

density' has been changed and this network modification results in measurable changes to a range of physical properties, including optical properties. This is discussed in greater detail in Chapter 5.

4.4 Calibration

A general standard operating procedure (S.O.P.) for measuring the refractive index on the modified IR Metricon system used in this study can be found in **Appendix A** and may be useful for new users. The following section will describe the specific steps taken to calibrate and characterize a Metricon prism coupler.

4.4.1 Thermal

As part of the Metricon system design, both the pneumatic actuator and thermal clamp for the measurement prism have thermocouples embedded in their structure. The location of these thermocouples is close enough to control the temperature, but not close enough to precisely know the temperature at the point of measurement (i.e., where the laser beam hits the specimen). For the thermal calibration of the PNNL system, a thermistor (Omega 44006) was epoxied to a small copper wafer with thermally conductive paste. The copper wafer and thermistor were held in place as a sample would be, with the thermistor head being as close to the measurement position as possible. The resistance of the thermistor was recorded and compared to the manufacturer's data sheet to obtain an accurate temperature. For the thermal calibration of the UCF system, a thermocouple (Omega SC-TT-K-30-36-PP) was used in a similar fashion.

Table 4.3 – Temperature set point and temperature at measurement location

Temperature Set point (°C)	Temperature at Measurement location PNNL System (°C) ±0.3 °C	Temperature at Measurement location UCF System (°C) ±0.3 °C
20	25.1	25.0
30	29.6	29.9
35	33.8	34.8
40	38.3	39.5
50	46.9	49.1
60	55.5	58.9
70	64.4	68.5
80	72.9	78.1
90	81.0	87.7
100	90.0	97.5

The temperature set point was then increased to 100 °C in 5-10 °C intervals, starting at 25 °C to obtain an offset curve between the temperature set point and the temperature at the measurement position. The system was allowed to thermally equilibrate for 30 minutes before measuring the average temperature and the variation around the average. It was determined that the maximum variation in temperature was 0.3 °C for the PNNL system and 0.3 °C for the UCF system.

Table 4.3 and Figure 4.8 show the temperature set points used, and the resulting temperature at the measurement location. The desired temperatures at the measurement location are 30, 50, 70, and 90 °C. Table 4.4 lists the required set points to obtain these specific temperatures for both systems. This process should be repeated for each individual prism to account for prism material differences or variations in the location of thermocouples or heaters with respect to the mounted prism.

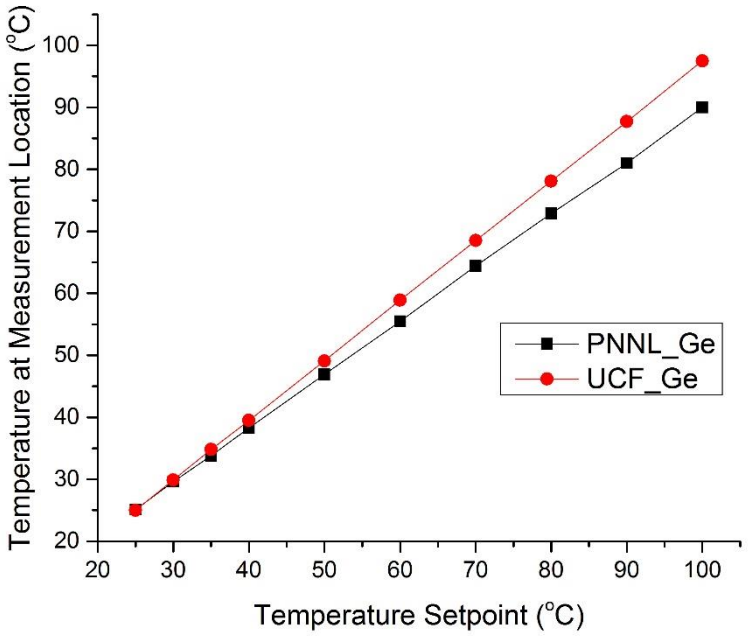

Figure 4.8 – Thermal offset curve for PNNL_Ge prism (black squares) and the UCF_Ge prism (red circles)

Table 4.4 – Required temperature set points for desired measurement temperatures

Measurement Temperature (°C)	30	50	70	90
Required temperature Set point - PNNL (°C)	30.5	53.7	76.8	100
Required temperature Set point - UCF (°C)	30.2	51.0	71.6	92.3

4.4.2 Refractive index (PNNL System)

To start with the calibration, PNNL purchased a small boule of ZnSe (Crystaltechno Ltd.). From this boule, a minimum deviation prism was fabricated and sent to M3 Measurement Solutions Inc. (M3MSI) for minimum deviation refractometry. From the same boule, 10 disks measuring 15 mm x 1 mm were also fabricated. These disks were assumed to have the same index as the minimum deviation prism as additional unpublished work at PNNL showed top-to-bottom variation and center-to-edge index variation of ZnSe boules to be

within the error of the measurement technique (<.0005 RIU) [143]. The data provided by M3MSI contains a Sellemeier fitting of the ZnSe at 20 °C as well as the measured dn/dT of several wavelengths, fit between 0 °C and 70 °C. The reported error on the ZnSe refractive index is ±0.0001 refractive index units (RIU).

Using an approximate prism index (one or no decimal points) and the method as described previously, the refractive index of the ZnSe sample was measured. The prism index was adjusted so that the measured ZnSe index matched the data provided by M3MSI for that specific wavelength and temperature combination. The process of measuring the refractive index and adjusting prism index to have the results match the calibration data is repeated a minimum of 20 times. The reported refractive index for this specific wavelength and temperature combination is reported as the average of these points.

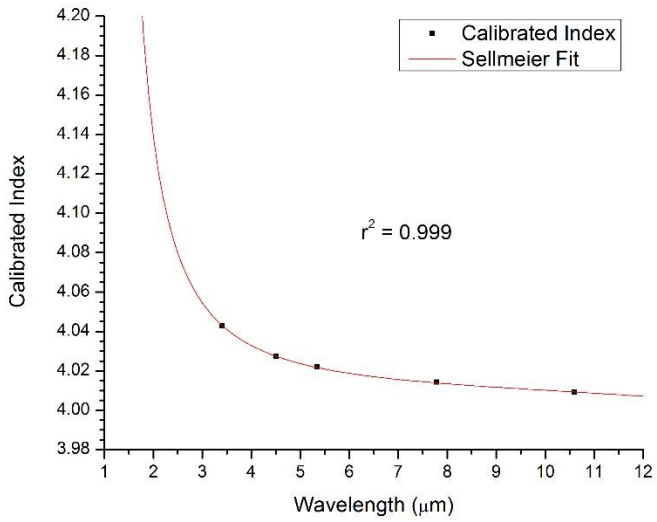

Figure 4.9 – Calibrated index of PNNL Ge prism at 30 °C

The refractive index for each prism is calculated at 30, 50, 70, and 90 °C for each necessary wavelength. Moving forward, this will be referred to as the calibrated prism index. The calibrated prism index at 30 °C for the PNNL Ge prism is shown in Figure 4.9. The data was fit with a standard Sellmeier equation of the form:

$$n^2 = A + \frac{B\lambda^2}{(\lambda^2 - C^2)} + \frac{D\lambda^2}{(\lambda^2 - E^2)}$$

Equation 8

where A, B, C, D, and E are all fitting parameters. The calibrated PNNL Ge prism index for all temperatures along with their respective Sellmeier fittings is shown in Figure 4.10 and listed in

Table 4.5. The Sellmeier coefficients and individual r^2 values for each fit is shown in Table 4.6.

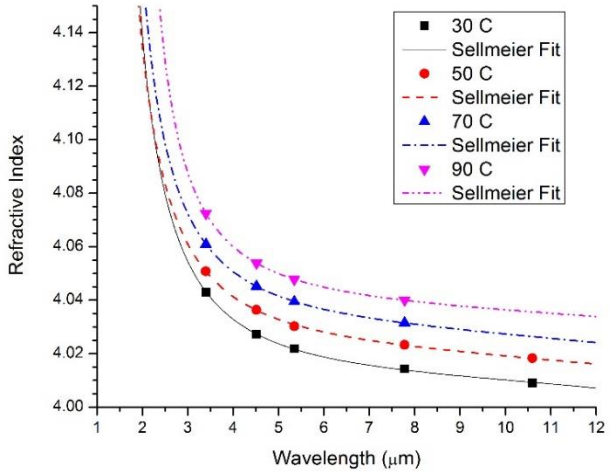

Figure 4.10 – Calibrated Index of PNNL Ge prism at all measured temperatures

Table 4.5 – Tabulated refractive index of PNNL Ge prism. Error on these measurements is ±0.0005

Wavelength (μm)	30 °C	50 °C	70 °C	90 °C
3.4	4.0430	4.0508	4.0609	4.0724

4.515	4.0273	4.0364	4.0452	4.0539
5.348	4.0219	4.0303	4.0395	4.0478
7.778	4.0143	4.0233	4.0315	4.0400
10.591	4.0091	4.0183	-	-

Table 4.6 – Sellmeier coefficients and calculated r^2 fitting values for Sellmeier fits

Temperature (°C)	A	B	C	D	E	r^2
30	14.08	2.0	1.17	0.10	22.31	0.999
50	14.10	1.99	1.13	2.00	73.66	0.999
70	14.65	1.58	1.29	2.00	72.50	0.999
90	15.42	0.88	1.70	2.00	85.92	0.999

The refractive index can also be presented as it changes with temperature. Presented in Figure 4.11 is the change in index with temperature for all the measured wavelengths. There was an issue with the 10.591µm source at PNNL to prevented further measurements after the 30 °C and 50 °C data points were collected. When the data is plotted in this form, the materials dn/dT can be calculated as the slope of a linear best-fit line. Table 4.7 lists the dn/dT (slope) of each wavelength along with the calculated r^2 values for those fits. Note that the r^2 for the 10.591µm source was not calculated as there were only 2 data points. The values listed in Table 4.7 compare well with dn/dT values for single crystal Ge found elsewhere in the literature [5,8].

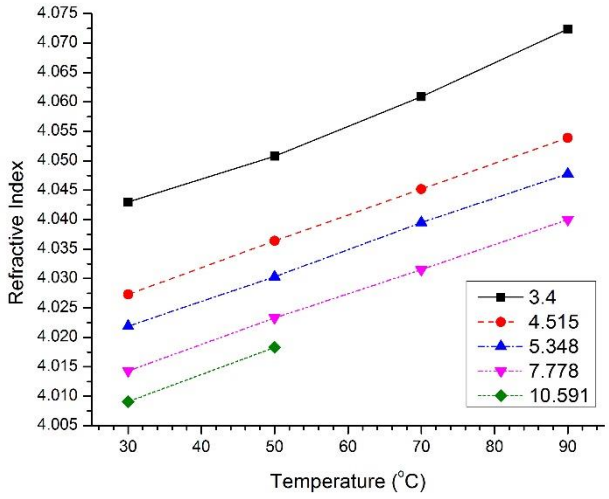

Figure 4.11 – PNNL_Ge prism index as a function of temperature for several wavelengths

Table 4.7 – Calculated dn/dT of Ge and r^2 values from linear fits

Wavelength (µm)	dn/dT ±11.2 ppm/°C	r^2 of linear fit
3.4	491.5	.996
4.515	443.0	.999
5.348	434.5	.999
7.778	426.5	.999
10.591	460.0	N/A

4.4.3 Refractive index (UCF System)

Initially for the UCF prism coupling system, only one wavelength (4.515 µm) was available for refractive index and thermo-optic coefficient measurements. This limits the ability to determine the dispersion of both the Ge measurement prism and any samples. The Ge prism for the UCF system, which will be referred to as UCF_Ge, was calibrated using the same general protocol as for the system at PNNL as well as the same ZnSe calibration wafers, initially measured by M3MSI. The calibrated index for the UCF_Ge

prism at 4.515 µm and various temperatures is shown in Figure 4.12, along with the calibrated index for the PNNL_Ge prism at 4.515 µm as well. The calibrated index for the two prisms correlates extremely well, and there is only a small offset between the two (approximately 0.0030 RIU), with the measured dn/dT also correlating well: 443 ±11.2 ppm·°C^{-1} for the PNNL_Ge and 445 ±11.2 ppm·°C^{-1}for the UCF_Ge prism.

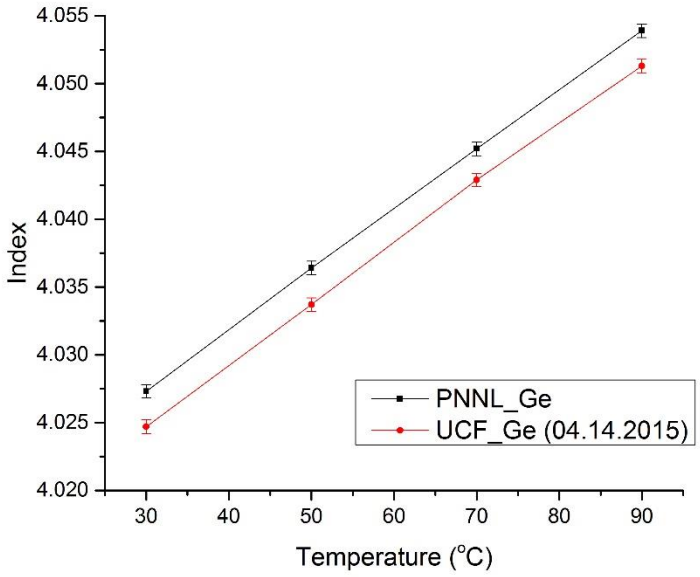

Figure 4.12 – Calibrated refractive index of the PNNL_Ge prism (black squares) and UCF_Ge prism (red circles) at 4.515µm for the four temperature set points.

4.5 Error analysis

4.5.1 Sources of Error (Absolute Error)

The absolute error for index and dn/dT measurements obtained by a prism coupler is calculated by the equation first presented by Zhou et al. [144]:

$$\Delta\frac{dn}{dT} = \pm\left[\frac{2}{(T_2 - T_1)^2}\Delta n^2 + \frac{2(n_2 - n_1)^2}{(T_2 - T_1)^4}\Delta T^2\right]$$

Equation 9

where Δn is the error associated with the measuring the index, ΔT the error associated with measuring the temperature, T_1 and T_2 are the initial and final temperatures, and n_1 and n_2 are the index measured at T_1 and T_2. As stated previously, the error on measuring the temperature was determined to be 0.3 °C. The error on the index was calculated by assuming $T_2 - T_1 = 0.3$ ℃, and propagating the error of this thermal stability throughout the measurement steps.

A 0.3 °C temperature error combined with a ZnSe dn/dT of 6.1 ppm·°C^{-1} (at 4.515 µm) corresponds to a "thermal system" error on the ZnSe index of ±0.00002, and the quoted error on the ZnSe index from M3MSI is ±0.0001. Combining these two error sources through a sum of the squares method results in an absolute ZnSe index error ±0.0001. This error is increased to ±0.0002 for the Ge measurement index (calibration index), as the small thermal error combined with the large dn/dT of Ge creates a larger uncertainty in the index. When adding in the systematic measurement errors associated with statistical repeatability, knee location identification, and knee quality, the total error on the index increases to ±0.0004.

Using the Ge prism index error of ±0.0004, and a thermal stability of 0.3 °C, the error of the samples measurements can be calculated. For the sample error, the individual errors from thermal stability, knee recognition / quality and statistical repeatability increase the sample index error to ±0.0005. There are two reasons the error on the measured sample

does not increase significantly compared to the Ge error. One is the fact that the knee quality was much higher for the glassy samples, as compared to the ZnSe samples. If the knee quality were to degrade with a poorly polished sample, the index would increase further. The second reason is that the dn/dT of the glass samples are much smaller than the dn/dT of Ge (~50 ppm $\cdot°C^{-1}$ vs ~450 ppm $\cdot°C^{-1}$) and thus don't contribute to the error as much. It is important to also not that the error on the index, and later dn/dT, was found to not mathematically change if the dn/dT of the sample was allowed to vary anywhere between -150 and +150 ppm $\cdot°C^{-1}$.

The error on the dn/dT was calculated by using the index error of ±0.0005, a thermal stability error of 0.3 °C, and a temperature window, $T_2 - T_1 = 60$°C. Substituting these values into Equation 9 yields an error on the dn/dT ±11.2 ppm$\cdot°C^{-1}$ for both the Ge calibration prism and for the glass samples.

Three methods have been identified to decrease the magnitude of the dn/dT error, based on analysis of Equation 9. These methods include improving the quality of the knee recognition and identification, decreasing the thermal fluctuations from 0.3 °C, and increasing the maximum temperature so that the temperature window is greater than 60 °C. It was calculated that solely decreasing the thermal fluctuations to within ± 0.1 °C would reduce the error on the dn/dT to 10.5 ppm$\cdot°C^{-1}$. Likewise it was found that solely increasing the temperature window to 100 °C (30 – 130 °C) would decrease the error on the dn/dT to ±6.7 ppm$\cdot°C^{-1}$. Finally improving the knee recognition and identification so that the statistical error on the index was ±0.0002 would decrease the error on the dn/dT to ±8.3 ppm$\cdot°C^{-1}$. Combining all three of these effects simultaneously would result in an overall

decrease of the dn/dT error to ±4.7 ppm·°C^{-1}. Limitations on sample properties, such as T_g, hardness, or final polish can also hinder the ability to achieve lower values for the dn/dT error by introducing local material variation that translates to the region of measurement.

The errors on the PNNL and UCF systems were deemed to be similar, as the two systems had the same thermal stability, and similar quality of knee recognition and repeatability. While reduction of the error on the dn/dT was not a focus of this project, Appendix B highlights some of the efforts to design thermal housing for the UCF system to decrease thermal fluctuations by an undergraduate student, Rebecca Whitsitt. Rebecca's addition to the system was added at the end of the current study and thus was not fully evaluated for improvements to the data presented herein that were measured without the thermal housing in place.

4.5.2 Repeatability of the UCF system (Relative Error)

As a way to determine the absolute measurement error, reproducibility, and absolute offset of the UCF system from a known reference material, a sample of IG 6 (Vitron $As_{40}Se_{60}$) was measured on a frequent basis. A square "coupon" sample measuring ~25 mm x 25 mm x 3 mm was cut from the center of a large boule of IG 6, and polished. The refractive index of this sample has been determined from the Vitron IG 6 data sheet [35], which provides a detailed fitting of the index as a function of both temperature and wavelength. The index at 4.515 µm was determined from their fitting, and is shown in Table 4.9 for the appropriate temperature set points. The calculated dn/dT at 4.515µm for the IG 6 sample is 34.4 ppm·°C^{-1}. The measured refractive index of the IG 6 sample is shown in Figure 4.13 along with the provided index from Vitron. There is an offset between the two data sets at 30 °C

and the dn/dT values are significantly different (34.4 ppm·°C^{-1} from Vitron, and ~76.8 ppm·°C^{-1} measured at UCF). Additional samples of IG 5 ($Ge_{28}Sb_{12}Se_{60}$) and IG 4 ($Ge_{10}As_{40}Se_{50}$), also from Vitron, were measured to determine the ability to reproduce published dn/dT data. Across all three IG samples, there was a consistent relative to the provided dn/dT data, averaging to 42.0 ppm·°C^{-1}. The measured values of dn/dT along with the datasheet values for dn/dT are shown in Table 4.8. As a result of this consistent offset, the decision was made to offset all values measured on the UCF system by the 42.0 ppm·°C^{-1}. These changes will be applied in selected areas of Section 4.7 and Section 4.9, where the trends in dn/dT results are analyzed and discussed

Table 4.8 – Offset between measured and datasheet values of dn/dT of IG samples.

Glass	Datasheet dn/dT (ppm·°C^{-1})	Measured dn/dT (ppm·°C^{-1})	Offset (ppm·°C^{-1})	Offset adjusted (ppm·°C^{-1})
IG 4	22.5	64.0	41.5	22.0
IG 5	63.5	106.5	43.0	64.5
IG 6	34.5	76.0	41.5	34.0

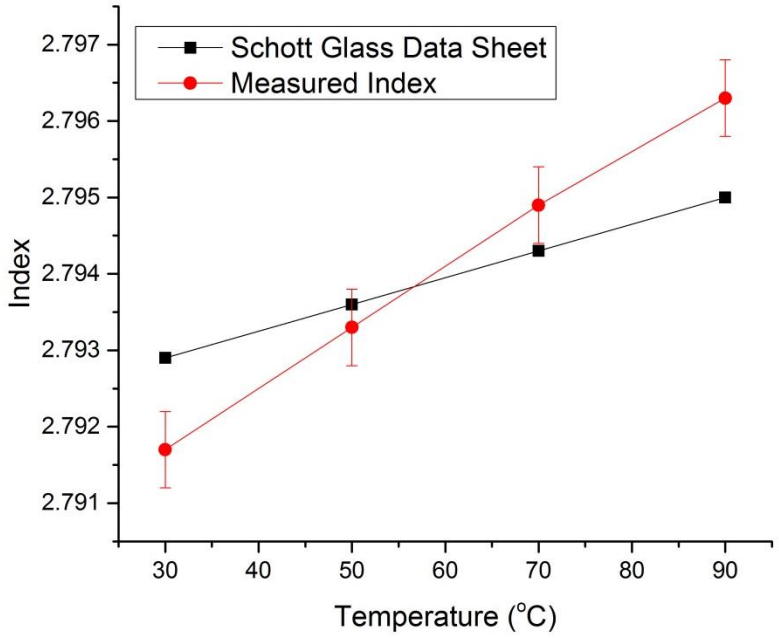

Figure 4.13 – Refractive index of IG 6 from Vitron (black) and measured refractive index at UCF (red).

The index of this sample was measured at 30 °C on a consistent basis, while the dn/dT was measured at various time intervals. The reason for the differing intervals between the dn/dT measurements will be explained in Chapter 5, which investigates the effect of "room temperature ageing" on samples and a subsequent index relaxation upon heating the sample to temperatures near to, but below the glass transition temperature. On the days the dn/dT was measured, and more importantly the full thermal cycling was performed, the reported refractive index at 30 °C is recorded, and shown in Figure 4.14.

Table 4.9 – Refractive index of the IG6 sample at the various temperature set points, as calculated from the Vitron data sheet

Temperature (°C)	Calculated Index (Vitron data sheet)
30	2.7929
50	2.7936
70	2.7943
90	2.7950

The measured refractive index of the IG 6 sample at 30 °C is shown in Figure 4.14, for each day the measurement was performed. There is little variance in the measured refractive index from day to day, and all of the measured index values are well within the errors of each other. The average measured index across 16 days of measurements is 2.7918 and is within an envelope of $\Delta n = 0.0006$, resulting in a *relative* index error of ± 0.0003.

The calculated dn/dT for each of these measurements is shown in Figure 4.15, for the days in which a full thermal cycling was actually performed. The measured dn/dT also agrees well from day to day, with variations remaining within the measurement error. The average dn/dT across 8 days is 76.0 ppm·°C^{-1} and is within an envelope of $\Delta dn/dT = 12.0$ ppm·°C^{-1}, resulting in a *relative* dn/dT error of ± 6.0 ppm·°C^{-1}. After applying the offset discussed previously, the average measured dn/dT for IG6 becomes 34.0 ± 6.0 ppm·°C^{-1}.

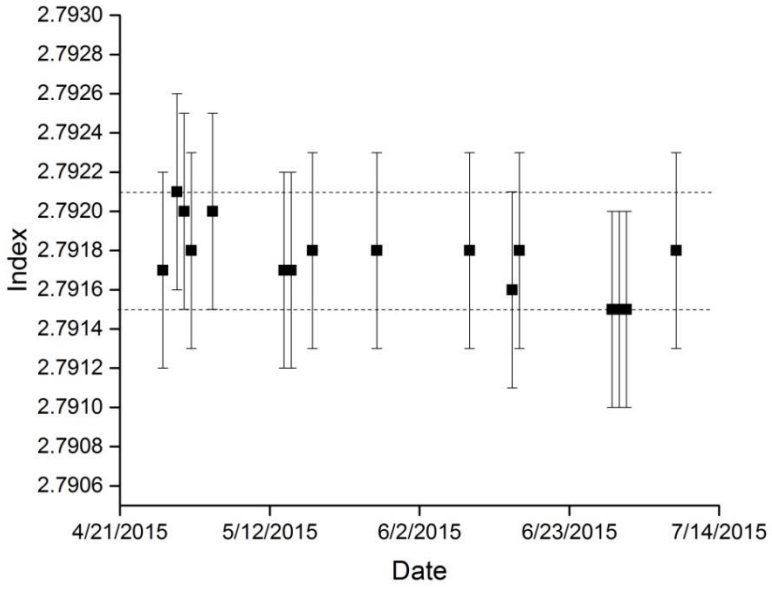

Figure 4.14 – Refractive index of the IG6 sample at 30°C for each of the measurement dates.

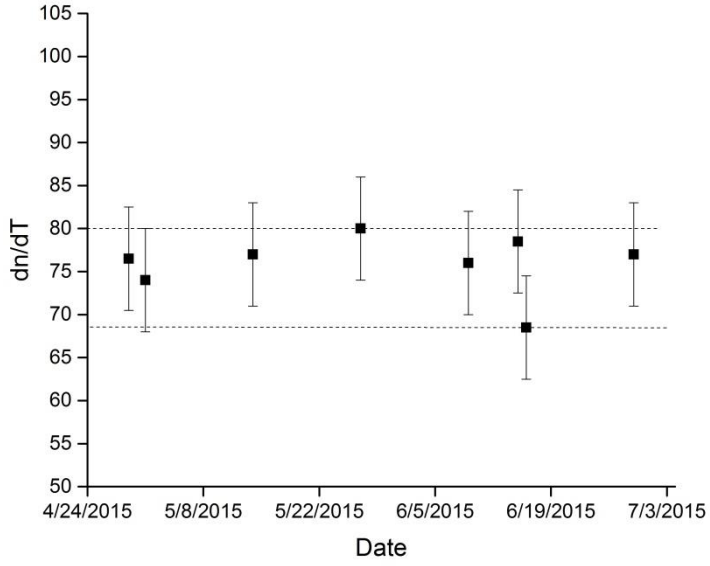

Figure 4.15 – dn/dT of the IG6 sample for each of the measurement dates.

4.6 GeAsSe Results - Refractive Index

4.6.1 PNNL results

The refractive index of each glass of the study was measured using the calibrated PNNLGe prism at 4.515μm. In total there are 17 GeAsSe glasses divided across three tielines, each with a unique As:Se ratio. The error on the refractive index measurements is ±0.0005 and is either within the size of the data points or specifically shown for all of the following figures.

First the refractive index for $As_{40}Se_{60}$ is shown in Figure 4.16, at 30, 50, 70, and 90 °C as a function of wavelength. This composition was measured at three additional wavelengths (3.39 μm, 5.4 μm, and 7.78 μm) to demonstrate that the GeAsSe glasses can also be fit with the same Sellmeier equation as the Ge measurement prism. The Sellmeier coefficients and the r^2 fitting value are listed in Table 4.10. There is obvious issue with the fitting at shorter wavelengths ($\lambda < 2.5$ μm), as all temperature fits appear to converge to the same predicted refractive index. To obtain a more realistic fit of the refractive index, additional wavelengths on both the shortwave and longwave ends of the spectrum need to be added to the fit.

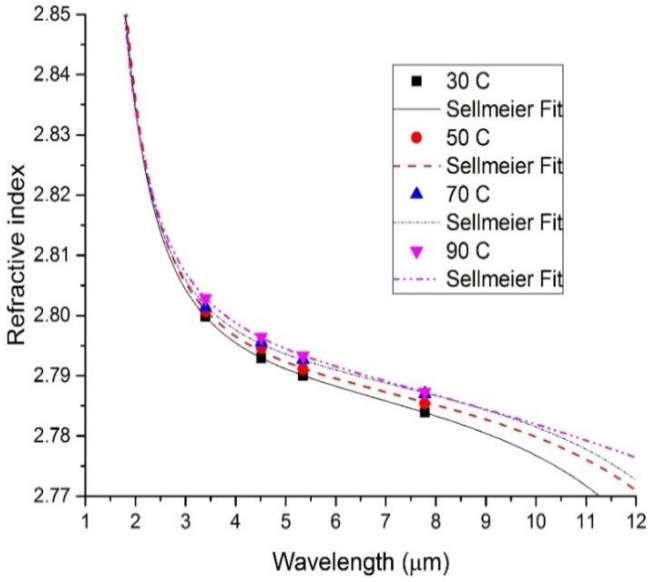

Figure 4.16 – $As_{40}Se_{60}$ refractive index vs wavelength at 30 °C, 50 °C, 70 °C, and 90 °C with corresponding Sellmeier fits.

The source at 4.515 μm was selected as the primary wavelength for compositional analysis of refractive index and dn/dT. This decision to limit the scope to this source was made based on the quality of the available laser sources, the available equipment time at PNNL, and the usefulness of this data in related projects.

Table 4.10 – Sellmeier coefficients and calculated r^2 values for Sellmeier fits

Temperature (°C)	A	B	C	D	E	r^2
30	6.99	0.78	1.01	0.10	15.87	0.999
50	6.99	0.78	1.02	0.10	16.95	0.997
70	7.00	0.78	0.99	0.10	16.99	0.997
90	6.97	0.82	0.95	2.00	57.77	0.999

The trends in the refractive index can be presented a number of ways, each with their own merits. The refractive index for all three GeAsSe tielines is shown in Figure 4.17, Figure 4.18, and Figure 4.19 as a function of added Ge to the starting AsSe binary composition.

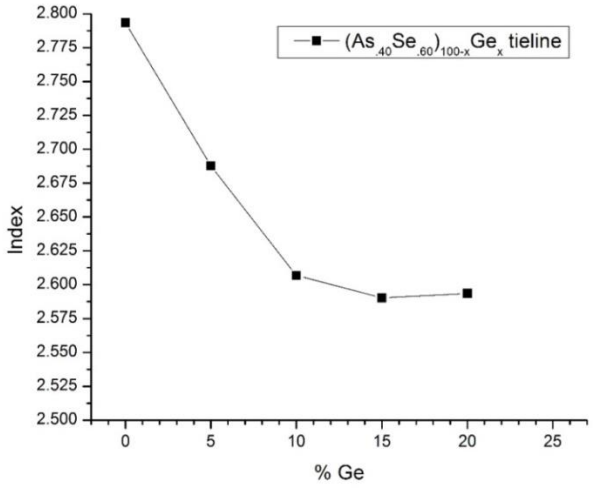

Figure 4.17 – Refractive index of the $(As_{.40}Se_{.60})_{100-x}Ge_x$ tieline at 4.515µm as a function of at% Ge

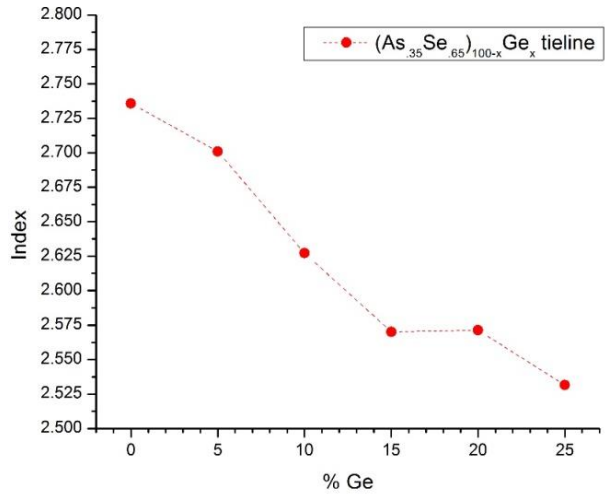

Figure 4.18 – Refractive index of the $(As_{.35}Se_{.65})_{100-x}Ge_x$ tieline at 4.515μm as a function of at% Ge

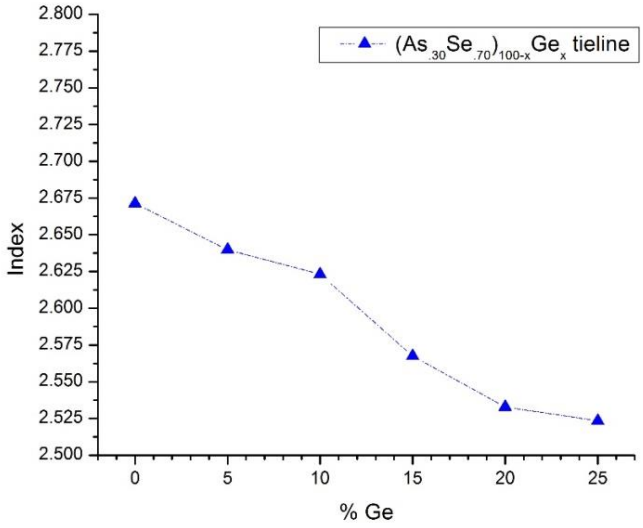

Figure 4.19 – Refractive index of the $(As_{.30}Se_{.70})_{100-x}Ge_x$ tieline at 4.515μm as a function of at% Ge

4.6.2 UCF Results

The goal for the construction of the UCF Metricon system was to replicate the ability of the PNNL Metricon system to measure both the refractive index and thermo-optic coefficient of samples at infrared (IR) wavelengths. To investigate the ability of the UCF prism to replicate IR index data, all of the aforementioned GeAsSe glasses that were measured on the PNNL system were also measured on the UCF system. Due to time constraints, the index and dn/dT measurements at UCF were also limited to one wavelength. The wavelength was specifically chosen to be the same as at PNNL: 4.515μm. The laser source used at UCF is a tunable optical parametric oscillator (OPO) from M^2 lasers (Firefly-IR). The tunability of the source allows for measurements of optical properties at additional wavelengths, with additional alignment and calibration, but the additional wavelengths were not the focus of these investigations.

The refractive index values for all of the glasses along the three GeAsSe tielines as measured on the UCF Metricon system are shown at 30 °C and 4.515 μm in Figure 4.20, Figure 4.21, and Figure 4.22, along with the original index values measured at PNNL. Unfortunately two of the compositions (40_60_5 and 30_70_0) had all of the remaining samples fracture do to various reasons and were unable to be measured on the UCF Metricon system. The symbols for these two data points are left hollow to signify that while the data was still collected, the measurements were performed on newly melted samples rather than the originals that were also measured at PNNL.

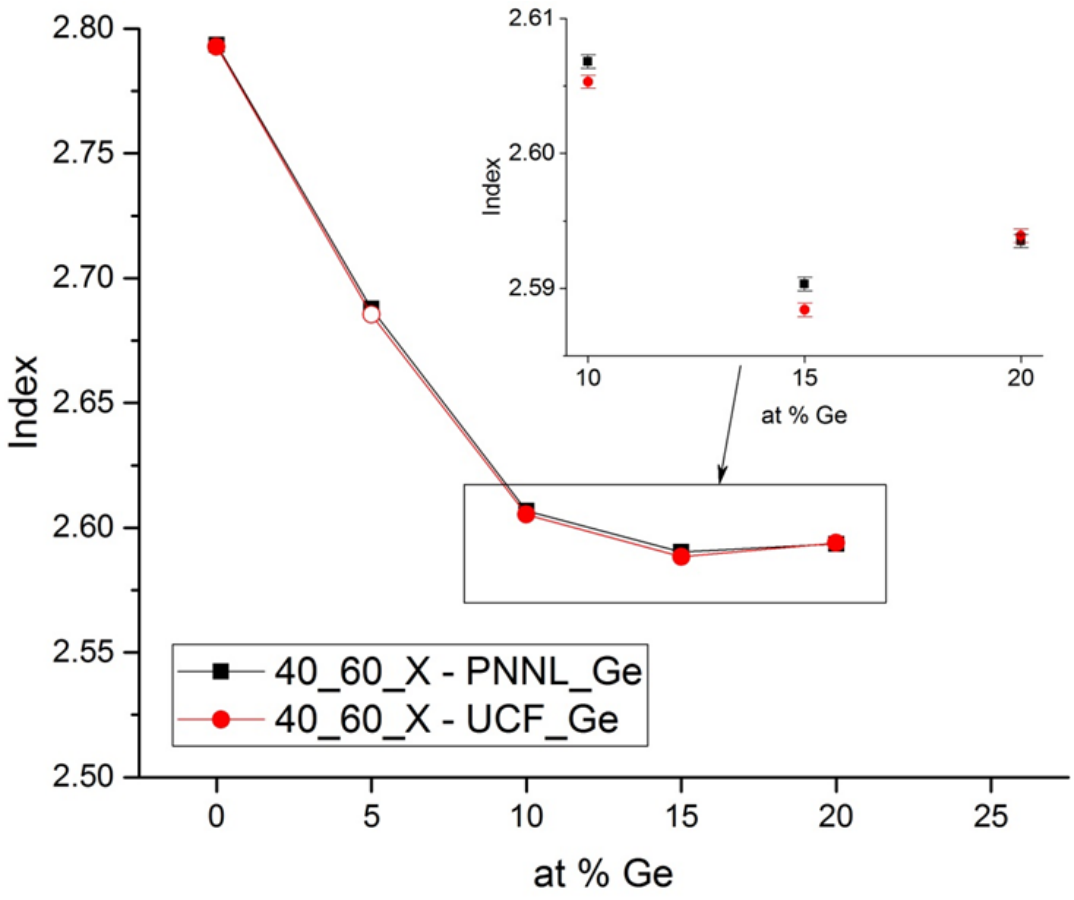

Figure 4.20 – Refractive index of the $(As_{.40}Se_{.60})_{100-x}Ge_x$ tieline measured at UCF at 4.515µm as a function of at% Ge, with inset graph to highlight similarities of measurements between the two systems.

The measurements show that the relative trends in refractive index observed with the PNNL system are preserved in UCF system as well. There is a consistent but small offset between the two measurement systems, with the PNNL system giving slightly higher index results (+0.0009 RIU). The difference in the refractive index, defined as the UCF-measured index subtracted from the PNNL-measured index, is shown in Figure 4.23 for all three tielines.

The offset in the measured index is believed to be a direct result of the unresolved Ge prism index offset observed between the PNNL and UCF systems. As previously stated, conversations with the manufacturer of the base system (Metricon Inc.) were unable to completely determine the origin of this offset.

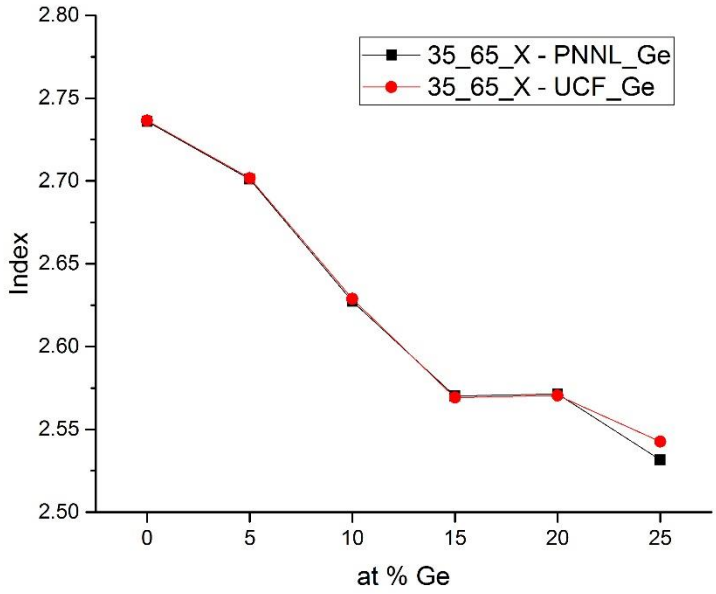

Figure 4.21 – Refractive index of the $(As_{.35}Se_{.65})_{100-x}Ge_x$ tieline measured at UCF at 4.515μm as a function of at% Ge

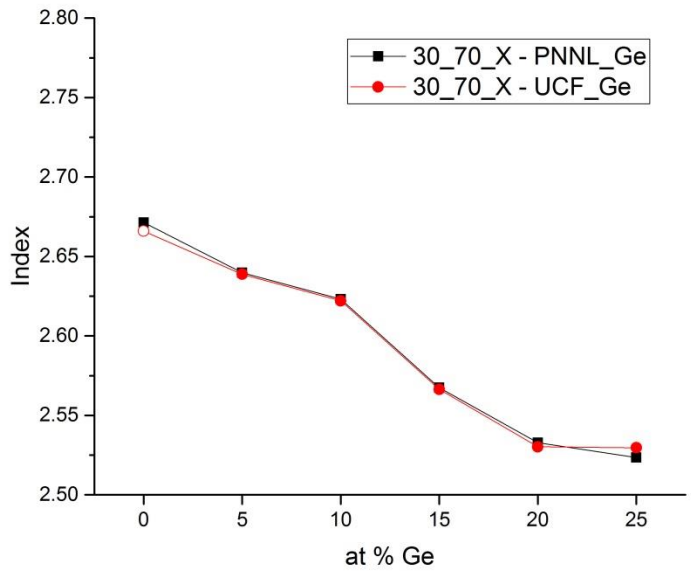

Figure 4.22 – Refractive index of the $(As_{.30}Se_{.70})_{100-x}Ge_x$ tieline measured at UCF at 4.515µm as a function of at% Ge

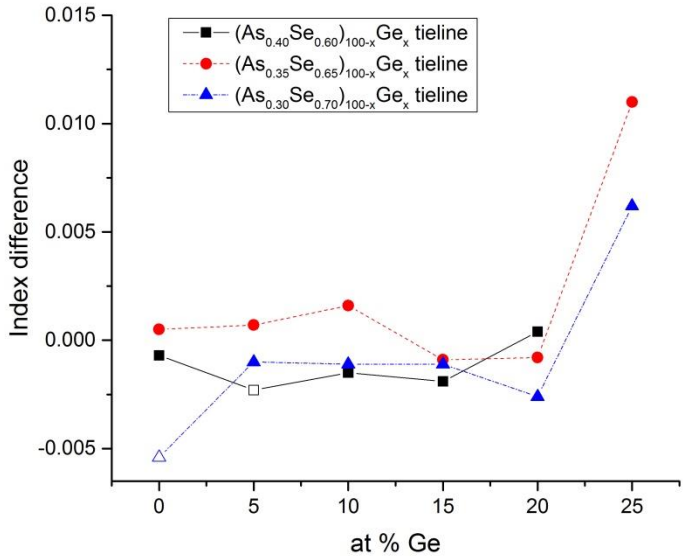

Figure 4.23 – Difference between the refractive index measured on the PNNL and on the UCF systems at 4.515µm

4.7 GeAsSe Results – Thermo-optic Coefficient (dn/dT)

4.7.1 PNNL Results

The change in index with temperature is shown again for $As_{40}Se_{60}$ in Figure 4.24, here with the wavelengths separated and plotted as function of temperature. The dn/dT is calculated for this in the same manner as for the Ge measurement prism: the slope of the best fit line for the change in index with temperature is calculated and reported as the dn/dT. The calculated dn/dT values and the corresponding r^2 values for the fits are listed in Table 4.11.

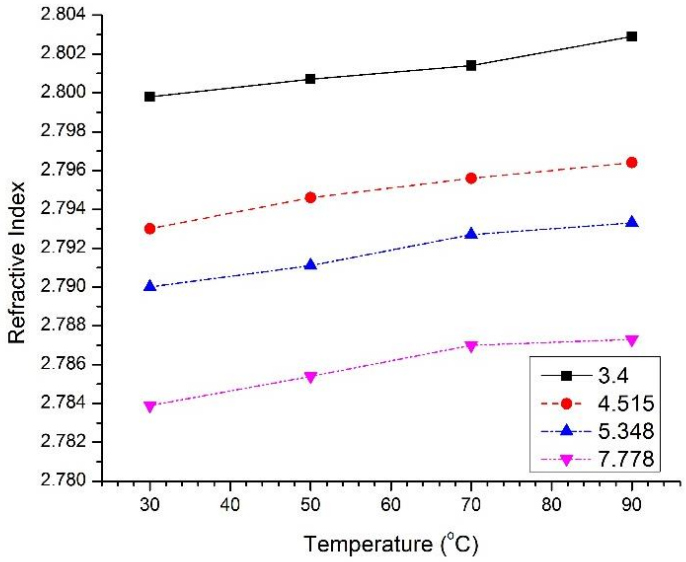

Figure 4.24 – $As_{40}Se_{60}$ refractive index vs temperature for individual wavelengths

Table 4.11 – Calculated dn/dT of $As_{40}Se_{60}$ and r^2 values from linear fits

Wavelength (µm)	dn/dT ±11.2 ppm·°C^{-1}	r^2 of linear fit
3.4	50.0	0.959
4.515	56.0	0.960
5.348	57.5	0.961
7.778	59.0	0.907

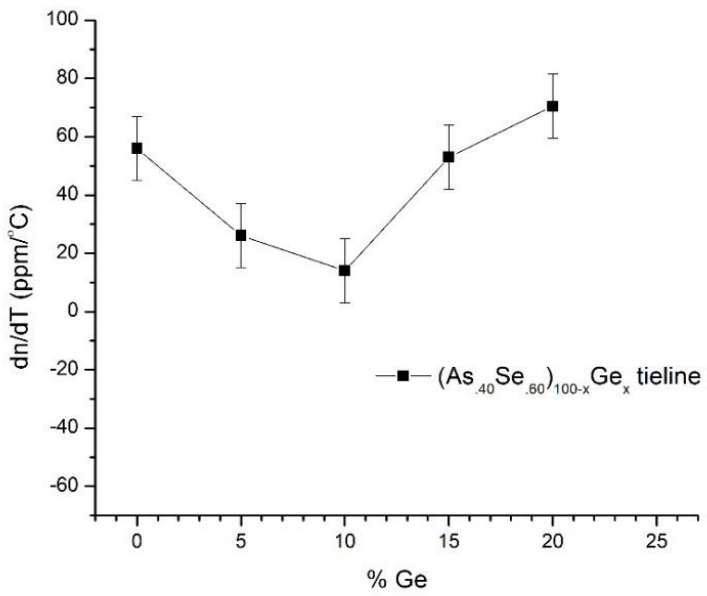

Figure 4.25 – dn/dT of $(As_{.40}Se_{.60})_{100-x}Ge_x$ tieline at 4.515μm as a function of at% Ge

The dn/dT is shown in Figure 4.25, Figure 4.26, and Figure 4.27 for the three respective tielines as a function of added Ge to the starting AsSe binary compositions. Along the AsSe binary, there is a large decrease in the dn/dT with increasing Se content. The dn/dT ranges from +56.0 ppm·°C^{-1} for $As_{40}Se_{60}$ to -41.0 ppm·°C^{-1} for $As_{30}Se_{70}$. Adding Ge to the two Se-excessive compositions results in a linear increase in dn/dT until stoichiometry is reached. After passing stoichiometry all three tielines exhibit either a plateau or a decrease in the dn/dT. As the compositions become more Se deficient, all three tielines exhibit a second change in their trends. From this point onward, the dn/dT increases with Ge additions. The two changes observed in the dn/dT trends of the three tielines is analogous to the changes observed in the refractive index. Remember that the $(As_{.35}Se_{.65})_{100-x}Ge_x$ and $(As_{.30}Se_{.70})_{100-x}Ge_x$ tielines showed only a small change in index with Ge while Se

excessive, and here these two tielines show an increase in dn/dT with Ge. Once all three tielines are in the Se deficient region, the rate of change of index and dn/dT of the $(As_{.35}Se_{.65})_{100-x}Ge_x$ and $(As_{.30}Se_{.70})_{100-x}Ge_x$ tielines resemble the $(As_{.40}Se_{.60})_{100-x}Ge_x$ tieline more closely. Finally once all three glasses have reached the level of Se deficiency necessary to promote formation of new structures, all tielines show a similar change in index and dn/dT trends.

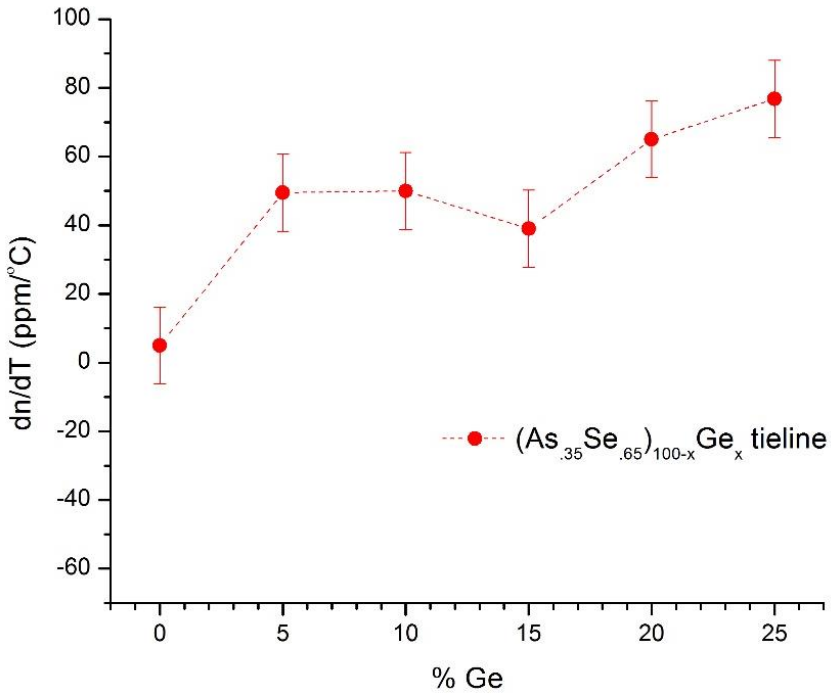

Figure 4.26 – dn/dT of $(As_{.35}Se_{.65})_{100-x}Ge_x$ tieline at 4.515μm as a function of at% Ge

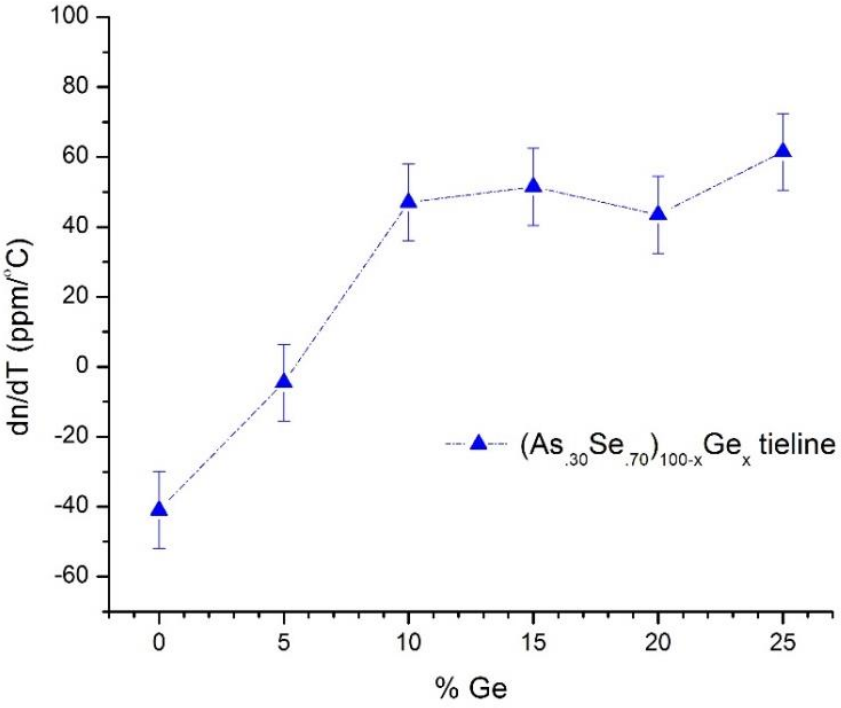

Figure 4.27 – dn/dT of $(As_{.30}Se_{.70})_{100-x}Ge_x$ tieline at 4.515µm as a function of at% Ge

4.7.2 UCF Results

The dn/dT of the GeAsSe glass samples was also measured using the UCF Metricon system. The same procedure for measuring dn/dT that was developed at PNNL was followed. The dn/dT values measured on both systems at 4.515 µm and calculated between 30 °C and 90 °C for all three tielines are shown in Figure 4.28, Figure 4.29, and Figure 4.30. Similar to the replication of the 30 °C index measurements, the compositional trends in dn/dT observed at PNNL are also observed with the UCF system.

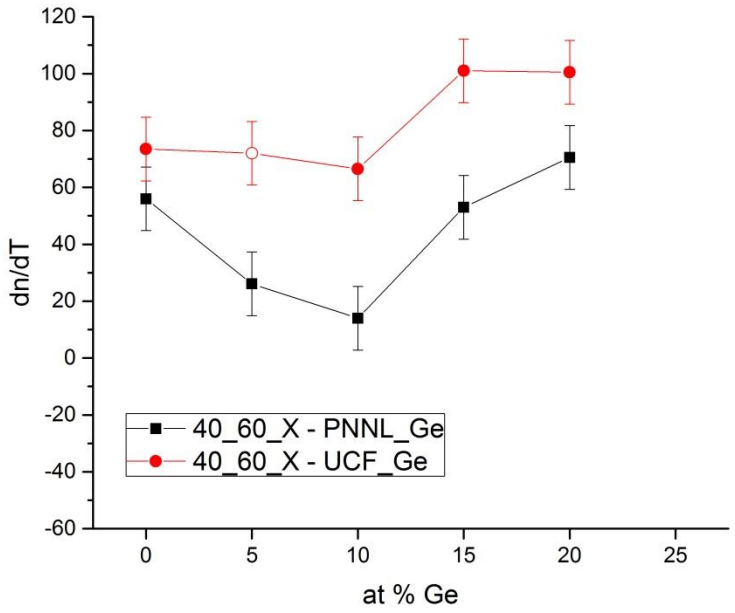

Figure 4.28 – dn/dT of $(As_{.40}Se_{.60})_{100-x}Ge_x$ tieline measured at UCF at 4.515µm as a function of at% Ge

The measured dn/dT of the GeAsSe glasses on the UCF was significantly higher than measured on the PNNL system. The difference between the two data sets, defined as the UCF dn/dT subtracted from the PNNL dn/dT, is shown in Figure 4.31 for all three tielines and averages to +30.2 ppm·°C^{-1} t. The origin of this offset is believed to be a result of improper calibration of the Ge prisms. This could come from either a mis-calibration of the temperature and/or the refractive index. It is important to note that recalibrating the system would result in a nearly DC offset for both the refractive index and the dn/dT for all glasses.

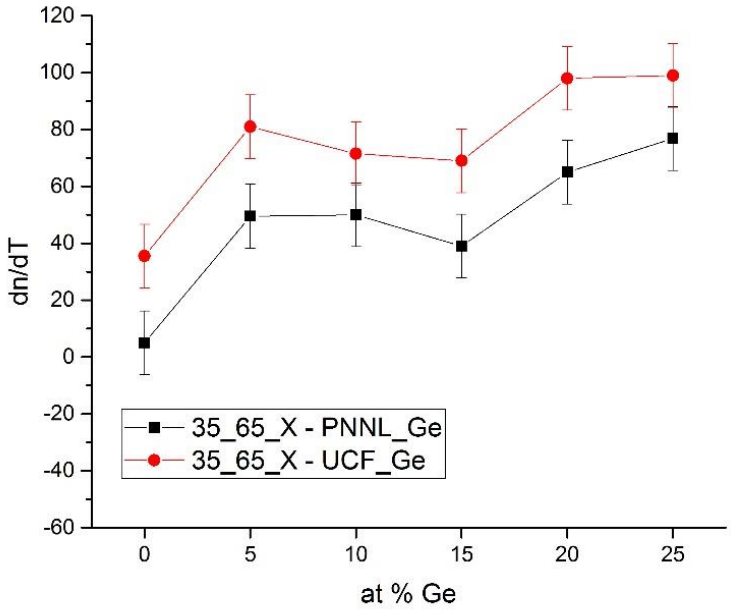

Figure 4.29 – dn/dT of $(As_{.35}Se_{.65})_{100-x}Ge_x$ tieline measured at UCF at 4.515µm as a function of at% Ge

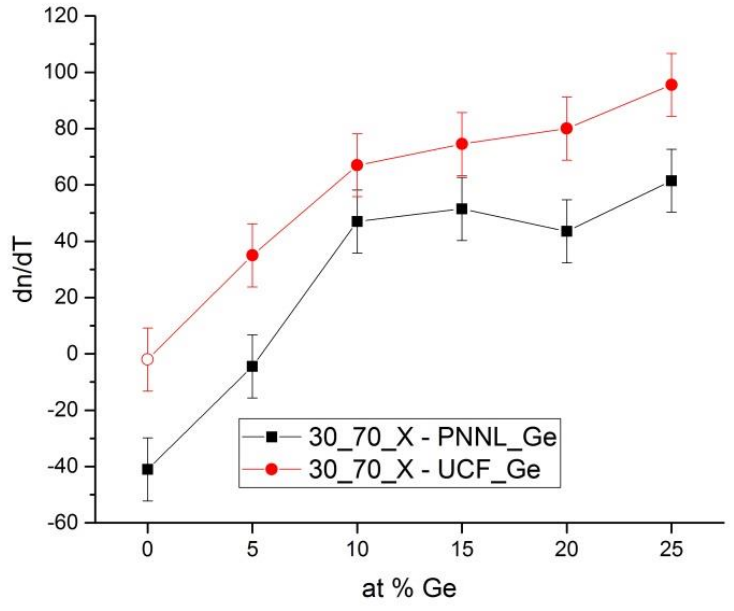

Figure 4.30 – dn/dT of $(As_{.30}Se_{.70})_{100-x}Ge_x$ tieline measured at UCF at 4.515µm as a function of at% Ge

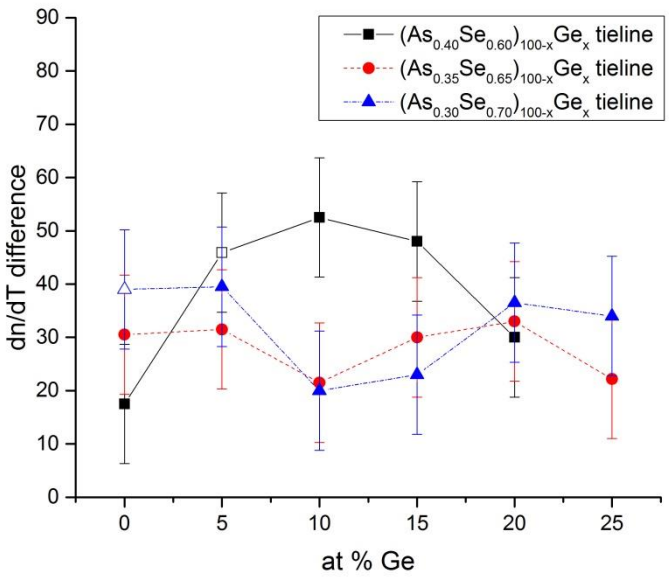

Figure 4.31 – Difference between the dn/dT measured on the PNNL and on the UCF systems at 4.515µm

After applying the offset to the UCF system discussed in Section 4.5.2, the difference between the measured dn/dT on the UCF and PNNL systems decreases from +30.2 ppm·°C^{-1} to -11.8 ppm·°C^{-1}. With the offset applied, the average difference between the PNNL and UCF systems is slightly larger than the measurement error (±11.2 ppm·°C^{-1}).

4.8 Melt Homogeneity

Attempting to quantify sometime small variations in refractive index between different compositions requires confidence that such small variations are outside of the intrinsic variation in index seen within a given melt. Since large melts prepared by commercial chalcogenide glass manufacturers (typically > 3kgs) are considered large enough to average out melt inhomogeneities that arise from density fluctuations resulting from melt vessel size, shape and melt and annealing time, the small melts prepared in this academic

study are likely much less homogeneous than commercial material. Despite the small melts (typically 25g) efforts were made to assess variation both within melt and across varying melts to estimate such variation. The results of these studies are discussed here. Note that the linear offset in the dn/dT presented in Section 4.5.2 (-40.2 ppm·°C^{-1}) is not accounted for here, as it would apply equally to all samples measured.

4.8.1 Within melt refractive index uniformity

The entire $(As_{0.35}Se_{0.65})_{100-x}Ge_x$ tieline was remelted in order to gain an understanding of the index homogeneity within melts, as well as the melt to melt reproducibility possible when melting an identical composition under identical conditions. From each of these 25g melts, fabricated following melt, quench, and annealing conditions discussed in Section 2.1.1, slices were taken from the top, middle, and bottom of the boule for analysis. The approximate location of each of the samples is shown in Figure 4.32. The samples maintained the same geometry as the original melts, 10mm in diameter and ~2mm in thickness. The refractive index of three samples from each melt was measured using the same protocol as described before.

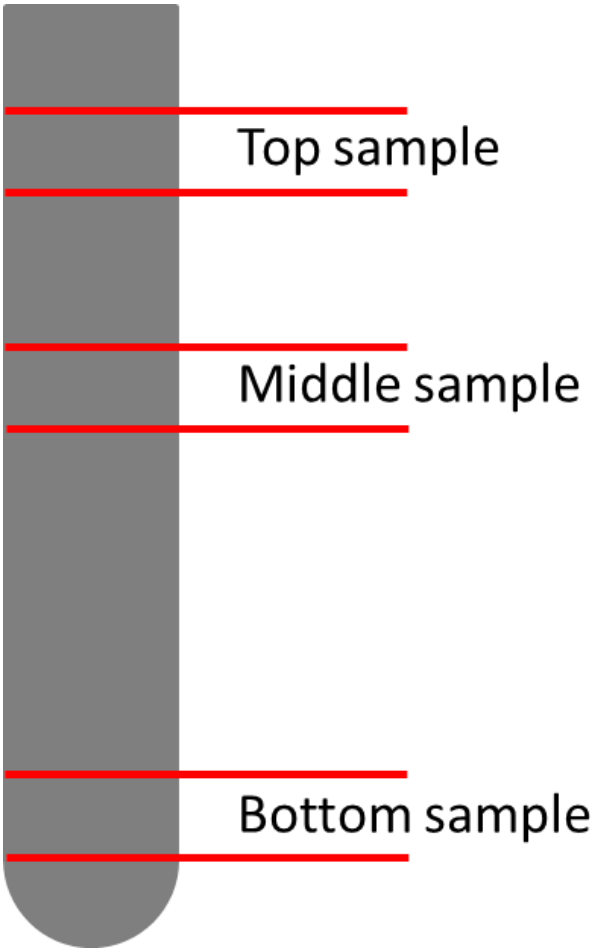

Figure 4.32 – Schematic of the glass boule showing the approximate location of the top, middle, and bottom samples.

The refractive index for the top, middle, and bottom slices are shown for the additional melt of 35_65_10 in Figure 4.33 as a function of temperature. In this representative case, the measured index of the top and middle samples agree well for all temperatures, while the bottom slice consistently yields a higher refractive index.

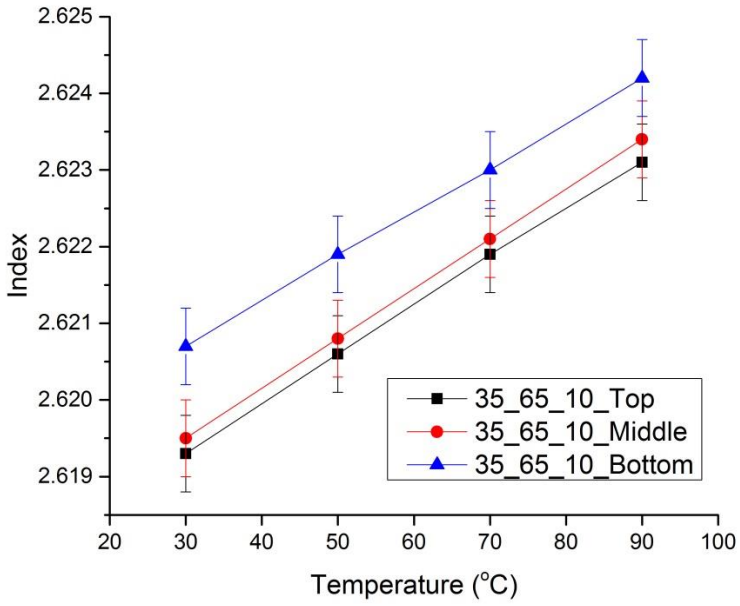

Figure 4.33 – Refractive index at incremental temperatures of the top, middle, and bottom slices of a representative remelt along the 35_65_X tieline

4.8.2 Melt-to-melt refractive index uniformity

The refractive index of the top, middle, and bottom slices for all melts along the 35_65_X tieline is shown in Figure 4.34 along with the data from the original melts (as measured on the UCF Metricon system in Section 4.5.1). When viewing the changes in refractive index on the scale necessary for compositional analysis, the differences in index within the melt and from melt to melt appear to be minimal. The refractive index of the top, middle, and bottom samples for all melts along the 35_65_X tieline are listed in Table 4.12. Two additional values are also calculated in this table: the index difference between the top and bottom samples, and the difference between the averaged index for the three samples of the new melts and the original melts.

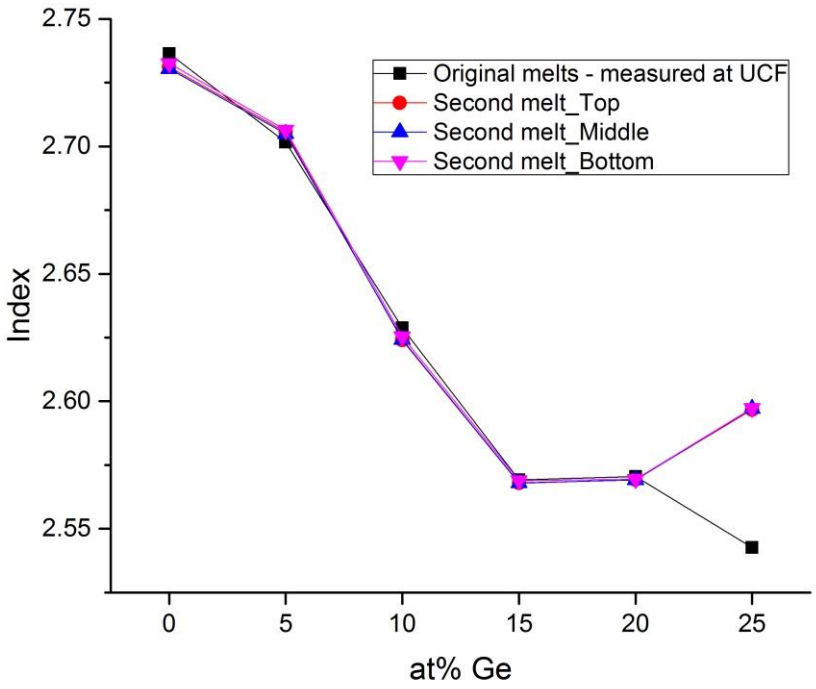

Figure 4.34 – Refractive index of the top, middle, and bottom slices of the remelts along the 35_65_X tieline, along with the data from the original melts, as measured on the UCF Metricon system.

The dn/dT for each top, middle, and bottom slice was also calculated by taking a linear fit of the index data with temperature. The dn/dT for the three slices, along with the dn/dT from the original melts (as measured on the UCF system) is shown in Figure 4.35. As with the refractive index values at 30 °C, the dn/dT for the second melts of the 35_65_X tieline glasses are consistently lower than the original melts.

The lower measured dn/dT and the higher measured index of the bottom samples is an interesting result. Given that compositions with lower Ge content (generally) have a higher index, and a lower dn/dT , the results from this homogeneity test suggests that during the

melting the heavier elements (Se and As) began to settle to the bottom of the tube. This could signify improper mixing (rocking) during the melting, or that the time in which the melt was left vertical (just prior to quench) is long enough for settling of heavier elements to occur.

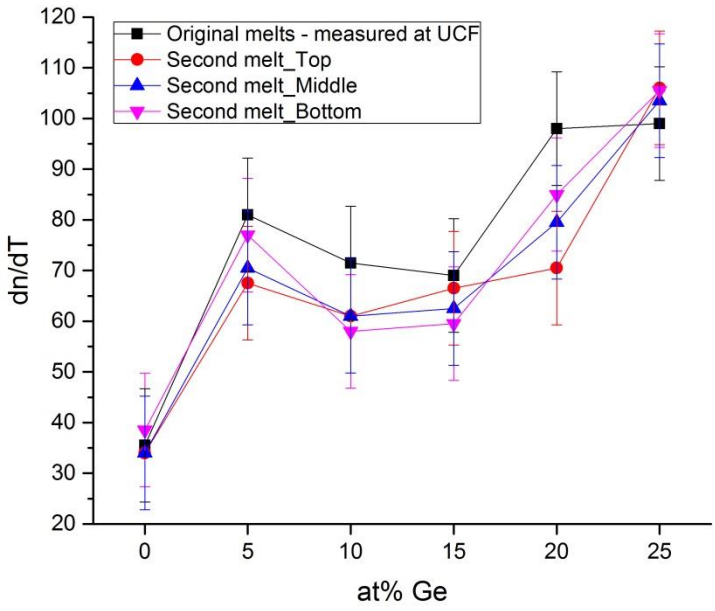

Figure 4.35 – dn/dT of the top, middle, and bottom slices of the remelts along the 35_65_X tieline, along with the data from the original melts, as measured on the UCF Metricon system.

Table 4.12 – Refractive index of the top, middle, and bottom samples for the 35_65_X

Composition	Original melt data	Second melt: Top	Second melt: Middle	Second melt: Bottom	Index difference: top - bot	Index difference between old melt and new melt
35_65_0	2.7364	2.7311	2.7305	2.7325	0.0014	0.0050
35_65_5	2.7017	2.7056	2.7050	2.7064	0.0008	0.0047
35_65_10	2.6288	2.624	2.6242	2.6254	0.0014	0.0043
35_65_15	2.5692	2.5679	2.568	2.5689	0.0010	0.0009
35_65_20	2.5705	2.5693	2.5692	2.5694	0.0001	0.0012
35_65_25	2.5426	2.5967	2.5971	2.5973	0.0006	-0.0544

Table 4.13 – dn/dT of the top, middle, and bottom samples for the 35_65_X tieline

Composition	Original melt data (ppm °C^{-1})	Second melt: Top (ppm °C^{-1})	Second melt: Middle (ppm °C^{-1})	Second melt: Bottom (ppm °C^{-1})	dn/dT difference: top – bot (ppm °C^{-1})	dn/dT difference between old melt and new melt (ppm °C^{-1})
35_65_0	35.5	34	34	38.5	4.5	0.0
35_65_5	81	67.5	70.5	77	9.5	9.3
35_65_10	71.5	61	61	58	3.0	11.5
35_65_15	69	66.5	62.5	59.5	7.0	6.2
35_65_20	98	70.5	79.5	85	14.5	19.7
35_65_25	99	106	103.5	105.5	2.5	-6.0

4.8.3 Scaling of melt size

The target application for these glasses is in infrared imaging systems. In order for these glasses to potentially be used as potential new materials for target applications, they must be able to be produced on a large (or simply larger) scale than is typically done in a laboratory setting. Scaling up a melt size, say from 25g to 250g, can result in different properties within the glass and can require new melt-quench protocols to produce a uniform, homogeneous glass. To assess the ability of these glasses to be "scaled up" to larger melts, several compositions were selected and 250g batches were prepared in 30 mm diameter silica ampules.

For this analysis, the melt-quench protocol was held the same, with the knowledge that this may not produce the most ideal glass at this specific melt size. The glasses were melted in a rocking furnace overnight at 750 °C, with a ramp rate of 2.5 °C min^{-1}. The rocking is then stopped and the temperature is then dropped to 650 °C. The melt was removed and then then quenched to room temperature with forced air. The main difference between the quenching of the small melts (25g) and the large melts (250g) is the time needed to quench to room temperature, and the "aggressiveness" needed of the forced air.

The specific compositions that were chosen for further analysis are listed in Table 4.14. The two glasses along the 40_60_X tieline were initially melted for an analysis of viscosity, and as such were sliced "vertically" rather than "horizontally". These two different sample orientations are shown in Figure 4.36. The advantage of cutting the slices "vertically" is that this sample geometry allows for a 2D mapping of both the refractive index and dn/dT of a cross-section of the melt. The main disadvantage of this sample geometry lies in the fabrication of these samples, where it is difficult to cut a large cross-section without damaging the sample, as was the case for the 40_60_10 sample.

For the 40_60_10 and 40_60_20 samples, the measurement locations are also noted in Figure 4.36 by the red Xs. For the 35_65_10 and 35_65_20 samples, the standard disk forms, the index and dn/dT was measured at 5 locations across the diameter of the sample. The 2D mapping of the index and dn/dT of the 40_60_10 and 40_60_20 samples are shown in Figure 4.37 and Figure 4.38, respectively.

The 2D mapping of the index reveals that the larger melts have a wide variability in the refractive index, ~0.0030 for 40_60_10 and ~0.0090 for 40_60_20. In both cases the higher refractive index was found in the lower part of the glass boule. A higher refractive index was also observed for the "bottom" samples in the 35_65_X small melts, but the magnitude was much larger for the large melts.

Variations in the dn/dT were also observed in these two large melts, but did not show a gradient from top to bottom of the melt. A higher dn/dT was generally found in the center of the melt, but this was not always consistent. Relative to the error of the measurements

(index ± 0.0005, dn/dT ± 11.2 ppm·°C^{-1}) the variation in the dn/dT is much smaller when compared to the refractive index.

The refractive index and dn/dT of the 35_65_10 and 35_65_20 samples are shown in Figure 4.39 and Figure 4.40, respectively. Again, these two samples were sliced differently, which prevents the 2D mapping presentation of the previous two glasses. The 35_65_10 sample showed a very uniform refractive index profile, with all measurements being within the error of the average index. The 35_65_20 sample showed a higher refractive index at the bottom of the melt, as was observed in the first two large melts, as well as the smaller melts. The dn/dT for these two melts also showed a generally higher dn/dT in the center of the sample rather than along the edges of the sample.

Overall, the average measured dn/dT of the large melts was within the established error of the corresponding average measured dn/dT of the small melts. The average refractive index of the large melts however, differed from the corresponding average index from the small melts by up to 0.0065, or approximately 13x the size of the index error. A listing of the average index and dn/dT for both the large and small melts is shown in Table 4.14.

Table 4.14 – Refractive index and dn/dT values of 25g melts and 250g melts for selected compositions.

Composition	Sample orientation	Small melt index – average	Small melt dn/dT – average	Large melt index – average	Large melt dn/dT – average
40_60_10	Vertical	2.6053	66.5	2.6063	72.7

40_60_20	Vertical	2.5939	100.5	2.6004	103.4
35_65_10	Horizontal	2.6288	71.5	2.6231	69.5
35_65_20	Horizontal	2.5705	98.0	2.5675	88.7

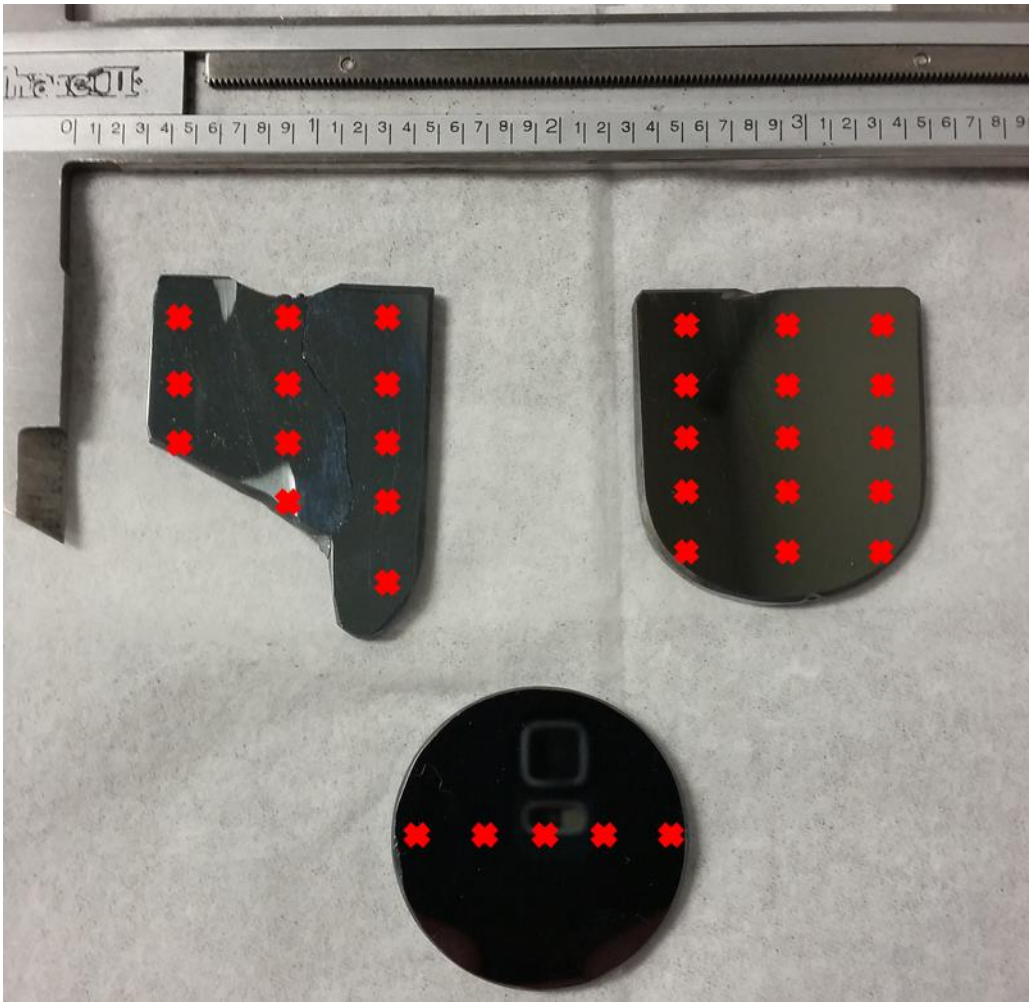

Figure 4.36 – Cross section of the 40_60_10 (top left) and 40_60_20 (top right) large melt sample, which were sliced "vertically" and a representative sample (bottom) of the 35_65_10 and 35_65_20 melts which were cut "horizontally". The 40_60_10 sample was damaged during fabrication, producing the irregular shape. The red X markers designate the approximate locations of measurements.

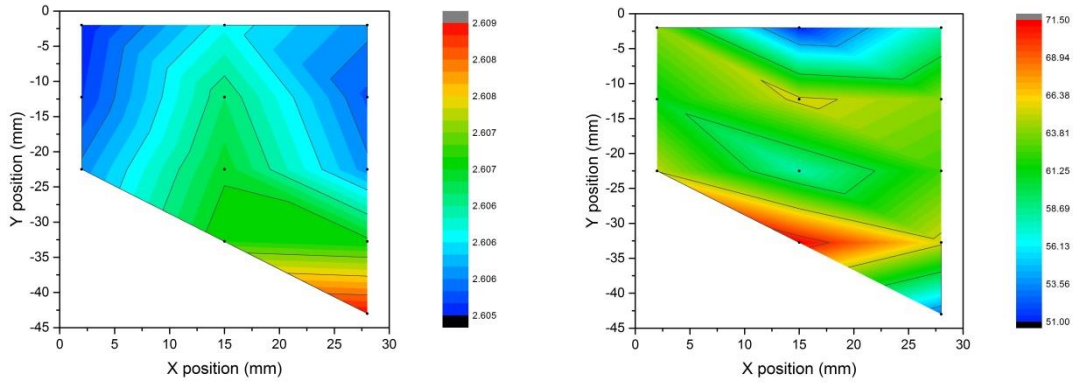

Figure 4.37 – Two-dimensional mapping of a) the index and b) the dn/dT of the 40_60_10 large melt cross-section, measured at 4.515 µm.

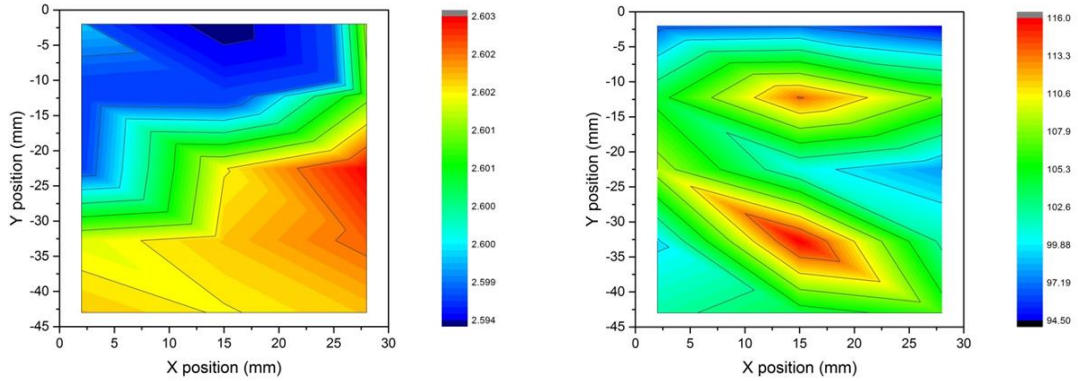

Figure 4.38 – Two-dimensional mapping of the index of the 40_60_20 large melt cross-section, measured at 4.515 µm and 30 °C

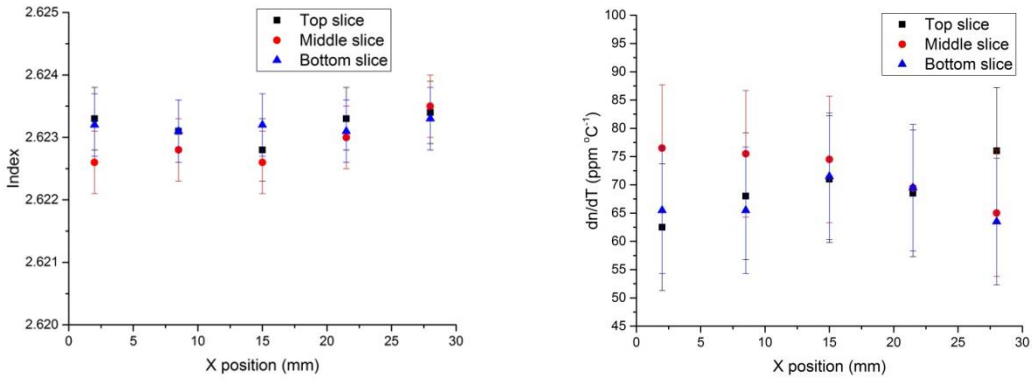

Figure 4.39 – The a) index and b) dn/dT of the 35_65_10 sample, measured at 4.515µm

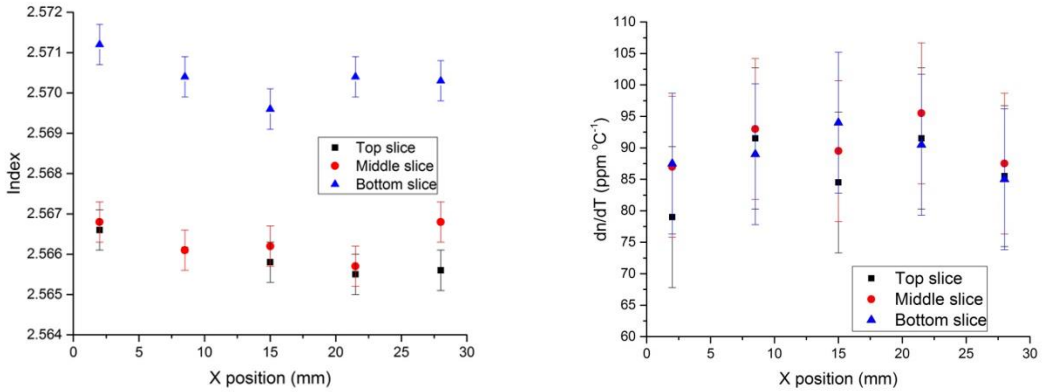

Figure 4.40 – The a) index and b) dn/dT of the 35_65_20 sample, measured at 4.515µm

4.8.4 Annealing of large melts

The large index variations in the 250g melts could potentially be a result of thermal history variations (uneven cooling), or variations in chemistry throughout the melt. In order to determine the origin of these variations, the large melt samples of 40_60_10 were annealed at a temperature 40 °C lower than T_g for 3 days. The assumption was that any thermal history variations would be sufficiently relaxed out of the glass during this exaggerated

annealing step. After slowly returning the sample to room temperature, the refractive index was measured again at 30 °C, in approximately the same locations as shown in Figure 4.36. The resulting index after the 3 day anneal is shown in Figure 4.41. The refractive index in the 40_60_10 sample became much more uniform after this secondary annealing step, decreasing the Δn from 0.0029 to 0.0016, a reduction of almost 50%.

The drastic reduction in the Δn across the sample leads to two important observations. First, variations in thermal history and internal stresses are important in determining the refractive index of a chalcogenide glass. Second, either the overnight annealing of the glass is not sufficient to ensure a uniform thermal history, or the process "cross sectioning" the boule may impart additional stresses on the sample and lead to refractive index changes. Unlike typical slicing and polishing, cross-sectioning a glass boule requires mounting and unmounting of the glass using thermal wax, potentially altering the thermal history of the sample. For purposes of future examination of this compositional system, longer anneals with attention to the extent of heating (rate and upper temperature during mounting for fabrication) should be considered to realize high index homogeneity samples.

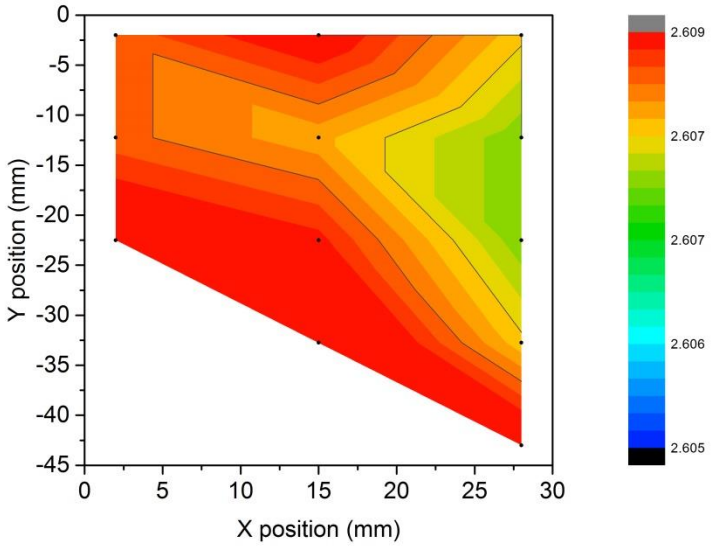

Figure 4.41 – Two-dimensional mapping of the refractive index of the 40_60_10 large melt cross-section after annealing, measured at 4.515 µm.

4.9 Analysis and Modeling

The analysis of the refractive index and thermo-optic coefficient in this section has been performed on values measured at UCF rather than at PNNL. Additionally, the values used for the $(As_{0.35}Se_{0.65})_{100-x}Ge_x$ tieline have been taken from the average values from the small-melt homogeneity investigation detailed in Section 4.8.2.

4.9.1 Refractive Index

The $(As_{.35}Se_{.65})_{100-x}Ge_x$ and $(As_{.30}Se_{.70})_{100-x}Ge_x$ tielines each contain compositions that are in the Se-excessive region. The change in index with composition in this region is linear and approximately the same for both tielines. In the region with a weak Se deficiency, the change in index with composition for the three tielines is approximately three times larger than in the region with a Se excess. Another slope change is observed when the network

has reached approximately -20% Se-poor percentage, followed by a broad minimum when the network is between -20% and -30% Se-poor in all three tielines.

As previously noted, at a Se-rich/-poor percentage of 0%, the composition is in stoichiometry and the structures in the network differ depending on which side of this transition point a composition may lie. Additionally, as noted in the introduction, when the network is sufficiently Se-poor, structures such as GeSe ethane-like modes become present. In the work of Xu et al., XPS/NMR studies showed the appearance of these specific structures on three compositions with a Se-rich/-poor percentage of approximately -30% [62].

The refractive index of all three tielines is shown in Figure 4.42a and 4.42b, as a function of the MCN and the %Se rich/poor, respectively. Figure 4.42a contains two dashed lines, one at MCN = 2.4 and another at MCN = 2.67, signifying the two points where possible transitions have been predicted and observed in other works. Similarly Figure 4.42b contains a dashed line corresponding to the change in structures at stoichiometry (0% Se-rich or Se-poor) and a shaded zone corresponding to the region where $Ge_2Se_{6/2}$ ethane-like modes are expected to appear (between approximately -20 and -30 % Se-poor). The fact that the changes experience an inflection at these points signifies that the index is extremely sensitive to the structures that are present in a given composition.

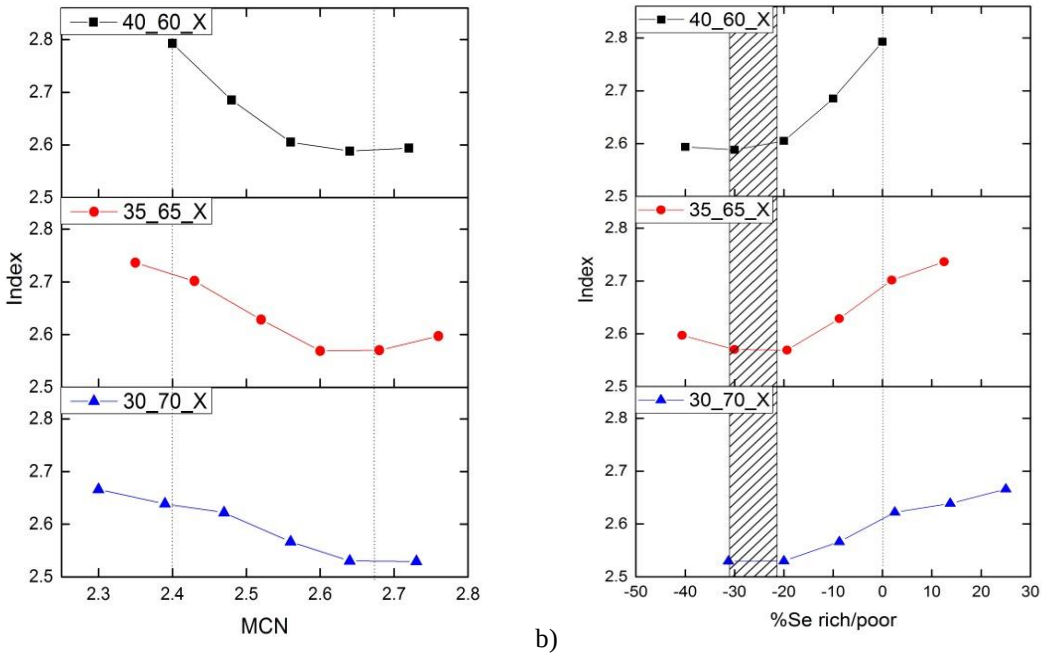

Figure 4.42 – Thermo-optic coefficient of the three GeAsSe tielines as a function a) MCN and b) %Se rich/poor. Vertical lines and shaded regions are shown to highlight locations of theorized transitions along the tielines.

4.9.2 Single Frequency Optical Model (Lorentz-Lorenz)

The Lorentz-Lorenz (LL) equation allows calculation of a material's polarizability (α), or molar refractivity (R_m) based on its molecular weight (M), density (ρ), and refractive index (n).

$$\frac{4\pi}{3}N\alpha = R_m = \frac{M}{\rho}\left(\frac{n^2-1}{n^2+2}\right)$$

Equation 10

Expressing the mass as molar volume (V_m) and solving the above equation for the refractive index yields a relation of the index to the dimensionless ratio R_m/V_m.

$$n = \sqrt{\frac{2\left(\frac{R_m}{V_m}\right) + 1}{1 - \left(\frac{R_m}{V_m}\right)}}$$

Equation 11

A multi linear regression was performed using index and density data to determine the refractivity values for Ge, As, and Se that would yield the best results for the LL model. The fitting resulted in a refractivity value for Se of 11.29 cm^3/mol, a refractivity value for As of 12.13 cm^3/mol, and a refractivity value for Ge of 9.59 cm^3/mol. Comparing to previous values of refractivity published by Webber et al. [66], 11.26 cm^3/mol for Se, 11.33 cm^3/mol for As, and 10.29 cm^3/mol for Ge, the refractivity for Se remains essentially unchanged while the values for Ge and As differ significantly. The calculated index using the fitted refractivity values and Equation 11 is shown in Figure 4.43, Figure 4.44, and Figure 4.45 for each of the respective tielines.

The refractivity values obtained here provide a reasonable estimate of a composition's refractive index, and can be useful for preliminary steps in compositional design. The LL model however, does not consistently predict "knees" or extrema with composition, as has been noted by McCloy et al. [145]. The reasoning for this is likely due to the model only considering elemental refractivity contributions and ignoring contributions from specific structures or bond types.

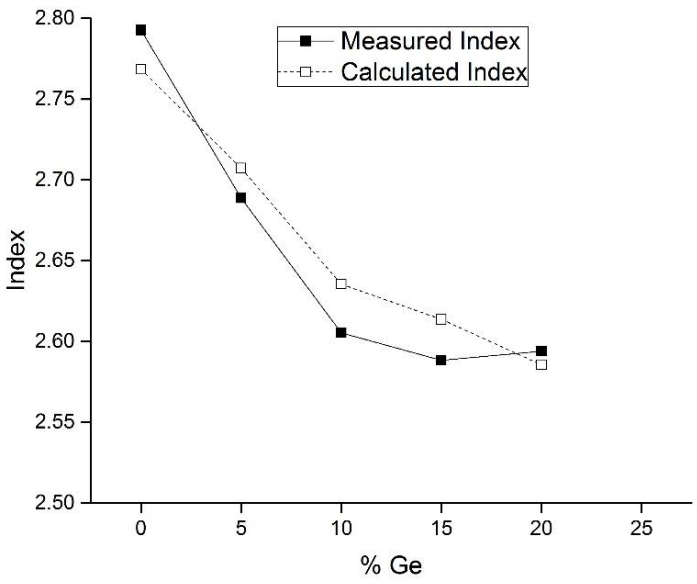

Figure 4.43 – Measured refractive index values along with index values calculated from the Lorentz-Lorenz formulation.

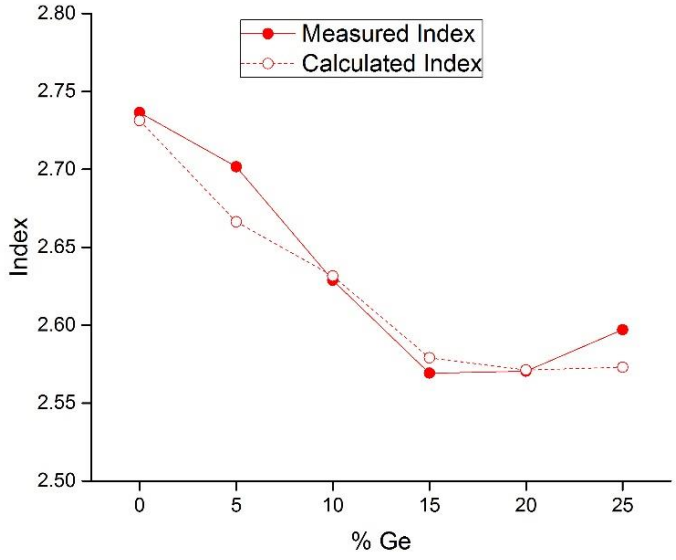

Figure 4.44 – Measured refractive index values along with index values calculated from the Lorentz-Lorenz formulation.

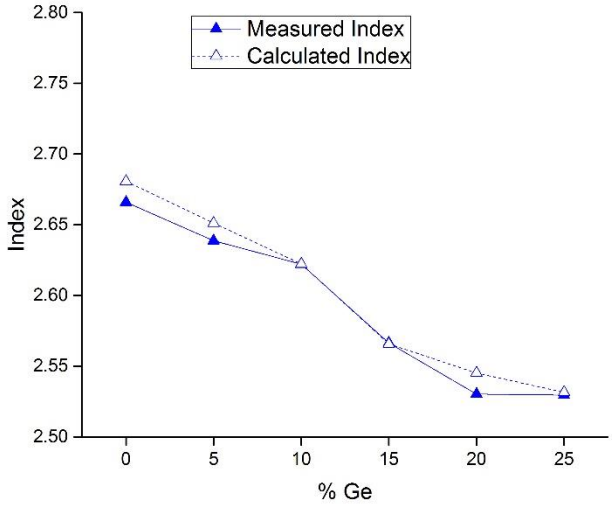

Figure 4.45 – Measured refractive index values along with index values calculated from the Lorentz-Lorenz formulation.

4.9.3 Thermo-optic coefficient (dn/dT)

Similar to the refractive index, the thermo-optic coefficient for the three tielines is presented in Figure 4.46a as a function of the MCN. Also similar to the refractive index, the dn/dT can be separated into three zones of common trends. The $(As_{.35}Se_{.65})_{100-x}Ge_x$ and $(As_{.30}Se_{.70})_{100-x}Ge_x$ tielines each show an increasing dn/dT until an MCN of ~2.45, then all three tielines exhibit a plateau between ~2.4-2.6, and then finally the dn/dT increases when MCN is greater than 2.6. The dn/dT is also shown in Figure 4.46b as a function of the Se-rich/-poor%.

In the case of the Se-rich/-poor%, the transitions between the zones are more pronounced than the MCN case, and correspond to the locations of the trend shifts observed in the refractive index. Specifically, the dn/dT changes linearly when the network is between

+30% and 0% Se-rich until compositions reach stoichiometry, the dn/dT then experiences a plateau while the network is between 0 and -20% Se-poor, and finally a second trend is observed when the network is between -20% and -30% Se-poor, the point at which Ge-Se ethane-like modes are expected to appear in the network. Inflections in dn/dT are linked with changes in structure signifying that the dn/dT also has a strong dependence on the structures present in the network.

Neither the index nor the thermo-optic coefficient show clear, predictable trends at the key MCN values of 2.4 or 2.67, as has been predicted through constraint and topology arguments. Instead, viewing the changes in index and thermo-optic coefficient with respect to how Se-rich or how Se-poor the network is, and thus which structures are likely to be present in the network, gives a more complete idea of how compositional variations will affect optical properties.

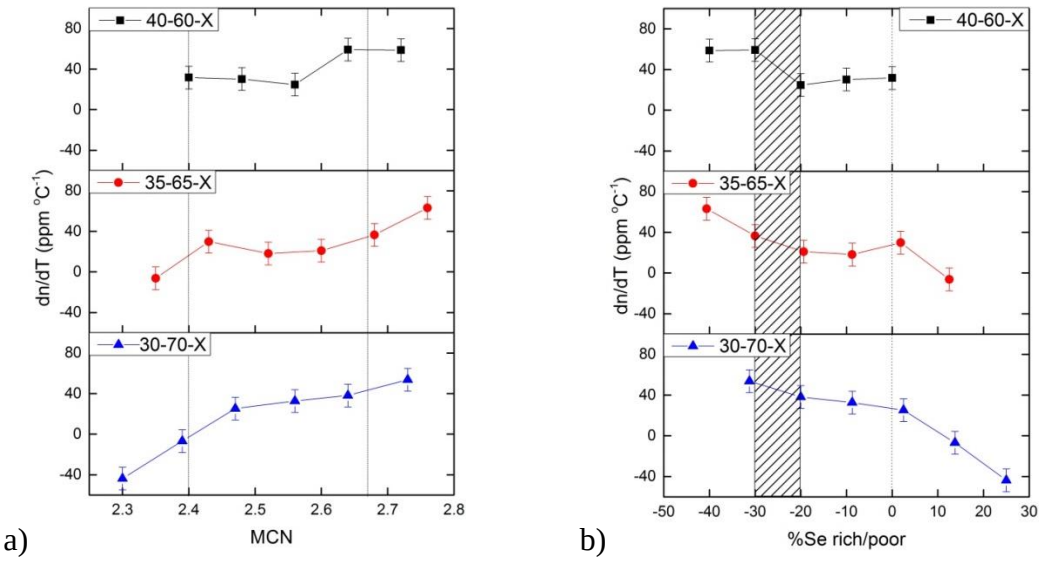

Figure 4.46 – Thermo-optic coefficient of the three GeAsSe tielines as a function a) MCN and b) %Se rich/poor. Vertical lines and shaded regions are shown to highlight locations of theorized transitions along the tielines.

4.9.4 Thermal Lorentz-Lorenz models

The primary formulation for modeling the change in the refractive index with temperature comes from a derivation of the LL model with respect to temperature, first presented by Prod'homme [146]:

$$\frac{dn}{dT} = \frac{(n^2-1)(n^2+2)}{6n}(\varphi - \beta)$$

Equation 12

where ϕ is related to the thermal polarization coefficient and β is related to the thermal expansion coefficient. This equation presents the thermo-optic coefficient as a competition between volumetric expansions with temperature (which lowers the index) and an increase in the electronic polarization of the atoms with temperature (which increases the index). Hilton [36,147] further simplified this relation by noting that the index ratio can approximated as n^3. His adaptation of the equation becomes:

$$\frac{1}{n^3}\frac{dn}{dT} = \frac{1}{6}\left(\frac{1}{R_m}\frac{dR_m}{dT} - 3CTE\right)$$

Equation 13

Using this Hilton approximation, the thermal polarizability coefficients (dR_m/dT) of each glass was calculated. Trends in dR_m/dT show a general decrease in the thermal polarizability coefficient with Ge content (or Se-deficiency), but vary too much to draw additional conclusions. Extrapolating the thermal polarizability coefficients across the tielines can theoretically yield thermal polarizability coefficients for the individual element, but the model results in a poor fitting. The fact that the LL model does not

accurately allow for bond or structure contributions carries forward as its temperature derivations also lack a contribution from these effects.

Plotting the quantity (n^{-3}·dn/dT) against the CTE yields a marginal linear relation (r^2 = 0.84) and is shown in Figure 4.47. A similar linear fitting was unable to be obtained for the dn/dT versus dR_m/dT data as there was too much variability in the calculated values. The linear relation between the two products indicates that knowing the both the coefficient of thermal expansion and refractive index is sufficient in reasonably predicting the dn/dT of a novel chalcogenide glass.

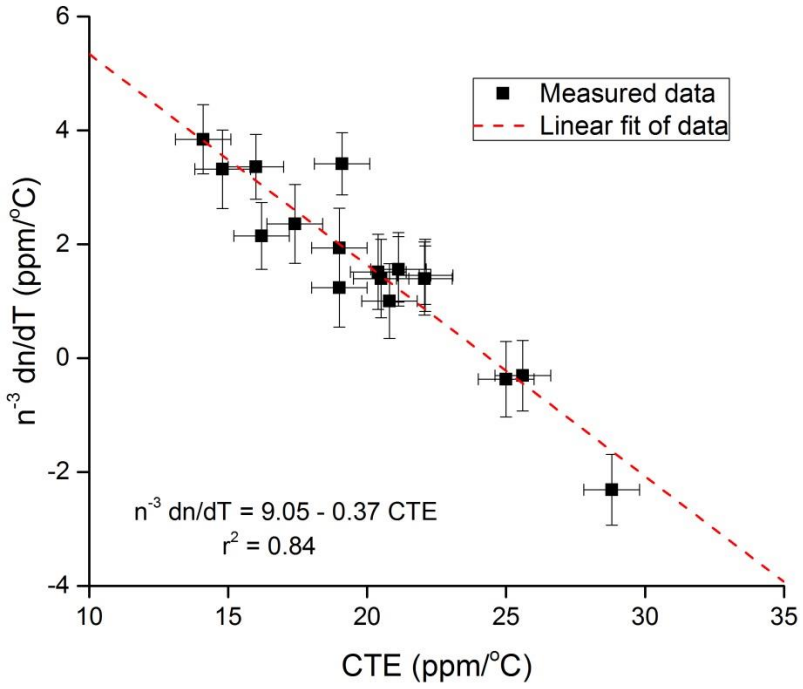

Figure 4.47 – Correlation between the quantity (n^{-3}·dn/dT) and the coefficient of thermal expansion, with a linear fitting

Solving the linear fit between (n^{-3}·dn/dT) and CTE for the zero dn/dT case give a solution of CTE = 24.5 ppm·°C^{-1}. Substituting this value into Equation 7, and taking into account

error from the dn/dT and CTE, yields an approximate MCN range of 2.3-2.4 that should provide the necessary CTE to produce a zero dn/dT. This range of binary and ternary glasses should provide IR optical designers with a starting point to develop novel compositions with a low or zero dn/dT.

Figure 4.47 was recreated to include various commercial infrared and oxide (visible) materials [2], and is shown in Figure 48. Most infrared materials fall along the best fit line between (n^{-3}·dndT) and CTE. The only significant exception is crystalline Silicon, with an extremely low coefficient of thermal expansion relative to its dn/dT. Oxide glasses completely miss this line, suggesting that separate fittings may be required for separate material types.

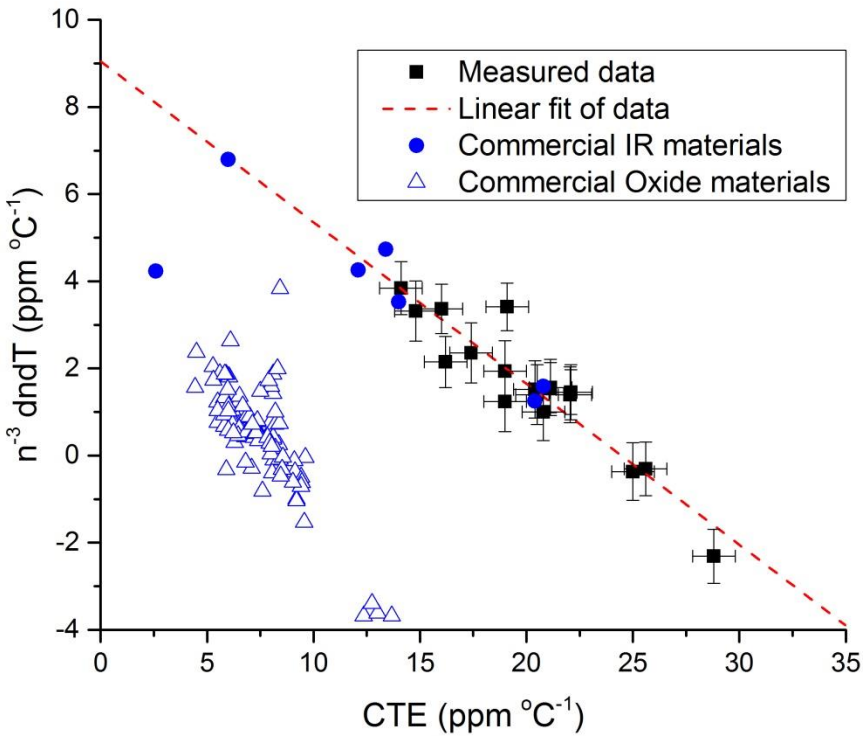

Figure 48 – Correlation between the quantity (n^{-3}·dn/dT) and the coefficient of thermal expansion for measured glasses, commercial infrared materials, and commercial oxide materials.

The knowledge of other chalcogenide glasses fitting the linear relation between (n^{-3}·dndT) and CTE will allow for prediction of zero dn/dT compositions in other glass forming systems. For example in the GeSbSe system, where Sb acts an iso-structural substitute for As, we can utilize CTE values obtained from SciGlass [148-151] to predict what compositions should give a zero dn/dT. Unfortunately, there is less data available for the GeSbSe ternary glass forming system, than the GeAsSe glass forming system. Despite the limited dataset, the CTE GeSbSe of glasses appear to follow a similar exponential-like relationship with the MCN as seen in GeAsSe glasses. Therefore, it is estimated that a GeSbSe glass with a MCN of approximately 2.35 – 2.45 will produce the necessary CTE to result in a zero dn/dT.

4.10 Conclusions

This chapter discussed two of the most important aspects of this dissertation: construction and characterization of an infrared (IR) index metrology tool, and the subsequent characterization/analysis of GeAsSe refractive index and thermo-optic coefficient (dn/dT).

The unique index metrology system was created through significantly modifying an off the shelf Metricon prism coupler to operate in the IR. Two versions of this system were created, one at Pacific Northwest National Laboratory (PNNL) and the other at University of Central Florida (UCF). Thermal and index calibration was performed on both system prior to measurements. Measurements of the refractive index on GeAsSe glasses conducted on both systems showed good agreement with minimal offset, while dn/dT measurement showed a significant offset between the two systems.

To address the issue of the material homogeneity, this chapter showed minimal variation of optical properties (index dn/dT) within a single melt as well as from melt-to-melt. The chapter also showed a larger inhomogeneity for "large-melt" samples, but demonstrated the ability to reduce this inhomogeneity with subsequent annealing steps, signifying that the index variations are mostly due to thermal history variations in larger melts.

The index and dn/dT results and analysis presented in this chapter constitute the main contribution for this body of work. Index metrology results showed an overall decrease in the index with Ge additions. Along each of the tielines investigated significant shifts in trends were observed at compositions corresponding to a change in the structure present in the glass. The first shift in trends was found to occur at compositions that are chemically stoichiometric: neither a net Se-excess nor a Se-deficiency. Se-Se bonds are only found in compositions with a Se-excess, but disappear once the composition becomes Se-deficiency resulting in the formations of As-As bonds. The second transition resulted in a minimum in refractive index and was found to occur at composition corresponding to the creation Ge-Se ethane-like structures, which only occur at higher levels of Se-deficiency.

The compositional trends for the dn/dT were also linked to the same structural changes as observed in the index within the analysis of this chapter. The dn/dT was shown to increase rapidly with added Ge up until the composition reached stoichiometry. As the structures within the network changed the dn/dT was shown to nearly plateau with further compositional changes. At the composition corresponding to the creation of Ge-Se ethane-like structures, the dn/dT was shown to increase again.

A method of predicting the index using the Lorentz-Lorenz model was outlined through combining density data and fitted refractivity values for Ge, As, and Se. This method of predicting the index found to be appropriate for first order approximations of the index as it did not have ability to take into account the contributions from structures in a glass, but rather only considered the individual elements in the composition. A simplified version of the thermal derivations of the Lorentz-Lorenz model also demonstrated a strong linear relationship between the quantity ($n^{-3} \cdot dn/dT$) and the coefficient of thermal expansion (CTE), demonstrating that the dn/dT can be roughly assumed knowing only the CTE and the refractive index.

Chapter 5

Room Temperature Index Relaxations

This chapter discusses a series of experiments that resulted after a sample exhibited a sharp change in refractive index with temperature during dn/dT measurements. The motivation for this chapter was to characterize and understand this phenomenon in chalcogenide glasses, how such an effect impacts the quality of measurements made (by our group and others), and to determine which compositions in the present effort might exhibit this feature. While this phenomenon was not initially planned as part of the investigation of this dissertation, it is vital to understand for any composition that may be a candidate for commercial production or detailed laboratory analysis.

The chapter will first present a brief background to aid in the understanding of structural relaxations in chalcogenide glasses. This includes prior observations of index drop seen in analysis of ChGs such as those studied, widely used in the precision glass molding community [110,152]. The index drop and subsequent room temperature relaxation on a sample of commercial glass IG 6 is then presented for two different thermal conditions, highlighting the similarities between the two. The process is then repeated on a Se-excessive glass, highlighting the role of the network structure in this phenomenon.

The relaxations of both of these glasses will be fit with simple relaxation equations, in order to compare their relaxation times (τ) with the processes described in literature.

5.1 Background – Structural Relaxations

Structural relaxations occur within a glass when it is in a state of thermodynamic dis-equilibrium. This dis-equilibrium is most prevalent as a molten glass cools through the glass transition region, where the kinetics and thermodynamics are changing rapidly. The kinetics eventually slow relaxations enough to prevent the glass reaching a certain thermodynamic equilibrium before that equilibrium has changed, creating a deviation between the current thermodynamic state of the glass and the equilibrium state. The faster a glass is cooled through the T_g region, the more severe the deviation from equilibrium will be. Normally a glass will next be annealed isothermally at 40 °C below the T_g for several hours to several days or weeks. During the annealing step the kinetics are sufficient enough to allow relaxations within the glass so that the glass can approach the thermodynamic equilibrium state. The larger the difference between the isothermal holding temperature (either in annealing or storage) and the T_g a glass is, the longer it is expected for that glass to reach thermodynamic equilibrium, if they will reach at all.

Structural relaxations have been observed in several types of glasses including oxides and chalcogenides [1,118,121,153-156]. In the chalcogenide glass family, glasses with excessive chalcogen content and a loosely bound network experience a larger effect from structural relaxations. In amorphous Se, which is essentially a 2D network, the structural relaxations are caused by compression of Se chains, and the Se switching between ring and chain configurations [153,155-161]. As the composition becomes less chalcogen excessive and the amount of Se chains are reduced, the network experiences a lesser degree of structural relaxations.

Structural relaxations within a glass can be characterized by a series of weighted exponential growth/decay functions, as shown in Equation 14. In this equation A is a fitting parameter, τi are the relaxation times, and Bi are weighting terms used to signify the strength of each relaxation. For simple relaxations, only one exponential may be needed, whereas complex relaxations may need several weighted exponentials to fully describe the relaxation.

$$y = A + \Sigma_i B_i * e^{-\frac{t}{\tau_i}}$$

Equation 14

Work by Koontz characterized the time scale of relaxations in (Ge)AsSe chalcogenide glasses as a function the difference between the isothermal hold temperature and the respective T_g, in the range of normal annealing temperatures using length dilatometery methods. This work showed that close to T_g the longest relaxations times are on the order of 10s of seconds, and decreasing the isothermal hold temperature relative to T_g will increase the longest relaxation times by three orders of magnitude, or a value of ~ 10,000s.

Work on GeSe binary glasses by Bhosle et al. also studied the effect of ageing near T_g, and found a series of compositions along the binary which exhibited no ageing effects [162,163]. This region of compositions has been described in this binary tieline and within other ternary glass forming systems as the "Boolchand intermediate phase", and is a region in which glasses exhibit a zero non-reversible heat flow in modulated DSC experiments. The work performed by Bhosle et al. did not specifically investigate the shape of the

relaxation “curves” but rather stated which sample did and did not experience ageing effects.

Room temperature relaxations have also been observed in binary glasses AsSe with a Se content > 60 at% [121,153-156,161]. Golovchak et al. observed volumetric relaxations of $As_{20}Se_{80}$ and $As_{30}Se_{70}$ glasses stored at room temperature for 20+ years using calorimetric methods. The authors ascribed a $\tau \approx 20$ years or ~600,000,000 seconds to these relaxations. The authors described the processes as a physical ageing that is driven by volumetric contractions of Se-Se-Se polymeric chains, and noted that these relaxations take place “much more effectively at high temperatures” [155]. The range of compositions likely to undergo a long-term densification includes all Ge- and/or As-Se compositions with a Se-rich network. The formulation presented by Golovchak does not expressly allow for room temperature relaxations in stoichiometric $As_{40}Se_{60}$, but work by others has shown the presence of a non-zero amount of homopolar bonds present in stoichiometric (Ge)AsSe glasses [63,70], allowing for the formation of Se chains and thus potential long term ageing.

Combining the results of Koontz and Golovchak, it becomes clear that the further away from T_g a glass is isothermally held, the longer the relaxation time, or τ, needed for the glass to fully relax to the equilibrium, ranging from tens of seconds near T_g to hundreds of millions of seconds at room temperature.

Hence, the importance of this effect on manufacturing of chalcogenides in bulk optical applications is significant, as variation in thermal history impacts bulk structure which affects resulting properties [110,152]. Specifically, thermal history induced index changes

can impact the actual refractive index, dispersion and thermo optic coefficients used by optical designers for modeling performance. Thus the role of considering the contributions of relaxation effects in measurement of these properties (for commercial and lab-scale investigations) is appropriate.

5.2 Effect of Relaxation of GeAsSe Glass Structures

Several of the GeAsSe glass samples investigated in the present study exhibited a non-linear change in refractive index with temperature. Specifically, as certain samples were heated to the temperature set points of 30 °C, 50 °C, and 70 °C the measured refractive index would linearly change with temperature. Upon heating to the final temperature set point of 90 °C, the slope between the 70 °C and 90 °C set points was significantly different than between the other set points. An example of this is shown in Figure 5.1, for the composition 30_70_5, where and inflection can be seen at the 70 °C set point. The total time at the maximum temperature of 90 °C was approximately one hour.

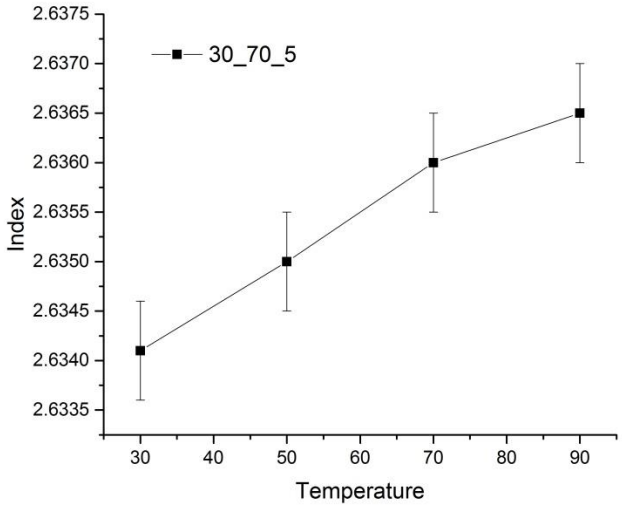

Figure 5.1 – Measured Index vs. Temperature for the 30_70_5 sample as initially measured at PNNL

It was also observed that upon cooling the sample to 70 °C, 50 °C, or 30 °C the newly measured index was lower than the initial measurements. This "index drop" occurred as a result of heating the sample to 90 °C during measurements. Given that the glass transition temperature (T_g) of all of these glasses is greater than 90 °C, this observation is therefore referred to as a "sub-T_g index change". After the sub-T_g index change occurs in the sample at 90 °C, the change in measured refractive index with temperature is again linear. The refractive index for the complete thermal cycle for the 30_70_5 sample is shown in Figure 5.2. The black data points represent the index before the sub-T_g relaxations have occurred, and the red data points represent the index after the glass has partially relaxed at 90 °C.

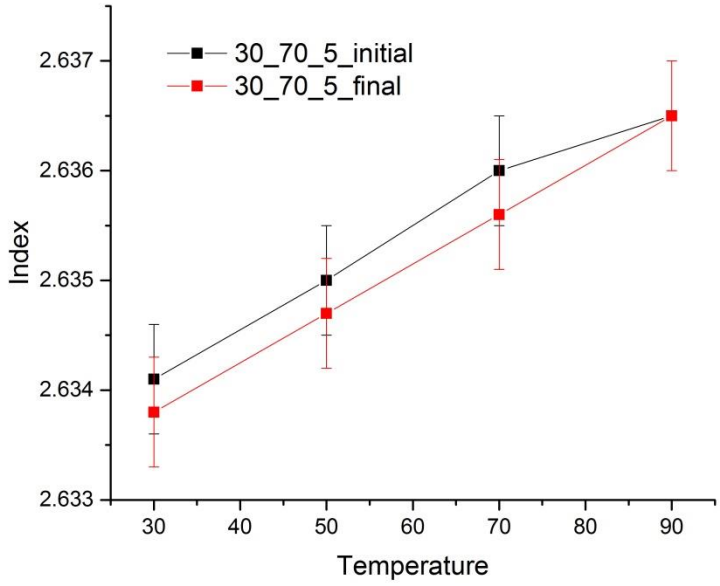

Figure 5.2 – Refractive index vs. Temperature for the 30_70_5 sample, showing the "sub-T_g index relaxation" at 90 °C, and the index drop at additional lower temperatures

This effect was first observed in August 2014 on several GeAsSe samples investigated here, while conducting measurements at PNNL. In years prior to this observation, the index of all samples was only measured at 30 °C and 90 °C due to time constraints and was fully not observed. Measuring the sample in this manner masked the effects of the sub-T_g index relaxations. The samples sat at room temperature under ambient conditions (standard pressure, and shielded from illumination) for approximately one year at the time of the first observation in August 2014. The average change in index at 30 °C across all measured samples after thermally cycling up to a maximum temperature of 90 °C is listed in Table 5.1 for each of the compositions investigated. If the average index change for a composition was less than the measurement error, ± 0.0003, the index change is listed as zero but is also noted with an asterisk.

After the construction of the Metricon system in the UCF laboratories, the same samples were re-measured using the same protocol to try to replicate the observed index drop at PNNL. The observed change in index measured at UCF at 30 °C is also shown in Table 5.1 for comparison. The time between measurements at PNNL and UCF was approximately 7 months.

Table 5.1 – Average measured change in index at 30 °C for all compositions at PNNL (small melts only) and at UCF (both small and large melts), approximately 7 months later. Compositions which exhibited a change in index less than the error, ±0.0003, are listed as zero index change and also noted with an asterisk.

Glass Composition	Index drop at PNNL	Index drop at UCF (Small melt)	Index drop at UCF (Large melt)
40_60_0	0.0004	0.0007	X
40_60_5	0.0005	0.0005	X
40_60_10	0.0000	0.0000*	0.0004
40_60_15	0.0000	0.0000*	X
40_60_20	0.0000	0.0000	0.0000
35_65_0	0.0010	0.0005	X
35_65_5	0.0004	0.0003	X
35_65_10	0.0000*	0.0000*	0.0000
35_65_15	0.0000	0.0000*	X
35_65_20	0.0000	0.0005	0.0000
35_65_25	0.0000	0.0000*	X
30_70_0	0.0016	0.00020	X
30_70_5	0.0004	0.0005	X
30_70_10	0.0003	0.0004	X
30_70_15	0.0000*	0.0000*	X
30_70_20	0.0000	0.0000*	X
30_70_25	0.0000	0.0000*	X

In general, the compositions with a Se-rich network exhibit a change in index at 30 °C, and glasses with a larger Se-rich%, such as 30_70_0 ($As_{30}Se_{70}$), exhibit the *largest* change (drop) in index. The exceptions to this are 40_60_0, which is stoichiometric. Note that 40_60_10 only exhibited an index drop in the large melt, and 35_65_20, which is Se-poor and only exhibited an index drop at UCF. As discussed in Section 4.8.4, the 40_60_10

large melt sample exhibited a change in index after a secondary annealing step suggesting that the glass was not fully annealed, and is also thought to be a contributing factor to the observed "index drop". Aside from these two outliers (40_60_10 and 35_65_20), it is believed that the observed index drop is primarily limited to compositions with a stoichiometric or Se-rich network. Additional work will be needed to confirm the boundaries of this phenomenon. Overall, there was good agreement between the measured index drop at PNNL and that (re-measured) at UCF.

The act of heating the sample up to 90 °C for ~ 1 hour is enough to cause a slight change in the glass' thermal history, and shifts the network to a slight disequilibrium state. The approximate 7 month gap between thermal cycling at PNNL and at UCF was enough time such that the room temperature relaxations could return the glass to the original equilibrium state. The next task was to determine exactly how the refractive index responds to the structural relaxations at room temperature, and to see if they can be characterized in similar methods to Golovchak and Koontz.

5.3 Analysis of commercial sample: IG6

Using the same experimental method as described previously in this Chapter, a sample of commercial glass, IG 6 from Vitron [35] was measured to include as a reference material with published index data. It was found to also exhibit a negative Δn, an index drop, at 30 °C after cycling to a maximum temperature of 90 °C. As discussed in Section 4.5.2, the sample of IG6 measures approximately 25mm x 25mm x 3mm and the refractive index was measured at 30 °C on a near-daily basis. Additionally, the sample was occasionally

thermally cycled up to 90 °C for dn/dT measurements. A representative refractive index profile of the IG6 sample before and after thermal cycling at 90 °C is shown in Figure 5.3. As with the (Ge)AsSe samples described previously, the samples was at 90 °C for approximately one hour. The initial Δn for the IG6 sample after thermal cycling was 0.0008 ±0.0003.

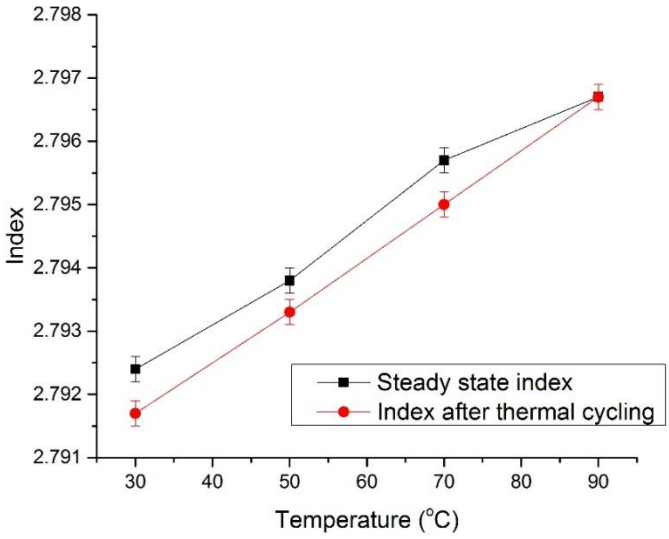

Figure 5.3 – Refractive index of IG6 both before and after thermal cycling up to 90 °C.

After this cycle the sample was stored at room-temperature (~20-24 °C) and measured at 30 °C on the semi-daily basis. Over the course of the next several days, the measured index at 30 °C slowly reverted to the initial (or steady state) index. This process is shown in Figure 5.4, which shows the measured index as a function of the time left at room temperature, as measured in seconds.

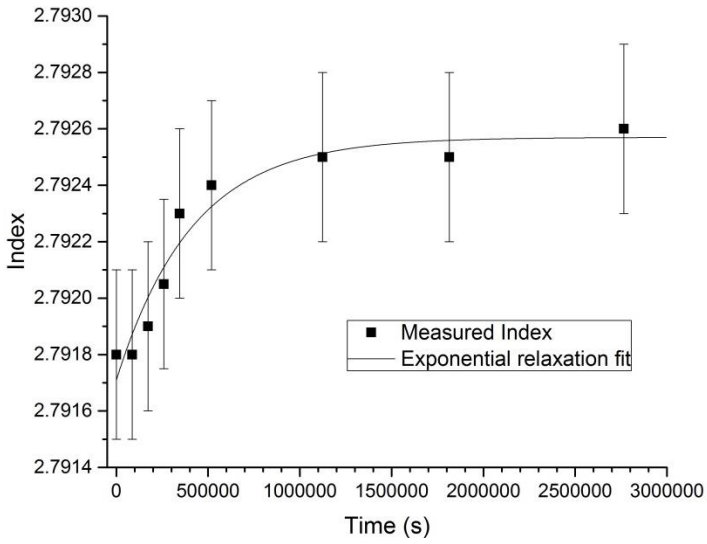

Figure 5.4 – Refractive index recovery of IG 6 sample at 30 °C after being held at 90 °C for 1 hour during measurement.

The same IG 6 sample was then placed in an annealing furnace at 90 °C for 6 days, to investigate if prolonged exposure to the "soft-anneal" temperature would measurably alter the recovery of the refractive index as it was subsequently held at room temperature. The sample was again measured once daily over the course of several days to determine the room temperature recovery/relaxation profile. The refractive index recovery for this experiment is shown in Figure 5.5, as a function of the time at room temperature, in seconds.

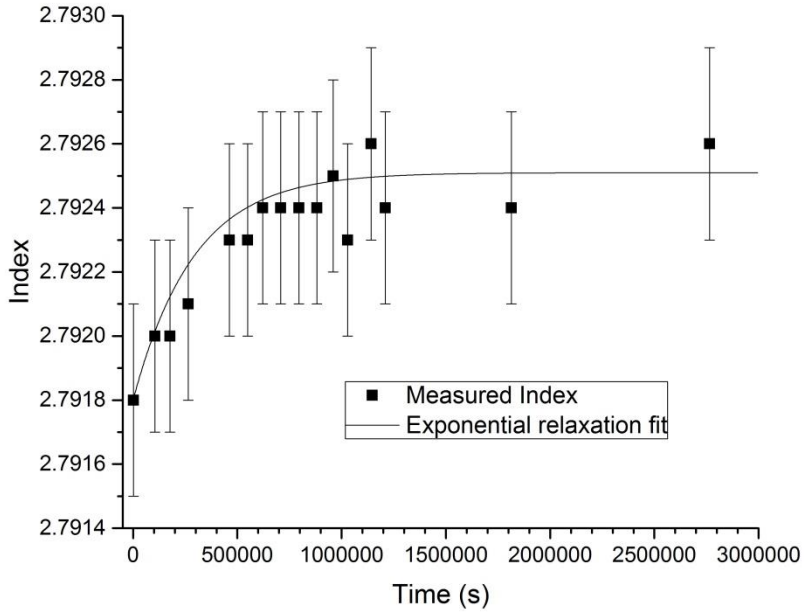

Figure 5.5 – Refractive index recovery of IG 6 sample at 30 °C after being held in an annealing furnace at 90 °C for 6 days.

Initial observations showed that indeed the behavior of the "index recovery" process is extremely similar to volumetric relaxations observed in chalcogenide glasses and explained in detail by Koontz [1] and Golovchak [155,156,161]. As noted, the recovery was related to the new thermal history, and not the long-standing prior manufacturing process' thermal history.

The index recovery data for each data set was then fit with a single exponential growth as shown in Equation 14. Fitting the initial data set, ~1 hour at 90 °C, to the exponential growth equation yielded a reasonable fit, with a relaxation time, τ = 287,000 seconds and an r^2 = 0.92. The second data set, in which the IG6 sample was held for 6 days at 90 °C, resulted in a relaxation time of τ = 291,500 seconds and an r^2 = 0.88. There is essentially

no change in the relaxation times for these two experiments, signifying that one hour at 90 °C is enough time to completely, but temporarily, alter the thermal history of the IG6 sample enough to impart temporary changes in the index.

These two relaxation times are simultaneously much longer than relaxation times observed by Koontz [1,118], and much shorter than the relaxation times observed by Golovchak [155,156,161] for AsSe binary glasses with similar compositions. It is difficult to ascertain the reasoning the vast discrepancies between this result and the two external results, but it is extremely important to note that all three of the experiments are measuring relaxations using different techniques. Koontz obtained results through dilatometric measurements, Golovchak through calorimetric measurements, and results in this work were obtained through optical measurements. It is hypothesized that the (time-) scale length of the various measurement techniques may play a role in capturing the structure-sensitive attributes of the thermal history modified material and thus impacts the magnitude of the calculated relaxation times. This mechanism, while similar in structural origin is perhaps sensitive to the physical attribute being probed in the specific characterization method employed to observe the property change. Further experiments to systematically characterize the changes, with time and temperature, would provide further guidance on these hypotheses.

5.4 Analysis of Se-rich Sample: $As_{30}Se_{70}$

A sample of the composition 30_70_0 was also subjected to the same measurement protocol to determine how increasing the amount of Se-chains would affect the relaxation times. As listed in Table 5.1, the 30_70_0 sample exhibited the largest change in index at

30 °C after thermally cycling to a maximum temperature of 90 °C. The refractive index recovery of the 30_70_0 sample is shown in Figure 5.6. The measured index was fit with Equation 14, which resulted in a relaxation τ = 67,000 s and an r^2 = 0.95. The relaxation time of the 30_70_0 ($As_{30}Se_{70}$) sample is significantly faster than that of the IG6 sample ($As_{40}Se_{60}$), by almost an order of magnitude. According to Golovchak, densification of the Se-chains are the driving for in this relaxation, and so it would logically follow that increasing the Se-chain concentration in a glassy network should cause larger total relaxations and also decrease time necessary to complete these relaxations.

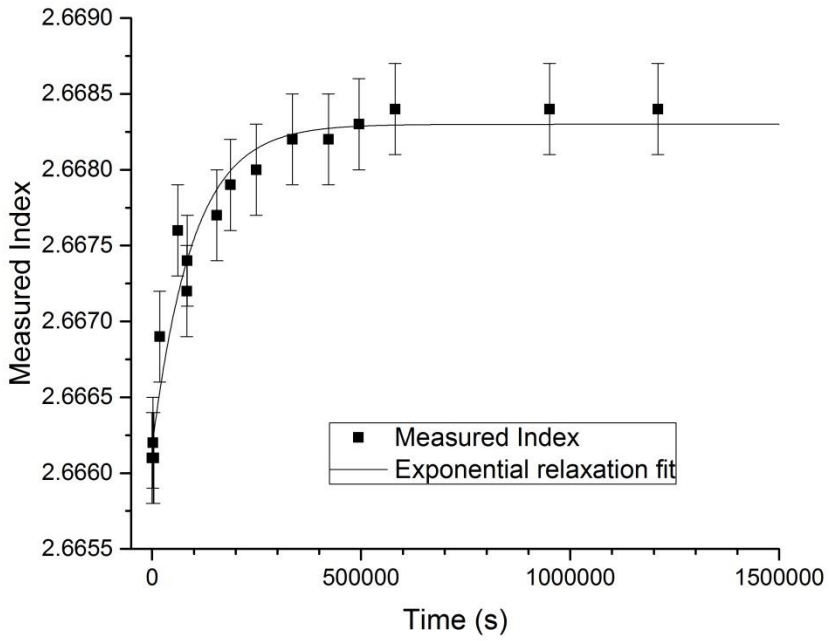

Figure 5.6 – Refractive index recovery of $As_{30}Se_{70}$ at 30 °C after being held in an annealing furnace at 90 °C for 1 hour during measurement.

5.5 Conclusions

This chapter has described a new phenomenon in chalcogenide glasses that has not been previously discussed in literature. While this work was not specifically designed to answer the fundamental questions of this dissertation, it was still deemed important to understand in the broad scope of chalcogenide optical properties and compositional design.

Specifically this chapter has shown a drop in the refractive index after thermal cycling, and a subsequent recovery in the index while being held at room temperature for several days. The cause of the index drop is a "freezing-in" of a new, non-equilibrium, thermo-dynamic state. Over time the glassy structure returns to the initial equilibrium structure, demonstrating a "memory" of that thermodynamic state.

The chapter quantified the index drop magnitude and recovery times for two AsSe binary glasses, and demonstrated that glasses with a Se-excessive network simultaneously have a larger index drop and faster recovery to a stoichiometric glass. Additional experiments noted that one hour at the elevated temperature was sufficient to fully, but temporarily impart the index drop.

Other relaxation phenomena have been documented in chalcogenide glasses with both shorter and longer time scales. This work is intended primarily to document this phenomenon, as there is still a significant amount of work required to fully characterize the origins and determine if the relaxations seen here are indeed the same structural relaxations as described by other authors.

Chapter 6

Conclusions

Currently, the development of novel infrared (IR) optical systems is hindered by the lack of a wide variety of available IR materials. IR optical designers are limited to only a handful of IR crystals and glassy materials. The overall goal for this dissertation was to alleviate the stresses of this situation through developing a method to compositionally design optical properties in chalcogenide glasses. These novel glasses will be designed to meet specific property attributes and therefore able to fulfill specific roles in an IR imaging system. This dissertation has chosen to focus on the GeAsSe ternary glass-forming system to work toward this goal.

In order to achieve this goal, two main tasks were identified. First it was realized that in order to characterize the optical properties (index and thermo-optic coefficient or dn/dT) of IR glasses, novel metrology equipment would need to be designed, constructed, and characterized. To accomplish this goal, several modifications were made to an "off the shelf" prism coupler from Metricon Corporation that allowed the system to measure index and dn/dT in the IR. Initial modifications were performed at Pacific Northwest National Laboratory (PNNL), and a mirror system was constructed at University of Central Florida (UCF). Error analysis of these systems revealed an *absolute* error on the index of ± 0.0005 and ± 11.2 ppm·°C^{-1} on the dn/dT, and outlined methods to decrease the error on the dn/dT to under ± 5.0 ppm·°C^{-1}. Repeatability experiments using the UCF system on a commercial

sample of IG 6 from Vitron showed a *relative* error on the refractive index and thermo-optic coefficient of ±0.0003 and ±6.0 ppm·°C^{-1}, respectively.

The second task to accomplish the overreaching goal of this dissertation was to melt and fabricate several chalcogenide glasses with unique compositions, then characterize the optical and non-optical properties of these glasses, and finally present the collected data in a manner that allows for meaningful analysis. This was by far the larger of the two tasks and resulted in a significant amount of data to be collected and analyzed.

To accomplish this task, this work investigated the effects of adding Ge to three binary AsSe glasses, up to a maximum of 25 at % Ge, creating a total of 17 unique GeAsSe compositions. The structural, optical, and physical properties of each composition was measured and presented as a function of either the chemistry (composition), network connectivity (mean coordination number), or the inherent structural makeup of the network (Se excess or deficiency). These multiple data types and presentation methods form the basis for compositional design analysis and allow for the answering of several fundamental questions needed to address the overall goal of this dissertation.

For example, one of the fundamental questions of this work was related the unknown effects of compositional design to the properties relevant to the manufacturing process. This study defined the material properties that dictate how a glass will respond to state of the art manufacturing processes and found that adding Ge increases the glass transition temperature (T_g), Vickers hardness (H_v), and decreases the coefficient of thermal expansion (CTE), all of which lead to a glass that is easier to manufacture into lens geometries through

conventional methods (grinding and polishing or diamond turning). This study also described the driving force behind these non-optical property changes as being the cross linking of AsSe puckered layers by Ge-Se bonds, which strengthens the network by replacing weak van der Waals forces with strong covalent bonds.

Combining the optical data with structural information obtained both here and from prior literature led to new understanding to the posed question regarding the origins of variations in the index and dn/dT with composition. The results and analysis presented here showed a strong shift in index and dn/dT trends at compositions corresponding to appearance or disappearance of specific structures. The first transition along the tielines was found at the stoichiometric composition, which resulted in a sharp change in slope for the index and a pseudo-plateau for dn/dT. On the Se-rich side of stoichiometry, Se forms homopolar bonds with itself, while on the Se-poor side As forms homopolar bonds with itself. The second transition along the tielines was found at a composition corresponding to a high level of Se deficiency that leads to the formation of $Ge_2Se_{6/2}$ ethane-like modes. This transition resulted in a minimum in the index, and the end of the pseudo-plateau region of the dn/dT.

Fitting the refractive index with the classical Lorentz-Lorenz model allowed for calculation of the polarizability of the individual constituents, and a reasonable prediction of the refractive index for a novel composition. Derivation of the L-L model with respect to temperature yields the Prod'homme equation, which relates the thermo-optic coefficient to the thermal expansion coefficient (CTE) and the thermal polarizability coefficient. Further simplification showed a linear relationship between the CTE and the quantity ($n^{-3}\cdot dn/dT$). This simplification revealed that in order to reasonably predict the thermo-optic coefficient,

only the room temperature index and the CTE are needed. Additionally, if a system calls for a novel composition with a zero thermo-optic coefficient, this simplification reveals that only the CTE is necessary in finding a suitable composition. The refractive index will not play a significant role in determination of the thermo-optic coefficient, and therefore several novel compositions, each with unique index values, can all have a zero thermo-optic coefficient.

The modeling of the index and dn/dT addresses the two remaining questions proposed at the start of this work: is there a link between optical and non-optical properties that can be used to reasonably predict index and dn/dT without necessarily measuring them, and are the other compositions which may satisfy the unique requirement of a zero dn/dT that simultaneously have better thermo-mechanical stability to commercially available options?

During measurements of the thermo-optic coefficient several samples exhibited hysteresis in the index at higher temperatures. This phenomenon was unexpected and certainly not part of the initial scope of this project. However it was decided that this observation deserved to be fully fleshed out in order to understand the ramifications of thermally-induced sub-T_g index modifications.

The initial index values at 30 °C were found to drop after cycling the sample to a maximum of 90 °C. This "index drop" was observed primarily in samples with a Se-rich composition, but not exclusively. One sample of IG6 ($As_{40}Se_{60}$) was then measured on a daily basis, and exhibited relaxations at room temperature, causing the index to slowly recover to the initial value. This "room temperature index recovery" took place over the course of 14 days, and

had a characteristic relaxation $\tau \cong 290{,}000$ s. The relaxation time was found to not shift significantly even when the sample was held at 90 °C for 6 days, signifying that 1 hour at °C is sufficient time to completely, but temporarily, alter the refractive index.

A sample of $As_{30}Se_{70}$ was also subjected to the same thermal cycling and measurement protocol. Like the IG 6 sample, the $As_{30}Se_{70}$ sample exhibited a recovery of the refractive index over the course of several days. The magnitude of change in the index for this sample was much larger (~0.0024 compared to 0.0008) and the relaxation time for the recovery of this sample was much shorter (~50,000s compared to ~290,000s). Both glass manufacturers and optical designers need to understand this phenomenon to ensure optical performance of the glass meets operation standards and requirements. There is significant room for further research in this area as this phenomenon has not been documented before.

The work and analysis presented here has addressed the required tasks and fundamental questions required to develop a method to compositionally design optical properties in chalcogenide glasses. It is believed that this work can serve as a good basis for the beginnings of compositional design for other unique optical property requirements, and also be extended into other glass forming systems with similarly understudied interrelationships between optical and material properties.

APPENDICES

APPENDIX – A

This section describes the standard operating procedure (S.O.P.) for measuring the refractive index of a sample on the Metricon Prism Coupler. The S.O.P. has been separated into four main tasks: system check, source check, calibration, and measurements.

1. System Check

Before using the Metricon Prism Coupler (Metricon), the user must first inspect the functionality of the system and its individual parts. The list of parts and functions to investigate has been separated into four categories: optical, mechanical, sources, and electrical.

Optical

- Mirrors
- Apertures
- Power meter / quadrant detector

Mechanical

- Pneumatic actuator
- Steering mirrors (tip/tilt dials)
- Rotation stage

.Sources

- See source check

Electrical

- Detector detects
- Lock-in locks-in
- Signal generator generates a signal

2. Source Check

This section will describe the proper procedure for turning on illumination sources for measurement purposes. At the time of writing the S.O.P. the only available sources are two optical parametric oscillators (OPOs) from M^2 Lasers Inc. and the procedure will describe the procedures for these specific sources. First turn on the power the all four of the control boxes for the M^2 lasers using the provided turn-keys. Allow the lasers approximately 5 minutes to reach their steady-state operating temperature.

Open the Google Chrome browser on laptop computer connected to the four control boxes. The default home page will bring you to a page which will control laser operation. Click on the "Control" button at the top of the page. Enter the username "main" and the password "main". Choose the wavelength of operation from the list provided, or input a new wavelength. Press the "Select" button next to the wavelength of choice. Allow time for the laser to reach this wavelength set point if it was not already set to this point. Click the

"Reset Interlock" button, and then the "Start" button near the bottom of the page. The laser will immediately begin to lase, so ensure the mechanical shutter at the exit of the laser is closed and safety goggles are worn.

The next step is to check if the laser is operating at the correct wavelength, and if the output is stable in both wavelength and power. Align the laser source to the input of an optical spectrum analyzer, and verify the measured wavelength is same as the one selected on the M2 control page. Also verify the stability of the wavelength over time. Next redirect the laser source into power meter or quadrant detector to measure the power stability of the output.

If the power and/or wavelength of the output are not behaving as expected, contact M^2.

Turn on the on-board HeNe laser using the turn-key power supply, ensure the HeNe source illuminates as usual.

Alignment

The next major objective is to assess the alignment of the system. Starting with the on-board HeNe, trace the path of the beam with a business card. The beam should strike the upper left corner of the measurement prism's entrance face. If the beam is striking the prism's entrance face but not the upper left corner, use the steering dials to redirect the beam to this corner. If the beam is obstructed or does not hit the measurement prism, a total realignment may be needed.

Using LCD paper, follow the beam path of the M^2 IR laser. Ensure the beam is not clipped by any mirrors and passes through the center of any apertures used to decrease the beam power/diameter. Place a moveable mirror on the Metricon stage in the beam path of both the HeNe and M2 lasers, after the physical location where they have been combined. This will direct both beams off of the Metricon and allow for easier analysis of their alignment.

Place either the LCD paper or the quadrant detector in new beam path, close to the newly placed mirror. Alternate blocking the visible and IR beams to determine if the centers of the two beams are striking the LCD paper / quadrant detector at the same point. Next move the LCD paper / quadrant detector further away from the moveable mirror but make sure it is still in the beam path. Again determine if the centers of the two beams are striking the LCD paper / quadrant detector at the same point. If the two beams are "overlapping" at both of these locations, the two beams are aligned. If they are not overlapping at both locations, the mirrors associated with that specific M2 laser will need to be adjusted until this condition is satisfied. Do not attempt to align the on-board mirrors to achieve "overlap" as this will cause a miss alignment in all other sources coupled into the Metricon.

3. Calibration

Now that the system has been inspected and the sources have been analyzed, the system must be calibrated. Calibration is not essential on a daily basis, but should be performed when any of the following conditions are met:

- Measurements are being conducted on a new project

- Measurements are being conducted at a new temperature and/or wavelength set point
- The last calibration was performed over 120 day ago
- There is a major discrepancy in measured values for known reference standards
- There have been modifications to the system, specifically the location of the thermocouples or heating elements.

The calibration begins with the thermal aspect. Attach a representative sample to the Metricon as if it was going to be measured normally. Affix a thermocouple to the sample as close to the measurement location as possible (upper left corner) without risking damage to the prism or sample.

Change the temperature set point for the two thermal controllers to 25 °C. After the system has had ample time to thermally equilibrate, record the temperature at the thermocouple location. Repeat this process in 5 – 10 °C intervals until you have reached or slightly exceeded your highest target temperature set point. Plot the measured temperature against the temperature set points. The shape of this curve should be linear, and can be easily fit with a linear function. Use this to determine the correct temperature set point to produce the desired temperature at the measurement location.

Replace the representative sample with a ZnSe reference standard (or other standard if it is available). Set the thermal controllers to the set point which will result in a measurement temperature of 30 °C (or any other specific set point). Measure the refractive index of this ZnSe sample using the Metricon software. If the measured index of the ZnSe sample is

different than the provided index at that wavelength and temperature, change the refractive index of the prism using the "Recalculate" feature. Within this option, change the prism index until the measured ZnSe index matches the provided reference index, and note the prism index. Repeat this process a minimum of 15 times to obtain an average index of the measurement prism at this measurement temperature and wavelength. This process should be repeated for each temperature and wavelength set point that is needed for calibration.

4. Measurements

Clean the sample and the prism with cotton swab or Kim wipe doused with acetone or another organic solvent. Both surfaces should be free of debris to ensure a good optical contact. If the sample is smaller (~10mm in diameter), hold the sample against the prism with wafer tweezers and activate the pneumatic actuator to hold the sample in place. If the sample is larger, the sample can be held by hand (with gloves), knowing that any oils from handling will require extra cleaning. Additionally for larger samples, make sure the position you wish to measure corresponds the actual measurement location. With the sample in place, adjust the temperature to the appropriate set point, as determined by the temperature calibration.

Within the Metricon software, set the refractive index of the prism to the calibrated index corresponding to the current measurement wavelength and temperature. Set the measurement window range so that the refractive index of the sample is approximately in the middle of the two boundaries, with a total range covering at least 1000 steps. If the

refractive index is not known, set the measurement range to a larger area, centered on an approximated value for the sample's refractive index.

To start the measurement press either the F1 key or click "Start New Measurement" within the Metricon software. The center column with the prism, sample, and detecting optics should begin to rotate and display the recorded intensity. The recorded intensity should be flat as the column rotates, until the angle of total internal reflection is reached. At this point the intensity will sharply decrease and there will be a "knee", as shown in Figure A.1.

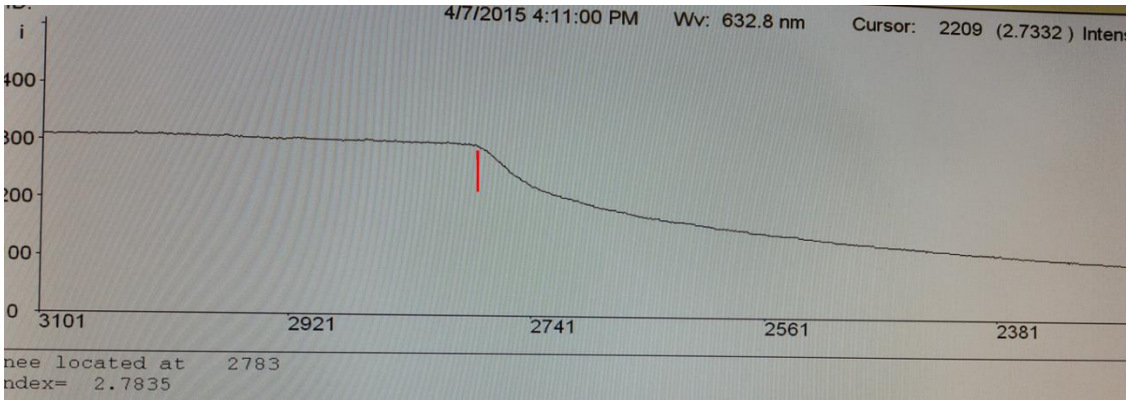

Figure A.1 – Visual output of the Metricon software. The "knee" is indicated by the red line in the graph, and is used to calculate the refractive index.

Select the index of the sample by clicking on knee location. Save the measurement and record the refractive index in an external Excel file. Repeat this process 5-15 times (depending on level of accuracy and confidence needed) to obtain an average index and error around that average. If a sample of unknown index does not exhibit a knee, adjust the

measurement window and range and repeat until the knee is found. After the knee is found, narrow the measurement window to decrease the time needed for measurements.

APPENDIX – B

This section briefely describes the design of thermal and mechanical upgrades to Metricon system at University of Central Florida, performed by undergraduate student Rebecca Whitsitt. The entries in this section are taken from the final report of Ms. Whitsitt's independent study class *EMA 4912 Directed Research* at UCF.

Part Descriptions

Rotating Stage

The "rotating stage" is the platform that connects to the arm of the main rotating mechanism and upon which the detector and integrating sphere sit. The IS sits on the smaller, raised portion of the stage to allow it to move up to the prism coupler as far as possible. The two curved sections of the stage allow the detector and IS holders to be clamped at any orientation. Each of the main sections of the stage are 0.375" thick, providing adequate strength while reducing overall weight.

Integrating Sphere Holder

The IS sits inside the raised portion of the holder and can be rotated in place or across the main stage. It is secured in place by a set screw and a c-clamp, and the raised portion is screwed onto the base from underneath.

Detector Holder

The detector sits inside this raised portion, which is also bolted to the base. Again, there is a set screw and a c-clamp holding the detector in place atop the rotating stage.

Thermal Housing

The thermal housing was designed to be placed on top of the sample-prism-actuator and accommodate the thermocouple and other wiring so that nothing need be changed or taken out in order to use the housing. Thus it was difficult to create a nearly enclosed space and removable inserts were employed as additional walls to be added to the main housing structure. Originally, the housing was designed as one piece, plus the inserts, but in order to simplify the machining process and cost, the structure was separated into 4 walls and an interior block permanently fastened together with screws.

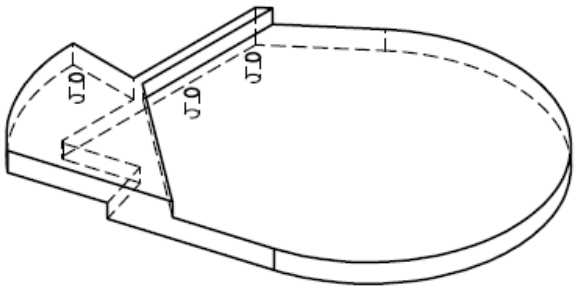

Figure B.1 – Metricon Upgrades – rotation platform for integrating sphere and detector

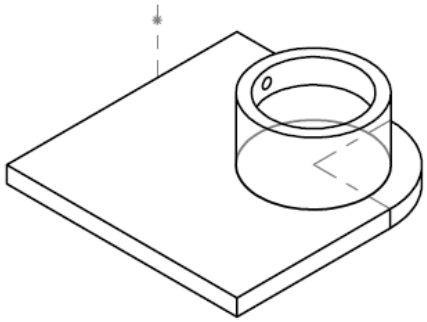

Figure B.2 – Metricon Upgrades – integrating sphere holder

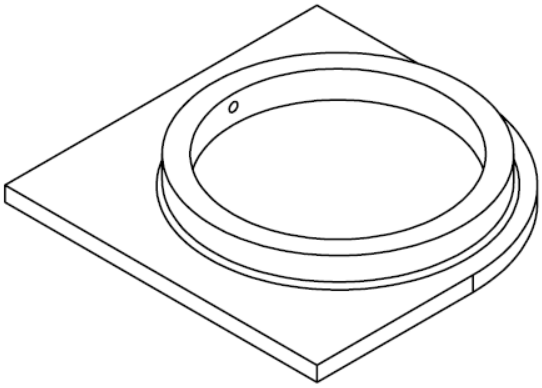

Figure B.3 – Metricon Upgrades – detector holder

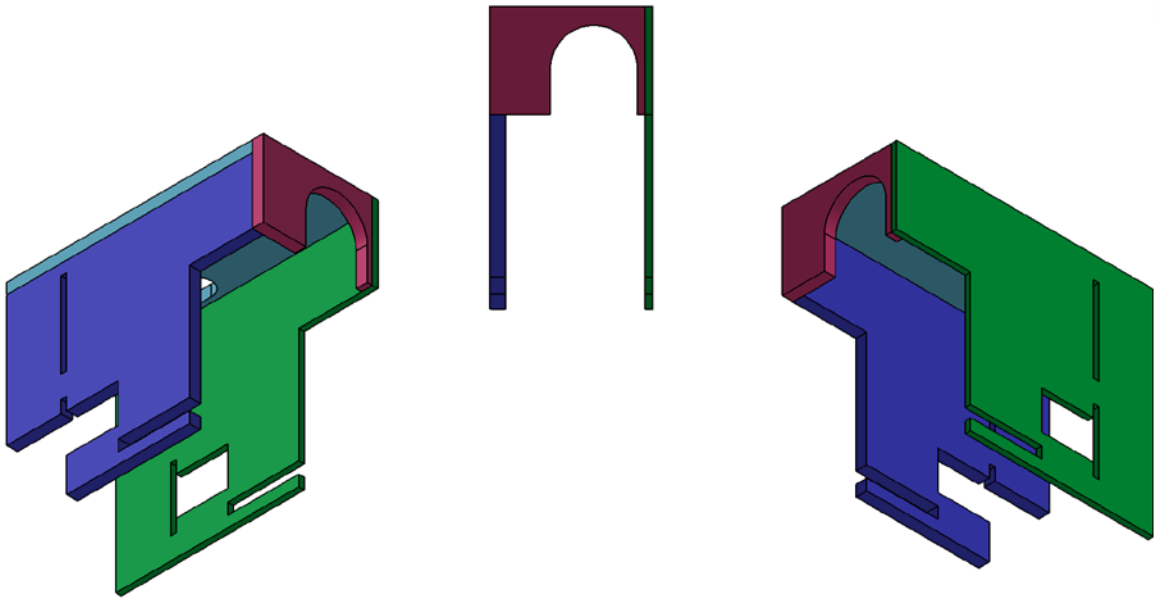

Figure B.4 – Metricon Upgrades – thermal housings

Walls 1-4

Three of the four walls are 1/8" thick and the fourth is 1/16th of an inch. There are three slots going across the width of the structure for placement of the 3 inserts. There is also a window on either side through which the laser's light can pass and space on top and on the sides for wiring.

Removable Inserts

Insert #1 is tightly fit through the prism coupler, aligned with insert # 3 (above the coupler) to form the rear wall of the enclosure and add support to the structure. Insert #2 slides in below the sample-prism-actuator and connects with the actuator's support arm to complete the bottom enclosure.

Photographs

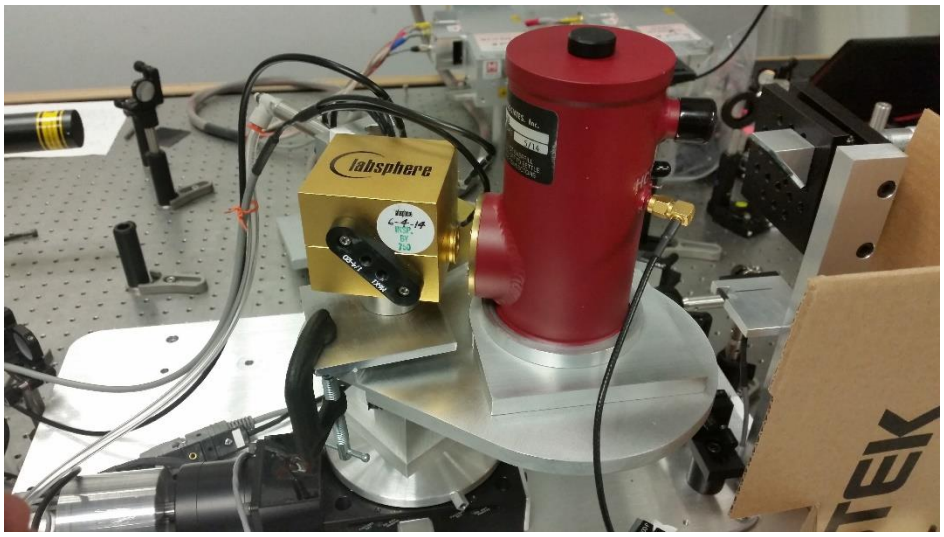

Figure B.5 –Metricon Upgrades – finished assembly

Figure B.6 – Metricon Upgrades – assembely showing the rotation platform, integrating sphere holder, and detector holder

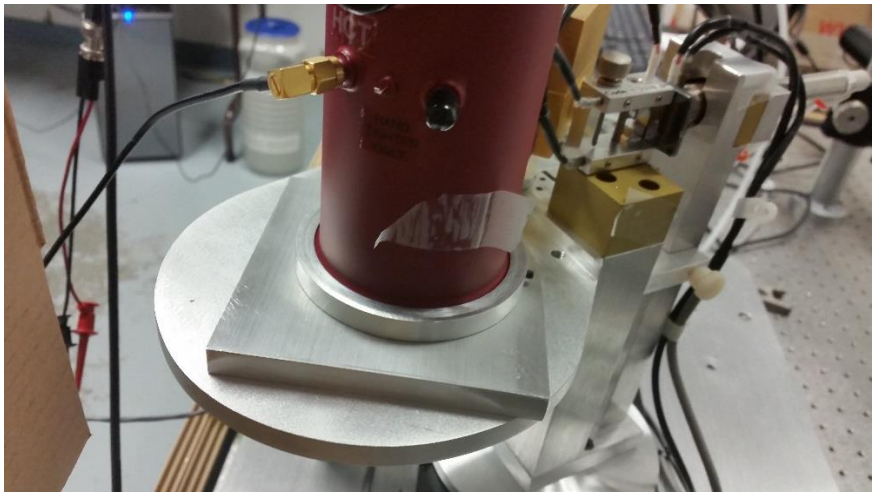

Figure B.7 – Metricon Upgrades – rear view of the rotation platform and the detector holder

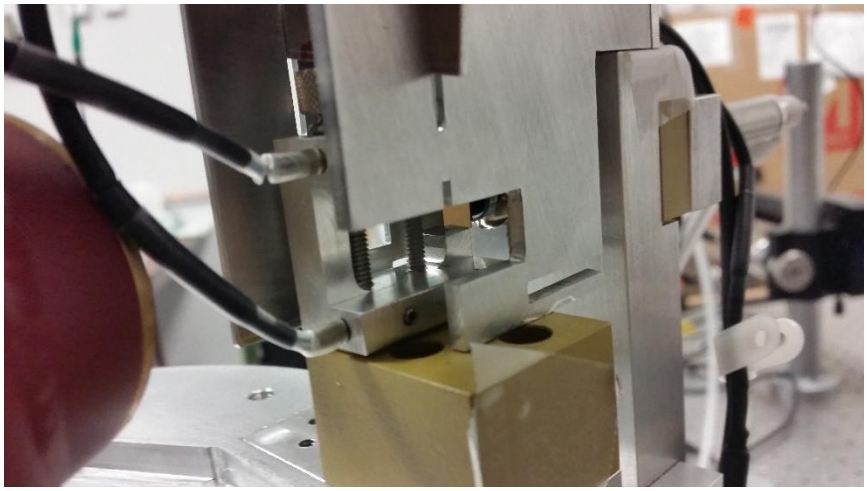

Figure B.8 – Metricon Upgrades – thermal housing around measurement prism

REFERENCE LIST

[1] E. Koontz, Characterization of Structural Relaxation in Inorganic Glasses Using Length Dilatometry, (2014).

[2] Schott Glass Inc., **Schott Optical Glass Data Sheets**, (2010).

[3] N. Carlie, L. Petit, K. Richardson, Engineering of glasses for advanced optical applications, (2006) 435-447.

[4] E. Kodak, H. Plant, INFRARED REFRACTIVE INDEXES, J. Opt. Soc. Am. (1957).

[5] J.M. Hoffman, W.L. Wolfe, Cryogenic refractive indices of ZnSe, Ge, and Si at 10.6 μm, Appl. Opt. 30 (1991) 4014-4016.

[6] G. Jellison Jr, F. Modine, Optical functions of silicon at elevated temperatures, J. Appl. Phys. 76 (1994) 3758-3761.

[7] C. Randall, R. Rawcliffe, Refractive indices of germanium, silicon, and fused quartz in the far infrared, Appl. Opt. 6 (1967) 1889-1895.

[8] B.J. Frey, D.B. Leviton, T.J. Madison, Temperature-dependent refractive index of silicon and germanium, (2006) 62732J-62732J-10.

[9] H. Icenogle, B.C. Platt, W.L. Wolfe, Refractive indexes and temperature coefficients of germanium and silicon, Appl. Opt. 15 (1976) 2348-2351.

[10] H.H. Li, Refractive index of silicon and germanium and its wavelength and temperature derivatives, Journal of Physical and Chemical Reference Data. 9 (1980) 561-658.

[11] G. Jellison Jr, F. Modine, Optical constants for silicon at 300 and 10 K determined from 1.64 to 4.73 eV by ellipsometry, J. Appl. Phys. 53 (1982) 3745-3753.

[12] M.L. Cohen, T. Bergstresser, Band structures and pseudopotential form factors for fourteen semiconductors of the diamond and zinc-blende structures, Physical Review. 141 (1966) 789.

[13] H. Morkoc, S. Strite, G. Gao, M. Lin, B. Sverdlov, M. Burns, Large-band-gap SiC, III-V nitride, and II-VI ZnSe-based semiconductor device technologies, J. Appl. Phys. 76 (1994) 1363-1398.

[14] H. Li, Refractive index of ZnS, ZnSe, and ZnTe and its wavelength and temperature derivatives, Journal of physical and chemical reference data. 13 (1984) 103-150.

[15] W.J. Tropf, Temperature-dependent refractive index models for BaF2, CaF2, MgF2, SrF2, LiF, NaF, KCl, ZnS, and ZnSe, Optical Engineering. 34 (1995) 1369-1373.

[16] G. Olbright, N. Peyghambarian, H. Gibbs, H. Macleod, F. Van Milligen, Microsecond room-temperature optical bistability and crosstalk studies in ZnS and ZnSe interference filters with visible light and milliwatt powers, Appl. Phys. Lett. 45 (1984) 1031-1033.

[17] S. Adachi, T. Taguchi, Optical properties of ZnSe, Physical review B. 43 (1991) 9569.

[18] T. Yokogawa, M. Ogura, T. Kajiwara, Low-loss short-wavelength optical waveguides using ZnSe-ZnS strained-layer superlattices, Appl. Phys. Lett. 52 (1988) 120-122.

[19] M. Rabah, B. Abbar, Y. Al-Douri, B. Bouhafs, B. Sahraoui, Calculation of structural, optical and electronic properties of ZnS, ZnSe, MgS, MgSe and their quaternary alloy Mg 1− x Zn x S y Se 1− y, Materials Science and Engineering: B. 100 (2003) 163-171.

[20] T. Bieniewski, S. Czyzak, Refractive indexes of single hexagonal ZnS and CdS crystals, JOSA. 53 (1963) 496-497.

[21] T.D. Krauss, F.W. Wise, Femtosecond measurement of nonlinear absorption and refraction in CdS, ZnSe, and ZnS, Appl. Phys. Lett. 65 (1994) 1739-1741.

[22] M. Nadeem, W. Ahmed, Optical properties of ZnS thin films, Turkish Journal of Physics. 24 (2000) 651-659.

[23] Dow Chemical, Cleartran, (2000).

[24] D.C. Harris, M. Baronowski, L. Henneman, L. LaCroix, C. Wilson, S. Kurzius, B. Burns, K. Kitagawa, J. Gembarovic, S.M. Goodrich, Thermal, structural, and optical properties of Cleartran® multispectral zinc sulfide, Optical Engineering. 47 (2008) 114001-114001-15.

[25] L. Vandeperre, F. Giuliani, S. Lloyd, W. Clegg, The hardness of silicon and germanium, Acta Materialia. 55 (2007) 6307-6315.

[26] J. Wortman, R. Evans, Young's modulus, shear modulus, and Poisson's ratio in silicon and germanium, J. Appl. Phys. 36 (1965) 153-156.

[27] G.A. Slack, S. Bartram, Thermal expansion of some diamondlike crystals, J. Appl. Phys. 46 (1975) 89-98.

[28] C.A. Klein, J. Pappis, ZnS, ZnSe, and ZnS/ZnSe windows: their impact on FLIR system performance, Optical Engineering. 25 (1986) 254519-254519-.

[29] D.B. Leviton, B.J. Frey, T. Kvamme, High accuracy, absolute, cryogenic refractive index measurements of infrared lens materials for JWST NIRCam using CHARMS, (2005) 59040O-59040O-12.

[30] Schott Glass Inc., **Schott Infrared Chalcogenide Glasses - IRG 22**, (2013).

[31] I. Amorphous Materials, **Amorpbous Materials, Inc. - Comparison of IR Materials**, (2013).

[32] Schott Glass Inc., **Schott Infrared Chalcogenide Glasses - IRG 23**, (2013).

[33] Schott Glass Inc., **Schott Infrared Chalcogenide Glasses - IRG 24**, (2013).

[34] Schott Glass Inc., **Schott Infrared Chalcogenide Glasses - IRG 25**, (2013).

[35] Schott Glass Inc., **Schott Infrared Chalcogenide Glasses - IRG 26**, (2013).

[36] R. Hilton, Infrared Chalcogenide Glass, (2006).

[37] X. Zhang, Y. Guimond, Y. Bellec, Production of complex chalcogenide glass optics by molding for thermal imaging, J. Non Cryst. Solids. 326 (2003) 519-523.

[38] J.D. Musgraves, P. Wachtel, S. Novak, J. Wilkinson, K. Richardson, Composition dependence of the viscosity and other physical properties in the arsenic selenide glass system, J. Appl. Phys. 110 (2011) 063503.

[39] A. Lakatos, M. Abkowitz, Electrical Properties of Amorphous Se, As 2 Se 3, and As 2 S 3, Physical Review B. 3 (1971) 1791.

[40] K. Tanaka, Structural phase transitions in chalcogenide glasses, Physical Review B (Condensed Matter). 39 (1989) 1270-9.

[41] S. Dembovskii, N. Luzhnaya, DIAGRAMMA SOSTOYANIYA SISTEMY AS-SE, Zhurnal Neorganicheskoi Khimii. 9 (1964) 660-664.

[42] K. Arai, S. Saito, Glass Transition in Chalcogenide Glasses, Japanese Journal of Applied Physics. 10 (1971) 1669.

[43] R. Ota, M. Kunugi, Thermal Expansion Coefficient and Glass Transition Temperature for As–Se Glasses, J Ceram Soc Jpn. 81 (1973) 228-231.

[44] K. Rao, R. Mohan, Glass transitions in arsenic-selenium glasses, J. Phys. Chem. 84 (1980) 1917-1919.

[45] A. Voronova, V. Ananichev, L. Blinov, Thermal Expansion of Melts and Glasses in the As–Se System, Glass physics and chemistry. 27 (2001) 267-273.

[46] L.E. Busse, Temperature dependence of the structures of As 2 Se 3 and As x S 1-x glasses near the glass transition, Physical Review B. 29 (1984) 3639.

[47] G. Yang, B. Bureau, T. Rouxel, Y. Gueguen, O. Gulbiten, C. Roiland, E. Soignard, J.L. Yarger, J. Troles, J. Sangleboeuf, Correlation between structure and physical properties of chalcogenide glasses in the As x Se 1− x system, Physical Review B. 82 (2010) 195206.

[48] D.C. Kaseman, I. Hung, Z. Gan, B. Aitken, S. Currie, S. Sen, Structural and Topological Control on Physical Properties of Arsenic Selenide Glasses, The Journal of Physical Chemistry B. 118 (2014) 2284-2293.

[49] K. Tanaka, Glass transition of covalent glasses, Solid State Commun. 54 (1985) 867-9.

[50] C. Hach, K. Cerqua-Richardson, J. Varner, W. LaCourse, Density and microhardness of As–Se glasses and glass fibers, J. Non Cryst. Solids. 209 (1997) 159-165.

[51] K. Tanaka, Elastic properties of covalent glasses, Solid State Commun. 60 (1986) 295-297.

[52] H. He, M. Thorpe, Elastic properties of glasses, Phys. Rev. Lett. 54 (1985) 2107.

[53] A. Feltz, H. Aust, A. Blayer, Glass formation and properties of chalcogenide systems XXVI: Permittivity and the structure of glasses As< sub> x Se< sub> 1− x and Ge< sub> x Se< sub> 1− x, J. Non Cryst. Solids. 55 (1983) 179-190.

[54] J.A. Savage, Optical properties of chalcogenide glasses, J. Non Cryst. Solids. 47 (1982) 101-115.

[55] L. Aio, A. Efimov, V. Kokorina, Refractive index of chalcogenide glasses over a wide range of compositions, J. Non Cryst. Solids. 27 (1978) 299-307.

[56] L. Petit, N. Carlie, H. Chen, S. Gaylord, J. Massera, G. Boudebs, J. Hu, A. Agarwal, L. Kimerling, K. Richardson, Compositional dependence of the nonlinear refractive index of new germanium-based chalcogenide glasses, Journal of Solid State Chemistry. 182 (2009) 2756-2761.

[57] J. David Musgraves, N. Carlie, L. Petit, G. Boudebs, J. Choi, M. Richardson, K. Richardson, Effect of Replacement of As by Ge and Sb on the Photo-Response under Near Infrared Femtosecond Laser Irradiation in As-based Sulfide Glasses, International Journal of Applied Glass Science. 2 (2011) 308-320.

[58] R.P. Wang, A. Smith, A. Prasad, D.Y. Choi, B. Luther-Davies, Raman spectra of GexAsySe1−x−y glasses, J. Appl. Phys. 106 (2009).

[59] W. Li, S. Seal, C. Rivero, C. Lopez, K. Richardson, A. Pope, A. Schulte, S. Myneni, H. Jain, K. Antoine, Role of S⁄ Se ratio in chemical bonding of As–S–Se glasses investigated by Raman, x-ray photoelectron, and extended x-ray absorption fine structure spectroscopies, J. Appl. Phys. 98 (2005) 053503.

[60] E. Mammadov, D. Bobela, A. Reyes, S. Mehdiyeva, P. Taylor, Magnetic resonance study of arsenic bonding sites in ternary chalcogenide glasses, Solid State Commun. 151 (2011) 1459-1462.

[61] S. Sen, B. Aitken, Atomic structure and chemical order in Ge-As selenide and sulfoselenide glasses: An x-ray absorption fine structure spectroscopic study, Physical Review B. 66 (2002) 134204.

[62] S. Xu, R. Wang, B. Luther-Davies, A. Kovalskiy, A. Miller, H. Jain, Chemical order in GexAsySe1-xy glasses probed by high resolution X-ray photoelectron spectroscopy, J. Appl. Phys. 115 (2014) 083518.

[63] S. Sen, C. Ponader, B. Aitken, Ge and As x-ray absorption fine structure spectroscopic study of homopolar bonding, chemical order, and topology in Ge-As-S chalcogenide glasses, Physical Review B. 64 (2001) 104202.

[64] R. Wang, A. Rode, D. Choi, B. Luther-Davies, Investigation of the structure of Ge x As y Se 1-xy glasses by x-ray photoelectron spectroscopy, J. Appl. Phys. 103 (2008) 083537-083537-5.

[65] R. Golovchak, O. Shpotyuk, M. Iovu, A. Kovalskiy, H. Jain, Topology and chemical order in As x Ge x Se 1− 2x glasses: A high-resolution X-ray photoelectron spectroscopy study, J. Non Cryst. Solids. 357 (2011) 3454-3460.

[66] P. Webber, J. Savage, Some physical properties of Ge□ As□ Se infrared optical glasses, J. Non Cryst. Solids. 20 (1976) 271-283.

[67] J. Philips, Topology of covalent non-crystalline solids I: Short-range order in chalcogenide alloys.<*br* />, Journal of Non-Crystalline Solids. 34 (1979) 153-181.

[68] J. Philips, Topology of covalent non-crystalline solids II: Medium-range order in chalcogenide alloys and a-Si (Ge), Journal of Non-Crystalline Solids. 43 (1981) 37-77.

[69] M. Iovu, E. Kamitsos, C. Varsamis, P. Boolchand, M. Popescu, Raman spectra of AsxSe100-x and As40Se60 glasses doped with metals, Chalcogenide Lett. 2 (2005) 21-25.

[70] S. Xu, R. Wang, Z. Yang, L. Wang, B. Luther-Davies, Evidence of homopolar bonds in chemically stoichiometric GexAsySe1− x− y glasses, Applied Physics Express. 8 (2015) 015504.

[71] J. Li, D. Drabold, S. Krishnaswami, G. Chen, H. Jain, Electronic Structure of Glassy Chalcogenides As 4 Se 4 and As 2 Se 3: A Joint Theoretical and Experimental Study, Phys. Rev. Lett. 88 (2002) 046803.

[72] W. Salaneck, K. Liang, A. Paton, N. Lipari, Electronic structure of molecular arsenic chalcogenides, Physical Review B. 12 (1975) 725.

[73] I. Chen, Electronic structures of As 4 Se 4 and Se 8, Physical Review B. 11 (1975) 3976.

[74] K. Tanaka, T. Yamabe, A. Tachibana, H. Kato, K. Fukui, Electronic structures of tetrasulfur tetranitride, tetraarsenic tetrasulfide, and tetraarsenic tetraselenide, and their anionic species, J. Phys. Chem. 82 (1978) 2121-2126.

[75] P. Boolchand, J. Grothaus, W. Bresser, P. Suranyi, Structural origin of broken chemical order in a Ge Se 2 glass, Physical Review B. 25 (1982) 2975.

[76] P. Boolchand, The Maximum in Glass Transition Temperature (T~ g) near x= 1/3 in Ge~ xSe~ 1~-~ x Glasses, Asian Journal of Physics. 9 (2000) 709-722.

[77] M. Zhang, S. Mancini, W. Bresser, P. Boolchand, Variation of glass transition temperature, Tg, with average coordination number, m, in network glasses: Evidence of a threshold behavior in the slope |dTg/dm| at the rigidity percolation threshold (m = 2.4), J. Non Cryst. Solids. 151 (1992) 149-154.

[78] T. Cardinal, K. Richardson, H. Shim, A. Schulte, R. Beatty, K. Le Foulgoc, C. Meneghini, J. Viens, A. Villeneuve, Non-linear optical properties of chalcogenide glasses in the system As–S–Se, J. Non Cryst. Solids. 256 (1999) 353-360.

[79] J.C. Phillips, M. Thorpe, Constraint theory, vector percolation and glass formation, Solid State Commun. 53 (1985) 699-702.

[80] M. Thorpe, Continuous deformations in random networks, J. Non Cryst. Solids. 57 (1983) 355-370.

[81] J.E. Shelby, Introduction to Glass Science and Technology, Royal Society of Chemistry, 2005.

[82] R. Wang, D. Bulla, A. Smith, T. Wang, B. Luther-Davies, Structure and physical properties of GexAsySe1− x− y glasses with the same mean coordination number of 2.5, J. Appl. Phys. 109 (2011) 023517.

[83] R. Wang, B. Luther-Davis, Structural and Physical Properties of Ge(x)As(y)Se(1-x-y) Glasses, in: R. Wang (Ed.), Amorphous Chalcogenides, 1st ed., Pan Stanford Publishing, 2014, pp. 97-142.

[84] J. Hu, L. Li, H. Lin, Y. Zou, Q. Du, C. Smith, S. Novak, K. Richardson, J.D. Musgraves, Chalcogenide glass microphotonics: Stepping into the spotlight, American Ceramic Society Bulletin. 94 (2015).

[85] T.T. Nang, M. Okuda, T. Matsushita, Composition dependence of the refractive index and its photo-induced variation in the binary glass systems: Ge< sub> 1− x Se< sub> x and As< sub> 1− x Se< sub> x, J. Non Cryst. Solids. 33 (1979) 311-323.

[86] L. Petit, J. Choi, T. Anderson, R. Villeneuve, J. Massera, N. Carlie, M. Couzi, M. Richardson, K.C. Richardson, Effect of Ga and Se addition on the "near-surface" photo-response of new Ge-based chalcogenide glasses under IR femtosecond laser exposure, Optical Materials. 31 (2009) 965-969.

[87] Y. Utsugi, Y. Mizushima, Photostructural change in the Urbach tail in chalcogenide glasses, J. Appl. Phys. 51 (1980) 1773-1779.

[88] A. Kolobov, H. Oyanagi, A. Roy, K. Tanaka, Role of lone-pair electrons in reversible photostructural changes in amorphous chalcogenides, J. Non Cryst. Solids. 227 (1998) 710-714.

[89] Schott Glass Inc., Schott Infrared Chalcogenide Glasses - N-BK7, (2007).

[90] R.P. Wang, D. Bulla, A. Smith, T. Wang, B. Luther-Davies, Structure and physical properties of GexAsySe1−x−y glasses with the same mean coordination number of 2.5, J. Appl. Phys. 109 (2011).

[91] S. Sen, E. Gjersing, B. Aitken, Physical properties of Ge x As 2x Te 100− 3x glasses and Raman spectroscopic analysis of their short-range structure, J. Non Cryst. Solids. 356 (2010) 2083-2088.

[92] J.D. Musgraves, P. Wachtel, B. Gleason, K. Richardson, Raman spectroscopic analysis of the Ge–As–S chalcogenide glass-forming system, J. Non Cryst. Solids. 386 (2014) 61-66.

[93] I. Kaban, P. Jóvári, R. Wang, B. Luther-Davies, N. Mattern, J. Eckert, Structural investigations of Ge5AsxSe95− x and Ge15AsxSe85− x glasses using x-ray diffraction and extended x-ray fine structure spectroscopy, Journal of Physics: Condensed Matter. 24 (2012) 385802.

[94] I. Pethes, I. Kaban, R. Wang, B. Luther-Davies, P. Jóvári, Short range order in Ge–As–Se glasses, J. Alloys Compounds. 623 (2015) 454-459.

[95] T. Wang, O. Gulbiten, R. Wang, Z. Yang, A. Smith, B. Luther-Davies, P. Lucas, Relative Contribution of Stoichiometry and Mean Coordination to the Fragility of Ge–As–Se Glass Forming Liquids, The Journal of Physical Chemistry B. 118 (2014) 1436-1442.

[96] T. Wang, W. Wei, X. Shen, R. Wang, B.L. Davies, I. Jackson, Elastic transition thresholds in Ge? As (Sb)? Se glasses, J. Phys. D. 46 (2013) 165302.

[97] R. Wang, A. Smith, B. Luther-Davies, H. Kokkonen, I. Jackson, Observation of two elastic thresholds in Ge x As y Se 1-xy glasses, J. Appl. Phys. 105 (2009) 056109-056109-3.

[98] M. Tatsumisago, B. Halfpap, J. Green, S. Lindsay, C. Angell, Fragility of Ge-As-Se glass-forming liquids in relation to rigidity percolation, and the Kauzmann paradox, Phys. Rev. Lett. 64 (1990) 1549.

[99] T. Velinov, M. Gateshki, D. Arsova, E. Vateva, Thermal diffusivity of Ge-As-Se (S) glasses, Physical Review B. 55 (1997) 11014.

[100] D. Bulla, R. Wang, A. Prasad, A. Rode, S. Madden, B. Luther-Davies, On the properties and stability of thermally evaporated Ge–As–Se thin films, Applied Physics A. 96 (2009) 615-625.

[101] M. Nam, J. Washer, J. Oh, Breaking the Mold: Overcoming Manufacturing Challenges of Chalcogenide Glass Optics, Photonics Spectra. 49 (2015) 52-57.

[102] A.Y. Yi, A. Jain, Compression molding of aspherical glass lenses–a combined experimental and numerical analysis, J Am Ceram Soc. 88 (2005) 579-586.

[103] G. Curatu, Design and fabrication of low-cost thermal imaging optics using precision chalcogenide glass molding, 7060 (2008) 706008.

[104] G. Cogburn, L. Mertus, A. Symmons, Molding aspheric lenses for low-cost production versus diamond turned lenses, 7660 (2010) 766020.

[105] M. Zhou, B. Ngoi, M. Yusoff, X. Wang, Tool wear and surface finish in diamond cutting of optical glass, J. Mater. Process. Technol. 174 (2006) 29-33.

[106] J. Yan, T. Zhou, J. Masuda, T. Kuriyagawa, Modeling high-temperature glass molding process by coupling heat transfer and viscous deformation analysis, Precis Eng. 33 (2009) 150-159.

[107] G.C. Firestone, A. Jain, Y.Y. Allen, Precision laboratory apparatus for high temperature compression molding of glass lenses, Rev. Sci. Instrum. 76 (2005) 063101.

[108] P. Wachtel, P. Mosaddegh, B. Gleason, J.D. Musgraves, K. Richardson, Performance Evaluation of a Bench-Top Precision Glass Molding Machine, Advances in Mechanical Engineering. 5 (2013) 178680.

[109] Y. Tsai, C. Hung, J. Hung, Glass material model for the forming stage of the glass molding process, J. Mater. Process. Technol. 201 (2008) 751-754.

[110] W. Zhao, Y. Chen, L. Shen, A.Y. Yi, Refractive index and dispersion variation in precision optical glass molding by computed tomography, Appl. Opt. 48 (2009) 3588-3595.

[111] K.D. Fischbach, K. Georgiadis, F. Wang, O. Dambon, F. Klocke, Y. Chen, Y.Y. Allen, Investigation of the effects of process parameters on the glass-to-mold sticking force during precision glass molding, Surface and Coatings Technology. 205 (2010) 312-319.

[112] W.J. Bresser, P. Boolchand, P. Suranyi, J. Hernandez, Molecular phase separation and cluster size in GeSe2 glass, Hyperfine Interactions. 27 (1986) 389-392.

[113] P. Boolchand, The Maximum in Glass Transition Temperature (T~ g) near x= 1/3 in Ge~ xSe~ 1~-~ x Glasses, Asian Journal of Physics. 9 (2000) 709-722.

[114] J. Massera, J. Remond, J. Musgraves, M. Davis, S. Misture, L. Petit, K. Richardson, Nucleation and growth behavior of glasses in the TeO 2–Bi 2 O 3–ZnO glass system, J. Non Cryst. Solids. 356 (2010) 2947-2955.

[115] J. Novak, S. Novak, M. Dussauze, E. Fargin, F. Adamietz, J.D. Musgraves, K. Richardson, Evolution of the structure and properties of solution-based Ge 23 Sb 7 S 70 thin films during heat treatment, Mater. Res. Bull. 48 (2013) 1250-1255.

[116] S. Novak, L. Scarpantonio, J. Novak, M.D. Prè, A. Martucci, J.D. Musgraves, N.D. McClenaghan, K. Richardson, Incorporation of luminescent CdSe/ZnS core-shell quantum dots and PbS quantum dots into solution-derived chalcogenide glass films, Optical Materials Express. 3 (2013) 729-738.

[117] Y. Zou, H. Lin, O. Ogbuu, L. Li, S. Danto, S. Novak, J. Novak, J.D. Musgraves, K. Richardson, J. Hu, Effect of annealing conditions on the physio-chemical properties of

spin-coated As 2 Se 3 chalcogenide glass films, Optical Materials Express. 2 (2012) 1723-1732.

[118] E. Koontz, V. Blouin, P. Wachtel, J.D. Musgraves, K. Richardson, Prony series spectra of structural relaxation in N-BK7 for finite element modeling, The Journal of Physical Chemistry A. 116 (2012) 12198-12205.

[119] S. Danto, D. Thompson, P. Wachtel, J.D. Musgraves, K. Richardson, B. Giroire, A Comparative Study of Purification Routes for As2Se3 Chalcogenide Glass, International Journal of Applied Glass Science. 4 (2013) 31-41.

[120] D. Thompson, S. Danto, J. Musgraves, P. Wachtel, B. Giroire, K. Richardson, Microwave assisted synthesis of high purity As2Se3 chalcogenide glasses, Physics and Chemistry of Glasses-European Journal of Glass Science and Technology Part B-European Journal of Glass Science and Technology Part B. 54 (2013) 27-34.

[121] O. Shpotyuk, J. Dlugosz, A. Golovchak, A. Kozdras, Physical Ageing of Chalcogenide Glasses, in: O. Shpotyuk (Ed.), Chalcogenide Glasses: Preperation, Properties and Applications, 1st ed., Woodhead Publishing, 2014, pp. 209-301.

[122] P. Tronc, M. Bensoussan, A. Brenac, G. Errandonea, C. Sebenne, Raman scattering and local order in GexSe 1-x glasses for $1/3 \leq x \leq 1/2$, Journal de Physique. 38 (1977) 1493-1498.

[123] T.A. Dow, M.H. Miller, P.J. Falter, Application of a fast tool servo for diamond turning of nonrotationally symmetric surfaces, Precis Eng. 13 (1991) 243-250.

[124] C.G. Blough, M. Rossi, S.K. Mack, R.L. Michaels, Single-point diamond turning and replication of visible and near-infrared diffractive optical elements, Appl. Opt. 36 (1997) 4648-4654.

[125] G. Tao, S. Shabahang, E. Banaei, J.J. Kaufman, A.F. Abouraddy, Multimaterial preform coextrusion for robust chalcogenide optical fibers and tapers, Opt. Lett. 37 (2012) 2751-2753.

[126] B. Gleason, P. Wachtel, J.D. Musgraves, K. Richardson, Using design of experiments to improve precision glass moulding, International Journal of Experimental Design and Process Optimisation. 3 (2013) 263-275.

[127] G. Cogburn, Advanced manufacturing methods for chalcogenide molded optics, 8012 (2011) 80122E.

[128] G. Curatu, Design and fabrication of low-cost thermal imaging optics using precision chalcogenide glass molding, (2008) 706008-706008-7.

[129] J.C. Lambropoulos, S. Xu, T. Fang, Loose abrasive lapping hardness of optical glasses and its interpretation, Appl. Opt. 36 (1997) 1501-1516.

[130] K. Puttick, M. Rudman, K. Smith, A. Franks, K. Lindsey, Single-Point Diamond Machining of Glasses, Proceedings of the Royal Society of London.Series A, Mathematical and Physical Sciences. (1989) 19-30.

[131] J. DeGroote Nelson, Optical Materials, Fabrication and Testing for the Optical Engineer. SPIE Short Course, (2013).

[132] M. Cumbo, Chemo-mechanical Interactions in Optical Polishing, (1993).

[133] G. Beall, Design and properties of glass-ceramics, Annual Review of Materials Science. 22 (1992) 91-119.

[134] B. Ananthasayanam, P.F. Joseph, D. Joshi, S. Gaylord, L. Petit, V.Y. Blouin, K.C. Richardson, D.L. Cler, M. Stairiker, M. Tardiff, Final shape of precision molded optics: Part I—Computational approach, material definitions and the effect of lens shape, Journal of Thermal Stresses. 35 (2012) 550-578.

[135] B. Ananthasayanam, P.F. Joseph, D. Joshi, S. Gaylord, L. Petit, V.Y. Blouin, K.C. Richardson, D.L. Cler, M. Stairiker, M. Tardiff, Final shape of precision molded optics: Part II—Validation and sensitivity to material properties and process parameters, Journal of Thermal Stresses. 35 (2012) 614-636.

[136] M. Yamane, J. Mackenzie, Vicker's hardness of glass, J. Non Cryst. Solids. 15 (1974) 153-164.

[137] H. Fang, P. Guo, J. Yu, Surface roughness and material removal in fluid jet polishing, Appl. Opt. 45 (2006) 4012-4019.

[138] T. Leung, W. Lee, X. Lu, Diamond turning of silicon substrates in ductile-regime, J. Mater. Process. Technol. 73 (1998) 42-48.

[139] L. Aio, V. Kokorina, Glass Formation and Properties of Glasses in the As–Ge–Se System, Opt.–Mekh.Prom-st. (1963) 36-43.

[140] L. Aio, B. Kokorina, Optiko-mech, (1961).

[141] H.A. Qiao, N.C. Anheier, J.D. Musgrave, K. Richardson, D.W. Hewak, Measurement of chalcogenide glass optical dispersion using a mid-infrared prism coupler, (2011) 80160F-80160F-10.

[142] N. Carlie, N. Anheier Jr, H.A. Qiao, B. Bernacki, M.C. Phillips, L. Petit, J.D. Musgraves, K. Richardson, Measurement of the refractive index dispersion of As2Se3 bulk glass and thin films prior to and after laser irradiation and annealing using prism coupling in the near-and mid-infrared spectral range, Rev. Sci. Instrum. 82 (2011) 053103.

[143] K. Lipschultz, Internal reports - Pacific Northwest National Laboratory, (2011).

[144] T. Zhou, J. Zhang, B. Hu, H. Yang, Measurements of the thermo-optic coefficient of a barium fluoride single crystal, Appl. Opt. 33 (1994) 2620-2623.

[145] J. McCloy, B. Riley, B. Johnson, M. Schweiger, H.A. Qiao, N. Carlie, The Predictive Power of Electronic Polarizability for Tailoring the Refractivity of High-Index Glasses: Optical Basicity Versus the Single Oscillator Model, J Am Ceram Soc. 93 (2010) 1650-1662.

[146] L. Prod'homme, A new approach to the thermal change in the refractive index of glasses, Phys.Chem.Glasses. 1 (1960) 119-122.

[147] A.R. Hilton, Optical properties of chalcogenide glasses, J. Non Cryst. Solids. 2 (1970) 28-39.

[148] A. Giridhar, P. Narasimham, S. Mahadevan, Density and microhardness of Ge□ Sb□ Se glasses, J. Non Cryst. Solids. 43 (1981) 29-35.

[149] A. Giridhar, P. Narasimham, S. Mahadevan, Electrical properties of Ge□ Sb□ Se glasses, J. Non Cryst. Solids. 37 (1980) 165-179.

[150] J. Savage, P. Webber, A. Pitt, An assessment of Ge-Sb-Se glasses as 8 to 12μm infrared optical materials, J. Mater. Sci. 13 (1978) 859-864.

[151] A.K. Varshneya, Some comments on physical properties of chalcogenide glasses, J. Non Cryst. Solids. 273 (2000) 1-7.

[152] U. Fotheringham, A. Baltes, P. Fischer, P. Höhn, R. Jedamzik, C. Schenk, C. Stolz, G. Westenberger, Refractive index drop observed after precision molding of optical elements: a quantitative understanding based on the Tool–Narayanaswamy–Moynihan Model, J Am Ceram Soc. 91 (2008) 780-783.

[153] R. Golovchak, O. Shpotyuk, A. Kozdras, B. Bureau, M. Vlček, A. Ganjoo, H. Jain, Atomistic model of physical ageing in Se-rich As–Se glasses, Philosophical Magazine. 87 (2007) 4323-4334.

[154] R. Golovchak, H. Jain, O. Shpotyuk, A. Kozdras, A. Saiter, J. Saiter, Experimental verification of the reversibility window concept in binary As-Se glasses subjected to a long-term physical aging, Physical Review B. 78 (2008) 014202.

[155] R. Golovchak, O. Shpotyuk, A. Kozdras, M. Vlček, B. Bureau, A. Kovalskiy, H. Jain, Long-term physical ageing in As–Se glasses with short chalcogen chains, Journal of Physics: Condensed Matter. 20 (2008) 245101.

[156] R.Y. Golovchak, C. Gorecki, A. Kozdras, O. Shpotyuk, Physical ageing effects in vitreous arsenic selenides, Solid State Commun. 137 (2006) 67-69.

[157] H. Koseki, A. Odajima, Photo-induced stress relaxation in amorphous selenium films, Japanese Journal of Applied Physics. 21 (1982) 424.

[158] D. Caprion, H. Schober, Structure and relaxation in liquid and amorphous selenium, Physical Review B. 62 (2000) 3709.

[159] R. Stephens, The viscosity and structural relaxation rate of evaporated amorphous selenium, J. Appl. Phys. 49 (1978) 5855-5864.

[160] J. Larmagnac, J. Grenet, P. Michon, Glass transition temperature dependence on heating rate and on ageing for amorphous selenium films, J. Non Cryst. Solids. 45 (1981) 157-168.

[161] R. Golovchak, B. Bureau, O. Shpotyuk, V. Boyko, M. Hyla, Bond-changing structural rearrangement in glassy As 3 Se 7 associated with long-term physical aging, J. Non Cryst. Solids. 377 (2013) 43-45.

[162] S. Bhosle, K. Gunasekera, P. Boolchand, M. Micoulaut, Melt Homogenization and Self-Organization in Chalcogenides-Part I, International Journal of Applied Glass Science. 3 (2012) 189-204.

[163] S. Bhosle, K. Gunasekera, P. Boolchand, M. Micoulaut, Melt Homogenization and Self-Organization in Chalcogenides-Part II, International Journal of Applied Glass Science. 3 (2012) 205-220.